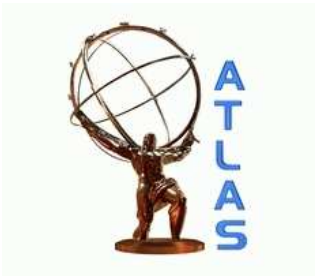

ATLAS NOTE

6th May 2010

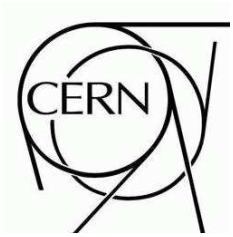

Response and Shower Topology of 2 to 180 GeV Pions Measured with the ATLAS Barrel Calorimeter at the CERN Test–beam and Comparison to Monte Carlo Simulations

E. Abat[k,1], J.M. Abdallah[f], T.N. Addy[af], P. Adragna[bz], M. Aharrouche[ay], A. Ahmad[cn], T.P.A. Akesson[aw], M. Aleksa[r], C. Alexa[n], K. Anderson[s], A. Andreazza[bc], F. Anghinolfi[r], A. Antonaki[e], G. Arabidze[e], E. Arik[k], T. Atkinson[bb], J. Baines[cc], O.K. Baker[da], D. Banfi[bd], S. Baron[r], A.J. Barr[bp], R. Beccherle[ai], H.P. Beck[i], B. Belhorma[au], P.J. Bell[az,18], D. Benchekroun[p], D.P. Benjamin[ab], K. Benslama[cd], E. Bergeaas Kuutmann[cm], J. Bernabeu[cw], H. Bertelsen[u], S. Binet[bn], C. Biscarat[ac], V. Boldea[n], V.G. Bondarenko[bh], M. Boonekamp[cg], M. Bosman[f], C. Bourdarios[bn], Z. Broklova[bx], D. Burckhart Chromek[r], V. Bychkov[am], J. Callahan[ah], D. Calvet[t], M. Canneri[bt], M. Capeáns Garrido[r], M. Caprini[n], L. Cardiel Sas[r], T. Carli[r,*], L. Carminati[bd], J. Carvalho[bv], M. Cascella[bt], M.V. Castillo[cw],

[*]Corresponding Author
Email address: Tancredi.carli@cern.ch (T. Carli)
[1]Deceased
[2]Now at Universität Mainz, Mainz, Germany
[3]Now at Technische Universität Dresden, Dresden, Germany
[4]Now at University of Arizona, Tucson, United States of America
[5]Now at Rutherford Appleton Laboratory, United Kingdom
[6]Now at Columbia University, Irvington, USA
[7]Now at Brookhaven National Laboratory, Upton, USA
[8]Now at CERN
[9]Now at Munich MPI, Germany
[10]Now at LAL-Orsay, France
[11]Now at Regina University, Canada
[12]Now at Universitat Autònoma de Barcelona, Bellaterra, Spain
[13]Now at University of Victoria, Victoria, Canada
[14]Also at Institute of High Energy Physics, Chinese Academy of Sciences, Beijing, P.R. China
[15]Also at School of Physics and Engineering, Sun Yat-sen University, Guangzhou, P.R. China
[16]Also at School of Physics, Shandong University, Jinan, Shandong, P.R. China
[17]Was at CEA, Centre d'Etudes de Saclay, France
[18]Now at Université de Genève, Switzerland
[19]Now at INFN Genova and Universit di Genova, Italy
[20]Now at Joint Institute for Nuclear Research, Dubna, Russia
[21]Now at Nikhef National Institute for Subatomic Physics, Amsterdam, Netherlands
[22]Now at Yale University, New Haven, USA
[23]Now at Georg-August-Universitaet, Goettingen, Germany
[24]Now at Versicherungskammer Bayern, Munich, Germany
[25]Now at Laboratoire de Physique de Particules (LAPP), Annecy-le-Vieux, France
[26]Now at Physikalisches Institut der Universitaet Bonn, Germany
[27]Now at Laboratoire de Physique Subatomique et de Cosmologie CNRS/IN2P3, Grenoble, France
[28]Now at Harvard University, Cambridge, USA
[29]Now at ICEPP, Tokyo, Japan
[30]Now at P.N. Lebedev Institute of Physics, Moscow, Russia
[31]Now at University of South Carolina, Columbia, USA
[32]Now at UT Dallas
[33]Now at Université Pierre et Marie Curie (Paris 6) and Université Denis Diderot (Paris-7), France
[34]Now at University of Pittsburgh, USA
[35]Now at SLAC, Stanford, USA
[36]Now at IFAE, Barcelona, Spain

ATL-CAL-PUB-2010-001
06 May 2010

A. Catinaccio[r], D. Cauz[aj], D. Cavalli[bc], M. Cavalli Sforza[f], V. Cavasinni[bt], S.A. Cetin[k], H. Chen[j], R. Cherkaoui[ca], L. Chevalier[cg], F. Chevallier[au], S. Chouridou[cu], M. Ciobotaru[cs], M. Citterio[bc], A. Clark[ad], B. Cleland[bu], M. Cobal[aj], E. Cogneras[i], P. Conde Muino[bv], M. Consonni[bd], S. Constantinescu[n], T. Cornelissen[ai], S. Correard[v], A. Corso Radu[r], G. Costa[bc], M.J. Costa[cw], D. Costanzo[ci], S. Cuneo[ai], P. Cwetanski[ah], D. Da Silva[ce], M. Dam[u], M. Dameri[ai], H.O. Danielsson[r], D. Dannheim[r], G. Darbo[ai], T. Davidek[bx], K. De[d], P.O. Defay[t], B. Dekhissi[av], J. Del Peso[ax], T. Del Prete[bt], M. Delmastro[r], F. Derue[at], L. Di Ciaccio[aq], S. Dita[n], F. Dittus[r], F. Djama[v], T. Djobava[cp], D. Dobos[z,8], M. Dobson[r], B.A. Dolgoshein[bh], A. Dotti[bt], G. Drake[b], Z. Drasal[bx], N. Dressnandt[br], C. Driouchi[u], J. Drohan[ct], W.L. Ebenstein[ab], P. Eerola[1], I. Efthymiopoulos[r], K. Egorov[ah], T.F. Eifert[r], K. Einsweiler[h], M. El Kacimi[ar], M. Elsing[r], D. Emelyanov[cc,20], C. Escobar[cw], A.I. Etienvre[cg], A. Fabich[r], K. Facius[u], A.I. Fakhr-Edine[o], M. Fanti[bd], A. Farbin[d], P. Farthouat[r], D. Fassouliotis[e], L. Fayard[bn], R. Febbraro[t], O.L. Fedin[bs], A. Fenyuk[by], D. Fergusson[h], P. Ferrari[r,21], R. Ferrari[bq], B.C. Ferreira[ce], A. Ferrer[cw], D. Ferrere[ad], G. Filippini[t], T. Flick[cz], D. Fournier[bn], P. Francavilla[bt], D. Francis[r], R. Froeschl[r], D. Froidevaux[r], E. Fullana[b], S. Gadomski[ad], G. Gagliardi[ai], P. Gagnon[ah], M. Gallas[r], B.J. Gallop[cc], S. Gameiro[r], K.K. Gan[bm], R. Garcia[ax], C. Garcia[cw], I.L. Gavrilenko[bg], C. Gemme[ai], P. Gerlach[cz], N. Ghodbane[t], V. Giakoumopoulou[e], V. Giangiobbe[bt], N. Giokaris[e], B.Di. Girolamo[r], G. Glonti[am], T. Goettfert[bj], T. Golling[h,22], N. Gollub[r], A. Gomes[bv], M.D. Gomez[ad], S. Gonzalez-Sevilla[cw,18], M.J. Goodrick[q], G. Gorfine[bl], B. Gorini[r], D. Goujdami[o], K.-J. Grahn[ap], P. Grenier[t,35], N. Grigalashvili[am], Y. Grishkevich[bi], J. Grosse-Knetter[l,23], M. Gruwe[r], C. Guicheney[t], A. Gupta[s], C. Haeberli[i], R. Haertel[bj,24], Z. Hajduk[x], H. Hakobyan[db], M. Hance[br], J.D. Hansen[u], P.H. Hansen[u], K. Hara[cr], A. Harvey Jr.[af], R.J. Hawkings[r], F.E.W. Heinemann[bp], A. Henriques Correia[r], T. Henss[cz], L. Hervas[r], E. Higon[cw], J.C. Hill[q], J. Hoffman[y], J.Y. Hostachy[au], I. Hruska[bx], F. Hubaut[v], F. Huegging[l], W. Hulsbergen[1], M. Hurwitz[s], L. Iconomidou-Fayard[bn], E. Jansen[cb], I. Jen-La Plante[s], P.D.C. Johansson[ci], K. Jon-And[cm], M. Joos[r], S. Jorgensen[f], J. Joseph[h], A. Kaczmarska[x,33], M. Kado[bn], A. Karyukhin[by], M. Kataoka[r,25], F. Kayumov[bg], A. Kazarov[bs], P.T. Keener[br], G.D. Kekelidze[am], N. Kerschen[ci], S. Kersten[cz], A. Khomich[ba], G. Khoriauli[am], E. Khramov[am], A. Khristachev[bs], J. Khubua[am], T.H. Kittelmann[u,34], R. Klingenberg[z], E.B. Klinkby[ab], P. Kodys[bx], T. Koffas[r], S. Kolos[cs], S.P. Konovalov[bg], N. Konstantinidis[ct], S. Kopikov[by], I. Korolkov[f], V. Kostyukhin[ai,26], S. Kovalenko[bs], T.Z. Kowalski[w], K. Krüger[1], V. Kramarenko[bi], L.G. Kudin[bs], Y. Kulchitsky[bf], A.C. Le Bihan[r], C. Lacasta[cw], R. Lafaye[aq], B. Laforge[at], W. Lampl[c], F. Lanni[j], S. Laplace[aq], T. Lari[bc], S. Latorre[bc], A-C. Le Bihan[1], M. Lechowski[bn], F. Ledroit-Guillon[au], G. Lehmann[r], R. Leitner[bx], D. Lelas[bn], C.G. Lester[q], Z. Liang[y], P. Lichard[r], W. Liebig[bl], A. Lipniacka[g], M. Lokajicek[bw], L. Louchard[t], K.F. Lourerio[bm], A. Lucotte[au], F. Luehring[ah], B. Lund-Jensen[ap], B. Lundberg[aw], H. Ma[j], R. Mackeprang[u], A. Maio[bv], V.P. Maleev[bs], F. Malek[au], L. Mandelli[bd], J. Maneira[bv], M. Mangin-Brinet[ad,27], A. Manousakis[e], L. Mapelli[r], C. Marques[bv], S.Marti i Garcia[cw], F. Martin[br], M. Mathes[l], M. Mazzanti[bc], K.W. McFarlane[af], R. McPherson[cx], G. Mchedlidze[cp], S. Mehlhase[ag], C. Meirosu[r], Z. Meng[ch], C. Meroni[bc], A. Miagkov[by], V. Mialkovski[am], B. Mikulec[ad,8], D. Milstead[cm], I. Minashvili[am], B. Mindur[w], V.A. Mitsou[cw], S. Moed[ad,28], E. Monnier[v], G. Moorhead[bb], P. Morettini[ai], S.V. Morozov[bh], M. Mosidze[cp], S.V. Mouraviev[bg], E.W.J. Moyse[r], A. Munar[br], A.V. Nadtochi[bs], K. Nakamura[cr,29], P. Nechaeva[ai,30], A. Negri[bq], S. Nemecek[bw], M. Nessi[r], S.Y. Nesterov[bs], F.M. Newcomer[br], I. Nikitine[by], K. Nikolaev[am], I. Nikolic-Audit[at], H. Ogren[ah], S.H. Oh[ab], S.B. Oleshko[bs], J. Olszowska[x], A. Onofre[bv], C. Padilla Aranda[r], S. Paganis[ci], D. Pallin[t], D. Pantea[n], V. Paolone[bu], F. Parodi[ai], J. Parsons[bk], S. Parzhitskiy[am], E. Pasqualucci[cf], S.M. Passmored[r], J. Pater[az], S. Patrichev[bs], M. Peez[ax], V. Perez Reale[bk], L. Perini[bc], V.D. Peshekhonov[am], J. Petersen[r], T.C. Petersen[u], R. Petti[j,31], P.W. Phillips[cc], J. Pilcher[s], J. Pina[as], B. Pinto[bv], F. Podlyski[t], L. Poggioli[bn], A. Poppleton[r], J. Poveda[cy], P. Pralavorio[v], L. Pribyl[r], M.J. Price[r], D. Prieur[cc], C. Puigdengoles[f], P. Puzo[bn], O. Røhne[bo], F. Ragusa[bc], S. Rajagopalan[j], K. Reeves[cz,32], I. Reisinger[z], C. Rembser[r], P.A.Bruckman.de. Renstrom[bp], P. Reznicek[bx], M. Ridel[at], P. Risso[ai], I. Riu[ad,36], D. Robinson[q], C. Roda[bt], S. Roe[r], A. Romaniouk[bh], D. Rousseau[bn], A. Rozanov[v], A. Ruiz[cw], N. Rusakovich[am], D. Rust[ah], Y.F. Ryabov[bs], V. Ryjov[r], O. Salto[f], B. Salvachua[b], A. Salzburger[ak,8], H. Sandaker[g], C. Santamarina Rios[r], L. Santi[aj], C. Santoni[t], J.G. Saraiva[bv], F. Sarri[bt], G. Sauvage[aq], L.P. Says[t], M. Schaefer[au], V.A. Schegelsky[bs], C. Schiavi[ai], J. Schieck[bj], G. Schlager[r], J. Schlereth[b], C. Schmitt[ay], J. Schultes[cz], P. Schwemling[at], J. Schwindling[cg], J.M. Seixas[ce], D.M. Seliverstov[bs], L. Serin[bn], A. Sfyrla[ad,8], N. Shalanda[be], C. Shaw[ae], T. Shin[af], A. Shmeleva[bg], J. Silva[bv], S. Simion[bn], M. Simonyan[aq], J.E. Sloper[r], S.Yu. Smirnov[bh], L. Smirnova[bi],

C. Solans[cw], A. Solodkov[by], O. Solovianov[by], I. Soloviev[bs], V.V. Sosnovtsev[bh], F. Spanò[bk], P. Speckmayer[r], S. Stancu[cs], R. Stanek[b], E. Starchenko[by], A. Straessner[aa], S.I. Suchkov[bh], M. Suk[bx], R. Szczygiel[w], F. Tarrade[j], F. Tartarelli[bc], P. Tas[bx], Y. Tayalati[t], F. Tegenfeldt[al], R. Teuscher[cq], M. Thioye[cn], V.O. Tikhomirov[bg], C.J.W.P. Timmermans[cb], S. Tisserant[v], B. Toczek[w], L. Tremblet[r], C. Troncon[bc], P. Tsiareshka[bf], M. Tyndel[cc], M.Karagoez. Unel[bp], G. Unal[r], G. Unel[ah], G. Usai[s], R. Van Berg[br], A. Valero[cw], S. Valkar[bx], J.A. Valls[cw], W. Vandelli[r], F. Vannucci[at], A. Vartapetian[d], V.I. Vassilakopoulos[af], L. Vasilyeva[bg], F. Vazeille[t], F. Vernocchi[ai], Y. Vetter-Cole[y], I. Vichou[cv], V. Vinogradov[am], J. Virzi[h], I. Vivarelli[bt], J.B.de. Vivie[v,10], M. Volpi[f], T. Vu Anh[ad,2], C. Wang[ab], M. Warren[ct], J. Weber[z], M. Weber[cc], A.R. Weidberg[bp], J. Weingarten[l,23], P.S. Wells[r], P. Werner[r], S. Wheeler[a], M. Wiessmann[bj], H. Wilkens[r], H.H. Williams[br], I. Wingerter-Seez[aq], Y. Yasu[ao], A. Zaitsev[by], A. Zenin[by], T. Zenis[m], Z. Zenonos[bt], H. Zhang[v], A. Zhelezko[bh], N. Zhou[bk]

[a] *University of Alberta, Department of Physics , Centre for Particle Physics, Edmonton , AB T6G 2G7, Canada*
[b] *Argonne National Laboratory, High Energy Physics Division, 9700 S. Cass Avenue, Argonne IL 60439, United States of America*
[c] *University of Arizona, Department of Physics, Tucson , AZ 85721, United States of America*
[d] *University of Texas at Arlington, Department of Physics, Box 19059, Arlington, TX 76019, United States of America*
[e] *University of Athens, Nuclear & Particle Physics Department of Physics, Panepistimiopouli Zografou, GR 15771 Athens, Greece*
[f] *Institut de Fisica d'Altes Energies, IFAE, Universitat Autònoma de Barcelona, Edifici Cn, ES - 08193 Bellaterra (Barcelona) Spain*
[g] *University of Bergen, Department for Physics and Technology, Allegaten 55, NO - 5007 Bergen, Norway*
[h] *Lawrence Berkeley National Laboratory and University of California, Physics Division, MS50B-6227, 1 Cyclotron Road, Berkeley, CA 94720, United States of America*
[i] *University of Bern, Laboratory for High Energy Physics, Sidlerstrasse 5, CH - 3012 Bern, Switzerland*
[j] *Brookhaven National Laboratory, Physics Department, Bldg. 510A, Upton, NY 11973, United States of America*
[k] *Bogazici University, Faculty of Sciences, Department of Physics, TR - 80815 Bebek-Istanbul, Turkey*
[l] *Physikalisches Institut der Universitaet Bonn, Nussallee 12, D - 53115 Bonn, Germany*
[m] *Comenius University, Faculty of Mathematics Physics & Informatics, Mlynska dolina F2, SK - 84248 Bratislava, Slovak Republic*
[n] *National Institute of Physics and Nuclear Engineering (Bucharest -IFIN-HH), P.O. Box MG-6, R-077125 Bucharest, Romania*
[o] *Université Cadi Ayyad , Marrakech, Morocco*
[p] *Université Hassan II, Faculté des Sciences Ain Chock, B.P. 5366, MA - Casablanca, Morocco*
[q] *Cavendish Laboratory, University of Cambridge, J J Thomson Avenue, Cambridge CB3 0HE, United Kingdom*
[r] *European Laboratory for Particle Physics (CERN), CH-1211 Geneva 23, Switzerland*
[s] *University of Chicago, Enrico Fermi Institute, 5640 S. Ellis Avenue, Chicago, IL 60637, United States of America*
[t] *Laboratoire de Physique Corpusculaire (LPC), IN2P3-CNRS, Université Blaise-Pascal Clermont-Ferrand, FR - 63177 Aubiere , France*
[u] *Niels Bohr Institute, University of Copenhagen, Blegdamsvej 17, DK - 2100 Kobenhavn 0, Denmark*
[v] *Université Méditerranée, Centre de Physique des Particules de Marseille, CNRS/IN2P3, F-13288 Marseille, France*
[w] *Faculty of Physics and Applied Computer Science of the AGH-University of Science and Technology, (FPACS, AGH-UST), al. Mickiewicza 30, PL-30059 Cracow, Poland*
[x] *The Henryk Niewodniczanski Institute of Nuclear Physics, Polish Academy of Sciences, ul. Radzikowskiego 152, PL - 31342 Krakow Poland*
[y] *Southern Methodist University, Physics Department, 106 Fondren Science Building, Dallas, TX 75275-0175, United States of America*
[z] *Universitaet Dortmund, Experimentelle Physik IV, DE - 44221 Dortmund, Germany*
[aa] *Technical University Dresden, Institut fuer Kern- und Teilchenphysik, Zellescher Weg 19, D-01069 Dresden, Germany*
[ab] *Duke University, Department of Physics Durham, NC 27708, United States of America*
[ac] *Centre de Calcul CNRS/IN2P3, Lyon, France*
[ad] *Université de Genève, Section de Physique, 24 rue Ernest Ansermet, CH - 1211 Genève 4, Switzerland*
[ae] *University of Glasgow, Department of Physics and Astronomy, UK - Glasgow G12 8QQ, United Kingdom*
[af] *Hampton University, Department of Physics, Hampton, VA 23668, United States of America*
[ag] *Institute of Physics, Humboldt University, Berlin, Newtonstrasse 15, D-12489 Berlin, Germany*
[ah] *Indiana University, Department of Physics, Swain Hall West 117, Bloomington, IN 47405-7105, United States of America*
[ai] *INFN Genova and Universit di Genova, Dipartimento di Fisica, via Dodecaneso 33, IT - 16146 Genova, Italy*
[aj] *INFN Gruppo Collegato di Udine and Universit di Udine, Dipartimento di Fisica, via delle Scienze 208, IT - 33100 Udine; INFN Gruppo Collegato di Udine and ICTP, Strada Costiera 11, IT - 34014 Trieste, Italy*
[ak] *Institut fuer Astro- und Teilchenphysik, Technikerstrasse 25, A - 6020 Innsbruck, Austria*
[al] *Iowa State University, Department of Physics and Astronomy, Ames High Energy Physics Group, Ames, IA 50011-3160, United States of America*
[am] *Joint Institute for Nuclear Research, JINR Dubna, RU - 141 980 Moscow Region, Russia*
[an] *Institut fuer Prozessdatenverarbeitung und Elektronik, Karlsruher Institut fuer Technologie, Campus Nord, Hermann-v.Helmholtz-Platz 1, D-76344 Eggenstein-Leopoldshafen*

[ao] KEK, High Energy Accelerator Research Organization, 1-1 Oho Tsukuba-shi, Ibaraki-ken 305-0801, Japan
[ap] Royal Institute of Technology (KTH), Physics Department, SE - 106 91 Stockholm, Sweden
[aq] Laboratoire de Physique de Particules (LAPP), Université de Savoie, CNRS/IN2P3, Annecy-le-Vieux Cedex, France
[ar] Laboratoire de Physique de Particules (LAPP), Université de Savoie, CNRS/IN2P3, Annecy-le-Vieux Cedex, France and Université Cadi Ayyad , Marrakech, Morocco
[as] LIP and IDMEC-IST, Lisbao, Portugal
[at] Université Pierre et Marie Curie (Paris 6) and Université Denis Diderot (Paris-7), Laboratoire de Physique Nucléaire et de Hautes Energies, CNRS/IN2P3, Tour 33 4 place Jussieu, FR - 75252 Paris Cedex 05, France
[au] Laboratoire de Physique Subatomique et de Cosmologie CNRS/IN2P3, Université Joseph Fourier INPG, 53 avenue des Martyrs, FR - 38026 Grenoble Cedex, France
[av] Laboratoire de Physique Théorique et de Physique des Particules, Université Mohammed Premier, Oujda, Morocco
[aw] Lunds universitet, Naturvetenskapliga fakulteten, Fysiska institutionen, Box 118, SE - 221 00, Lund, Sweden
[ax] Universidad Autonoma de Madrid, Facultad de Ciencias, Departamento de Fisica Teorica, ES - 28049 Madrid, Spain
[ay] Universität Mainz, Institut fuer Physik, Staudinger Weg 7, DE 55099, Germany
[az] School of Physics and Astronomy, University of Manchester, UK - Manchester M13 9PL, United Kingdom
[ba] Universitaet Mannheim, Lehrstuhl fuer Informatik V, B6, 23-29, DE - 68131 Mannheim, Germany
[bb] School of Physics, University of Melbourne, AU - Parkvill, Victoria 3010, Australia
[bc] INFN Milano and Universit di Milano, Dipartimento di Fisica, via Celoria 16, IT - 20133 Milano, Italy
[bd] Università di Milano , Dipartimento di Fisica and INFN, via Celoria 16, IT - 20133 Milano, Italy
[be] B.I. Stepanov Institute of Physics, National Academy of Sciences of Belarus, Independence Avenue 68, Minsk 220072, Republic of Belarus
[bf] B.I. Stepanov Institute of Physics, National Academy of Sciences of Belarus, Independence Avenue 68, Minsk 220072, Republic of Belarus and Joint Institute for Nuclear Research, JINR Dubna, RU - 141 980 Moscow Region, Russia
[bg] P.N. Lebedev Institute of Physics, Academy of Sciences, Leninsky pr. 53, RU - 117 924, Moscow, Russia
[bh] Moscow Engineering & Physics Institute (MEPhI), Kashirskoe Shosse 31, RU - 115409 Moscow, Russia
[bi] Lomonosov Moscow State University, Skobeltsyn Institute of Nuclear Physics, RU - 119 991 GSP-1 Moscow Lenskiegory 1-2, Russia
[bj] Max-Planck-Institut fr Physik, (Werner-Heisenberg-Institut), Fhringer Ring 6, 80805 Mnchen, Germany
[bk] Columbia University, Nevis Laboratory, 136 So. Broadway, Irvington, NY 10533, United States of America
[bl] Nikhef National Institute for Subatomic Physics, Kruislaan 409, P.O. Box 41882, NL - 1009 DB Amsterdam, Netherlands
[bm] Ohio State University, 191 West WoodruAve, Columbus, OH 43210-1117, United States of America
[bn] LAL, Université Paris-Sud, IN2P3/CNRS, Orsay, France
[bo] University of Oslo, Department of Physics, P.O. Box 1048, Blindern T, NO - 0316 Oslo, Norway
[bp] Department of Physics, Oxford University, Denys Wilkinson Building, Keble Road, Oxford OX1 3RH, United Kingdom
[bq] Università di Pavia, Dipartimento di Fisica Nucleare e Teorica and INFN Pavia, Via Bassi 6 IT-27100 Pavia, Italy
[br] University of Pennsylvania, Department of Physics, High Energy Physics, 209 S. 33rd Street Philadelphia, PA 19104, United States of America
[bs] Petersburg Nuclear Physics Institute, RU - 188 300 Gatchina, Russia
[bt] Universitaá di Pisa, Dipartimento di Fisica E. Fermi and INFN Pisa , Largo B.Pontecorvo 3, IT - 56127 Pisa, Italy
[bu] University of Pittsburgh, Department of Physics and Astronomy, 3941 O'Hara Street, Pittsburgh, PA 15260, United States of America
[bv] Laboratorio de Instrumentacao e Fisica Experimental de Particulas - LIP, and SIM/Univ. de Lisboa, Avenida Elias Garcia 14-1, PT - 1000-149, Lisboa, Portugal
[bw] Academy of Sciences of the Czech Republic, Institute of Physics and Institute for Computer Science, Na Slovance 2, CZ - 18221 Praha 8, Czech Republic
[bx] Charles University in Prague, Faculty of Mathematics and Physics, Institute of Particle and Nuclear Physics, V Holesovickach 2, CZ - 18000 Praha 8, Czech Republic
[by] Institute for High Energy Physics (IHEP), Federal Agency of Atom. Energy, Moscow Region, RU - 142 284 Protvino, Russia
[bz] Queen Mary, University of London, Mile End Road, E1 4NS, London, United Kingdom
[ca] Université Mohammed V, Faculté des Sciences, BP 1014, MO - Rabat, Morocco
[cb] Radboud University Nijmegen/NIKHEF, Dept. of Exp. High Energy Physics, Toernooiveld 1, NL - 6525 ED Nijmegen, Netherlands
[cc] Rutherford Appleton Laboratory, Science and Technology Facilities Council, Harwell Science and Innovation Campus, Didcot OX11 0QX, United Kingdom
[cd] University of Regina, Physics Department, Canada
[ce] Universidade Federal do Rio De Janeiro, Instituto de Fisica, Caixa Postal 68528, Ilha do Fundao, BR - 21945-970 Rio de Janeiro, Brazil
[cf] Università La Sapienza, Dipartimento di Fisica and INFN Roma I, Piazzale A. Moro 2, IT- 00185 Roma, Italy
[cg] Commissariàt a l'Enegie Atomique (CEA), DSM/DAPNIA, Centre d'Etudes de Saclay, 91191 Gif-sur-Yvette, France
[ch] Insitute of Physics, Academia Sinica, TW - Taipei 11529, Taiwan and Shandong University, School of Physics, Jinan, Shandong 250100, P. R. China
[ci] University of Sheffield, Department of Physics & Astronomy, Hounseld Road, Sheffield S3 7RH, United Kingdom
[cj] Insitute of Physics, Academia Sinica, TW - Taipei 11529, Taiwan
[ck] SLAC National Accelerator Laboratory, Stanford, California 94309, United States of America
[cl] University of South Carolina, Columbia, United States of America
[cm] Stockholm University, Department of Physics, SE - 106 91 Stockholm, Sweden
[cn] Department of Physics and Astronomy, Stony Brook, NY 11794-3800, United States of America

[co] Insitute of Physics, Academia Sinica, TW - Taipei 11529, Taiwan and Sun Yat-sen University, School of physics and engineering, Guangzhou 510275, P. R. China
[cp] Tbilisi State University, High Energy Physics Institute, University St. 9, GE - 380086 Tbilisi, Georgia
[cq] University of Toronto, Department of Physics, 60 Saint George Street, Toronto M5S 1A7, Ontario, Canada
[cr] University of Tsukuba, Institute of Pure and Applied Sciences, 1-1-1 Tennoudai, Tsukuba-shi, JP - Ibaraki 305-8571, Japan
[cs] University of California, Department of Physics & Astronomy, Irvine, CA 92697-4575, United States of America
[ct] University College London, Department of Physics and Astronomy, Gower Street, London WC1E 6BT, United Kingdom
[cu] University of California Santa Cruz, Santa Cruz Institute for Particle Physics (SCIPP), Santa Cruz, CA 95064, United States of America
[cv] University of Illinois, Department of Physics, 1110 West Green Street, Urbana, Illinois 61801 United States of America
[cw] Instituto de Fsica Corpuscular (IFIC), Centro Mixto UVEG-CSIC, Apdo. 22085, ES-46071 Valencia; Dept. Fsica At., Mol. y Nuclear, Univ. of Valencia and Instituto de Microelectrnica de Barcelona (IMB-CNM-CSIC), 08193 Bellaterra, Barcelona, Spain
[cx] University of Victoria, Department of Physics and Astronomy, P.O. Box 3055, Victoria B.C., V8W 3P6, Canada
[cy] University of Wisconsin, Department of Physics, 1150 University Avenue, WI 53706 Madison, Wisconsin, United States of America
[cz] Bergische Universitaet, Fachbereich C, Physik, Postfach 100127, Gauss-Strasse 20, DE-42097 Wuppertal, Germany
[da] Yale University, Department of Physics , PO Box 208121, New Haven, CT06520-8121, United States of America
[db] Yerevan Physics Institute, Alikhanian Brothers Street 2, AM - 375036 Yrevan, Armenia

Abstract

The response of the ATLAS barrel calorimeter to pions with momenta from 2 to 180 GeV is studied in a test–beam at the CERN H8 beam line. The mean energy, the energy resolution and the longitudinal and radial shower profiles, and, various observables characterising the shower topology in the calorimeter are measured. The data are compared to Monte Carlo simulations based on a detailed description of the experimental set–up and on various models describing the interaction of particles with matter based on Geant4.

Contents

1. Introduction

The Large Hadron Collider (LHC) at CERN collides protons with an energy up to 7 TeV. The resulting high centre–of–mass energy opens a new chapter for particle physics exploring the high–energy frontier. Calorimeters measure the energy of charged and neutral particles subject to strong or electromagnetic interactions. One of their main tasks is to measure the energy and directions of jets, sprays of hadrons of various species that emerge from the hard parton–parton scattering. Additionally, their hermeticity allows the reconstruction of the missing transverse energy in the event. The understanding of the calorimeter response to hadrons and of their shower development is therefore important for the LHC physics program.

ATLAS is one of the multi–purpose detectors at the LHC measuring particles produced in proton–proton collisions. The inner detector tracking system (ID) measures the angles, the momentum and the life–time of charged particles. In the central detector part (barrel), the calorimeter system consists of an electromagnetic sampling calorimeter, using liquid argon as active medium and lead as absorber, and a hadronic sampling calorimeter, using plastic scintillator as active medium and iron as absorber.

In the year 2004 a full slice of the ATLAS barrel detector was exposed to particles produced in a test–beam at the CERN H8 beam line. In this "combined test–beam" (CTB) modules of all sub–detectors (tracking system, electromagnetic and hadronic calorimeter and muon chambers) were arranged in a similar way as they were installed in the ATLAS barrel detector. The read–out electronics and the data acquisition system were close to those presently used in ATLAS. A data taking period is analysed where all sub–detectors have been operational. The inner detector system is used to select single pion tracks and provides particle identification. The electromagnetic and hadronic calorimeter are used to measure the pion energy response and resolution and the hadronic shower topology. The available beam momentum range of this data taking period was 2 to 180 GeV. The results obtained in this analysis give more detailed information than results obtained from an earlier data taking period of CTB 2004 [1].

For the first time[1], the combined ATLAS barrel calorimeter system was exposed to pions of 2 to 9 GeV. Studying the calorimeter response of pions at such low momenta is important, since the hadrons constituting jets can have rather low momenta even at the high energies available at the LHC. For instance, on average 30% of the momentum of a jet with a momentum of 100 GeV is carried by hadrons with momenta below 10 GeV.

The data from the combined test–beam are compared to Monte Carlo (MC) simulations based on the Geant4 simulation framework. Various ways models (and various model combinations) to simulate the interaction of particles depending on the particle type and the particle energy are tested. The aim is to identify the best combination of models and in parallel to asses the quality of the detector response simulation. For the ATLAS barrel electromagnetic calorimeter it is the first time that the pion response is systematically compared to MC simulations.

The paper is organised as follows:

The experimental set–up including the beam line, the beam detectors and the ATLAS detector is described in section 2. The reconstruction of the energy in the calorimeters is summarised section 3. This includes the cell energy reconstruction and the definition of the pion signal. The basic ingredients of the Monte Carlo simulations are described in section 5. The data–set is described in section 4, the event selection is given in section 6 and the particle identification is discussed in section 7. The results on the mean energy response and the energy resolution are presented in section 9 and the uncertainties on the energy measurement are discussed in section 8. The longitudinal shower profiles are measured in section 11 and the transverse shower profiles in section 12. Details of the shower topology are further examined in section 13. All measurements are compared to Monte Carlo simulations. In section 14 some conclusions on the accuracy of the simulation are drawn based on a fine momentum scan.

2. Experimental Set–up

The beam passes through a system of detectors that monitor the beam position and identifies the beam particle type. It then reaches the inner detector system and finally the calorimeter system consisting of an electromagnetic (LAr) and a hadronic (TileCal) part. Behind the calorimeter, beam monitor detectors

[1] Earlier tests using proto–type modules have been restricted to higher pion momenta[2].

for muon identification were installed. The muon spectrometer installed at the end of the beam line is not used in this analysis.

A right–handed reference frame is defined that is close to the ATLAS reference frame. The x–axis points along the beam line, while the y–axis points vertically upward. The η–and ϕ–directions are chosen with respect to a reference frame with cylindrical coordinates. Its origin mimics the virtual proton–proton interaction point in ATLAS. In this coordinate system the z–axis is defined along the LHC beam axis. The ϕ and θ angles are the azimuthal and polar angles. The pseudo–rapidity is defined by $\eta = -\log\tan\theta/2$.

The set–up of the combined test–beam is described in detail in ref. [3]. A description of the main parts relevant for this analysis is given in the following.

2.1. Beam line Set–up

The CTB set–up was installed on the H8 beam line at the SPS accelerator of CERN. The primary proton beam with a momentum of 450 GeV impinges on a beryllium primary target (T4) that is up to 30 cm thick. In the target various secondary particles such as protons, pions, electrons and kaons are produced. The secondary beam is selected using a system of magnets and collimators for electrons and hadrons with momenta between 10 and 400 GeV. Electrons can be to a large extent separated from the hadronic beam component through synchrotron radiation using a system of deflecting magnets and collimators. A sketch of the beam line is shown in Fig. 1.

Particles with momenta greater than 10 GeV move along the straight line and are produced upstream. This beam line is called high energy (HE) beam line in the following. The momentum (P_{beam}) spread of the HE beam line is estimated to be $\Delta P_{\mathrm{beam}}/P_{\mathrm{beam}} = 1\%$.

To produce particles at lower momenta (< 10 GeV), a 80 GeV secondary pion beam is directed on a 1 m long secondary polyethylene target that is installed 45 m before the experimental set–up. An absorber is placed after the target to stop particles that would reach the detector system via the HE beam line.

The particles are focused and deflected to the very low energy (VLE) beam line where the momentum selection is done using four dipole magnets and collimators. These tertiary beam particles are then sent back to the HE beam line where they are directed to the experimental set–up. The VLE beam line can deliver particles with momenta ranging from 2 to 9 GeV with a momentum spread of $\Delta P_{\mathrm{beam}}/P_{\mathrm{beam}} = 3\%$. Most of the produced particles are electrons.

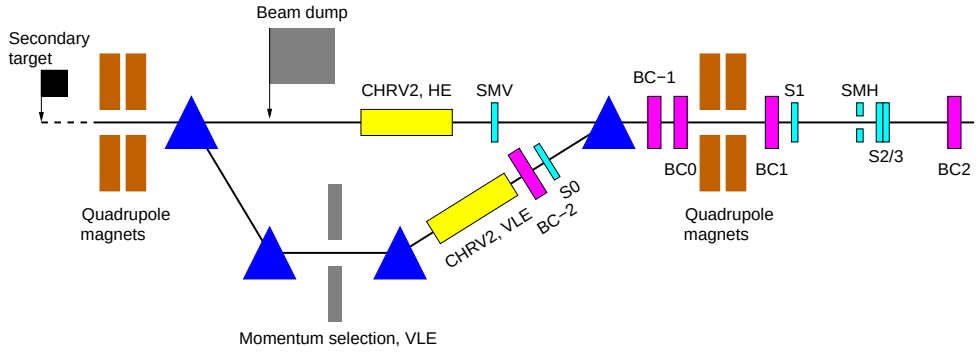

Figure 1: Sketch of the HE (straight part) and VLE (part bent downwards) H8 beam line at the SPS and of the beam monitor detectors. The particle beam enters from the left. The triangles mark the dipole positions to deflect the particles into the VLE beam line and to redirect them after momentum selection back to the HE beam line.

2.2. Beam Momentum Determination

The beam momenta are calculated from the magnet currents and the beam line collimator settings. This method relies on work done for the LAr calorimeter in the 2002 test–beam analysis [4], where a system of Hall probes was used to precisely determine the magnetic field in the bending magnets.

Based on this Hall probe measurement the relation between the measured magnet currents and the magnetic field in the bending magnets is known. The precision of the knowledge of the beam momenta in the HE beam line is about 0.3%.

For the runs at 20, 50 and 100 GeV the magnet currents have not been recorded and the beam momenta of runs that are nearby in time have been used. However, typical variations of the beam momentum when changing the beam line settings and then restoring them to the previous values is 0.1%. The precision of this procedure can be cross–checked by measuring electrons.

Additionally, for the VLE beam line, beam momenta were measured using the deflection angle of the beam chamber in the VLE beam line (BC–2) event by event [5, 6]. An overall normalisation factor between the HE and the VLE beam line of 0.975 has been introduced [5, 6].

The measured beam momenta are given in Table 5. The uncertainty is about 0.8% for all beam momenta. The beam spread in the VLE set–up is about 3%, while it is 0.24% for the HE set–up.

2.3. Beam line Detectors

The beam line is instrumented with a set of detectors to monitor the beam and to trigger the data acquisition system: scintillator trigger counters (S1–S3), wire chambers (BC1 – BC2) measuring the position of the beam particles in both transverse directions and a Cherenkov counter for particle identification. Their position is also shown in Fig. 1.

The beam monitor detectors are described in the following:

- Cherenkov counter:
  A 1 m long threshold Cherenkov counter filled with helium gas in the VLE beam line (CHRV2, VLE) separates pions from electrons. The Cherenkov counter in the HE beam line (CHRV2,HE) was not operational.

- Beam wire chambers:
  Delay multi–wire chambers equipped with two orthogonal wire planes measure the position of the beam particles transverse to the beam line (beam profile).

  The spatial resolution of the wire chambers is 200 μm. The chamber BC–2 is placed on the VLE beam line just after the dipoles selecting the momentum and the Cherenkov counter. The chambers BC–1 and BC0 are placed after the VLE beam line jointly with the HE beam line and before the focusing quadrupole magnets. In this analysis only BC–2, BC–1 and BC0 are used.

- Trigger scintillators:
  Various scintillators are used to trigger events and to select single particles. The scintillator S1, installed after the quadrupole magnets, has a size of $10 \times 10 \times 0.6$ cm^3, the scintillators S2 and S3 have a size of $5 \times 5 \times 1$ cm^3 and where installed in such a way that the overlap in y was about 2.5% cm.

- Muon scintillator:
  The muon veto (SMV) is a scintillator that is installed to tag and to veto unwanted muons from the HE beam line during data taking with the VLE beam line. This counter was, however, not operational. The muon halo (SMH) is a scintillator with a small hole with a diameter of 3.4 cm in the middle where the beam can pass through, but particles in the beam halo are tagged. It has a dimension of $40 \times 40 \times 2$ cm^3. Behind the first beam dump the muon tag, $\mu_{\rm tag}$, (SMT) is installed to trigger or tag particles, like muons, that can penetrate all previous detectors and the beam dump. It has a size of $30 \times 32 \times 1.5$ cm^3.

2.4. The Inner Detector System

The inner detector system consists of a pixel (Pixel), a silicon strip detector (SCT) and a straw tube tracker (TRT) [7].

A Pixel module consists of a single silicon wafer with an array of 40×400 μm^2 pixels. The pixel detector is made of six modules organised in three compartments and two sectors. The distance along the beam axis between the compartments and the location of the modules mimic the arrangement of the modules in ATLAS. Each module has an active size of $z \times y = 60.8 \times 16.4$ mm^2 and is positioned at an angle of about 20^o with respect to the incident beam. Modules in the same compartment overlap by 200 μm. The overall active area covered corresponds to a box with side sizes of 175 mm (in the x–direction), 250 mm (in the y-direction) and 180 mm (in the z–direction).

	LAr				TileCal	
	PS	Front	Middle	Back	A, BC	D
$\Delta\eta$	0.025	0.003	0.025	0.05	0.1	0.2
$\Delta\phi$	0.1	0.1	0.025	0.025	0.1	0.1

Table 1: Cell segmentation of the presampler and the three LAr and TileCal compartments in the $\eta \times \phi$ plane.

A SCT module is built from four single–sided silicon micro–strip sensors glued back–to–back in pairs of 40 mrad stereo angle, for a space point reconstruction in three dimensions. Each module produces two hits, one in each direction. The modules correspond to the ones used in the ATLAS end–cap. They have variable pitch size. The SCT consists of four compartments with two modules per compartment covering an area of $z \times y = 120.8 \times 60$ mm^2. There was a 4 mm overlap between the modules in each compartment. The two middle modules are centred vertically with respect to the beam axis, the first and the last ones are off–set by $y = -5$ mm and $y = 5$ mm. The overall active area covered corresponds to a box with side sizes of 330 mm (in the x–direction), 300 mm (in the y-direction) and 200 mm (in the z–direction).

The TRT consists of straw drift tubes filled with an active gas interleaved with transition radiators. Two ATLAS barrel wedges (each with three modules) are used. Each wedge is equivalent to 1/32 of the circumference of a cylinder with inner radius of 1080 mm and an overall length (along the z–axis) of 1425.5 mm. The angular coverage is $\Delta\phi = 28.125°$ starting at $\phi = -17.365°$.

In addition to tracking information, the TRT provides information on the amplitude of the measured signal in a straw encoded in two different thresholds. When the low threshold is passed, a hit in the straw is indicated. When in addition the higher threshold is passed, it is likely that a transition radiation (TR) photon interacted with the gas. Such TR photons are emitted by particles with a very high Lorentz gamma–factor ($\gamma > 1000$), thus essentially only electrons. This feature allows for a good separation of electrons and pions.

2.5. The LAr Barrel Calorimeter

The details of the ATLAS LAr barrel calorimeter are described elsewhere [8, 9, 7]. In the CTB one LAr module was installed. A module is made out of accordion–shaped lead absorbers glued between two 0.2 mm thick stainless steel sheets placed into a cryostat containing liquid argon. The read–out electrodes are interleaved between two absorbers. The lead of the absorbers have a thickness of 2.21 mm and the electrode size is 0.275 mm. A high voltage of 2kV is applied between the absorbers and the electrodes.

The module is longitudinally segmented into three compartments, each having a different transverse segmentation. The cell granularity of the three LAr calorimeter compartments is given in Table 1.

At $\eta = 0.45$, the front, middle and back compartments have thicknesses of 0.32 λ, 0.962 λ and 0.074 λ, respectively[2].

A thin presampler detector (PS) is mounted in front of the accordion module. It consists of two straight sectors with cathode and anode electrodes glued between plates made of a fibre–glass epoxy composite (FR4). The electrodes are 13 mm long. The gap between the electrodes is 1.93 mm.

2.6. The Tile Calorimeter

The details of the ATLAS TileCal are described elsewhere [10].

The iron–scintillator media of the TileCal modules is made of 4 and 5 mm thick iron plates sandwiched by 3 mm thick scintillator tiles, with a periodicity of 18 mm. The total thickness of the iron and the scintillator in a period is 14 mm and 3 mm, respectively. The tiles are oriented perpendicularly to the module length, i.e. they are placed parallel to the direction of the impinging particles. Each side of the scintillating tiles is read out by a single wavelength–shifting (WLS) fibre. The fibres are grouped together, separately for each side, forming a cell, that is read out by two photo–multipliers (PMT). The fibres are joined in bundles such that projective towers pointing to the ATLAS interaction region are formed.

[2]The variable λ denotes the nuclear interaction length for protons.

Each TileCal module represents one azimuthal segment of in total 64 modules used for the complete barrel and extended barrel assembly of the TileCal in ATLAS (see for details ref. [7]). The TileCal has a granularity of $\Delta\eta = 0.1$ and $\Delta\phi = 0.1$. Only the last compartment has a coarser η granularity (see Table 1). Eleven tile sizes are used in the structure of the barrel modules, grouped into clusters of $3 + 6 + 2$ tiles, defining three longitudinal compartments A (front), BC (middle) and D (back) with depths of 1.5, 4.1 and 1.8 λ at $\eta = 0$, respectively.

2.7. Combined Detector Set–up

A sketch of the lay–out of the ATLAS sub–detectors installed in the combined test–beam and additional beam monitor detectors in the beam line is shown in Fig. 2.

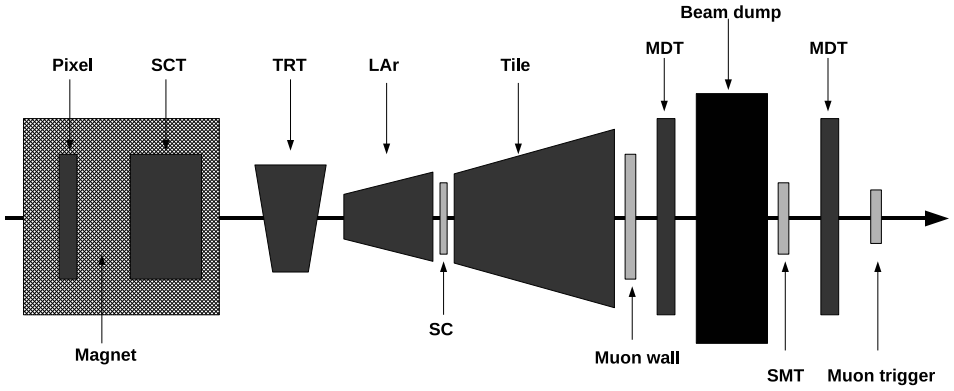

Figure 2: Sketch of the ATLAS sub–detectors and additional beam monitor detectors in the H8 beam line. The particle beam enters from the left.

The beam particles enter first the inner detector system (ID) composed of three compartments of six pixel modules (Pixel) and four compartments of two silicon tracker modules (SCT) and of two wedges of the barrel TRT. The Pixel detector and the SCT are surrounded by a magnet that is able to provide a magnetic field of 2 Tesla[3]. The TRT detector is placed outside the magnetic field. The distance between the last SCT compartment and the first TRT plane is 1114 cm.

After the inner detector one LAr module housed in a cryostat filled with liquid argon is placed on a movable table together with three TileCal barrel and three extended barrel modules stacked together[4]. The distance between the two calorimeters is approximately 30 cm. This is about 5 cm longer than it is in the ATLAS detector.

The movable table allows to change the angle and the position of the modules relative to the incident beam to emulate particles impinging on different impact points in η at $\phi = 0$. The particles impinge projectively (in η) as they were coming from the ATLAS interaction point.

The cryostat housing the LAr calorimeter consists of an inner and an outer aluminium wall with thicknesses of 4.1 cm and 3.9 cm, respectively. The two walls are separated by a vacuum gap. Between the cryostat and the calorimeter module a foam block (ROHACELL) is installed to exclude LAr in front of the calorimeter.

The LAr module covers a range of $0 < \eta < 1.4$ and $-0.2 < \phi < 0.2$ rad. The three TileCal modules cover a range of $-0.15 < \phi < 0.15$ rad and $-1 < \eta < 1$.

For a beam impinging at a pseudo–rapidity $\eta = 0.45$ the amount of material in front of the LAr, for the LAr and TileCal calorimeters and of the dead material in between the two calorimeters is given in Table 2. The length of the calorimeter layer is given in Table 2.

After the calorimeter system several test–station of the ATLAS muon spectrometer (MDT) have been installed, but have not been used in this analysis.

[3]For the data–set analysed here the magnetic field was switched off.

[4]After the test–beam data taking the LAr module and the lowest TileCal module remained in the test–beam area, the two upper TileCal modules have been integrated in the ATLAS detector.

	LAr				TileCal			
start of layer	1	2	3	DM	A	BC	D	DM
λ	0.44	0.76	1.72	1.79	2.42	4.03	8.56	10.6

	DM	LAr	DM	TileCal
λ	0.44	1.35	0.63	8.18

Table 2: Top: Longitudinal segmentation of the amount of material in the detector system. Quoted is the cumulative amount of material at the start of each calorimeter layer or the dead material (DM). The numbers are given in units of nuclear interaction lengths and corresponds to the material a particle, that impinges at $\eta = 0.45$, passes. Bottom: Amount of dead material (DM) in front of the LAr calorimeter, the length of the LAr and the TileCal calorimeter layers and the amount of dead material between the two calorimeters.

3. Reconstruction of the Energy Measured in the Calorimeter

The energy for each calorimeter cell is reconstructed from digitised samples of the signal from each read–out channel. The measured signal is calibrated such that the reconstructed energy corresponds to the deposited energy at the electromagnetic scale (measured in MeV). The electromagnetic scale is defined to reconstruct correctly the energy deposited by electrons and photons in the calorimeter.

3.1. Cell Energy Reconstruction of the LAr Calorimeter

The electronic calibration of the LAr calorimeter in the CTB is described in detail in ref. [11].

The ionisation signal from the calorimeter is brought via cables in the LAr out of the cryostat to the front–end crates. These crates, directly located on the cryostat, house both the Front End Boards (FEB) to read out the ionisation signals and the calibration boards to inject a well–known calibration pulses of known amplitude on the detector, to be used to measure the cell signal response and the electronic gains.

On the FEB, the signal is first amplified by a current–sensitive preamplifier. In order to accommodate the large dynamic range and to optimise the total noise (electronics and pile–up), the signal is shaped to a bipolar form and split in three linear gain ratios, called low, medium and high gain. For a given channel the signals are sampled at the 40 MHz clock frequency by a 12–bit ADC and stored in an analog pipeline (Switched Capacitor Array) until the trigger decision. After a trigger, a predefined number (N) of samples (S_i) is digitised.

To equalise the response dispersion of the electronics readout and the different capacitance of each calorimeter cell, the calibration board provides to all channels an exponential signal that mimics the calorimeter ionisation signal and probes the electrical properties of each cell.

The cell energy is reconstructed from the digitised samples of the ionisation signal using:

$$E_{\mathrm{cell}}^{\mathrm{rec}} = F_{\mu A \rightarrow \ \mathrm{MeV}} \cdot F_{\mathrm{DAQ}\rightarrow\mu\mathrm{A}} \cdot \frac{1}{\frac{M_{\mathrm{phys}}}{M_{\mathrm{cali}}}} \cdot \sum_{i=1,2} R_i \left[\sum_{j=1}^{N} \mathrm{OFC}_j \ (S_j - \mathrm{Ped}) \right]^i . \quad (1)$$

The individual terms are explained in the following:

3.1.1. Pedestal Measurement

The pedestal level, Ped, can be determined from dedicated calibration runs with no beam or using random triggers during the data taking of physics events. The latter method is used to correct for the observed drift of the pedestal level during the run (few MeV) due to a varying temperature of the front–end electronics.

3.1.2. Electronic Calibration System

The factor R_i relates the signal amplitude (in ADC–counts) to the corresponding injected current (in DAC–counts). It is obtained by calibration runs where the injected current is changed in small steps ("ramp run"). A higher order polynomial to relate the reconstructed amplitude and the injected charge is used.

The factor $F_{\mathrm{DAQ}\rightarrow\mu\mathrm{A}}$ relates the setting of the electronic calibration system to the current injected to the electronics. It is given by $F_{DAQ\rightarrow\mu A} = 76.3\ \mu\mathrm{V}/R_{\mathrm{inj}}$, where R_{inj} is the resistance of the injection

resistors (about 1 MΩ) depending on the resistor. Since the injection resistors were at slightly different values than the ones used in the reconstruction program, a correction factor 0.9907 is applied to all cell energies in the first compartment (strips).

3.1.3. Signal Amplitude Reconstruction with Optimal Filtering

The amplitude (A) of the sampled signal (measured in the ADC–counts) is reconstructed using a digital filtering technique [12], where the peak amplitude is expanded in a linear weighted sum of coefficients (OFC) and the pedestal (Ped) is subtracted in each sample. The optimal filtering (OF) technique reconstructs the energy and the interaction time from the five measured samples S_i and provides a measure of the quality of the measured to the expected pulse–shape.

To determine the OFCs the physics pulse–shape, its derivative and the auto–correlation noise matrix between the various samples needs to be known for each cell. In the CTB a calibration method is used where the calibration parameters are derived from the injected calibration pulse and applied on the physics pulse [11, 13, 14]. The factor $M_{\rm phys}/M_{\rm cali}$ takes into account that the physics and calibration pulse differ slightly in shape, and are not generated exactly in the same place on the detector.

In ATLAS, detector pulses have a constant timing with respect to the LHC bunch crossing frequency (25 ns) and therefore for each cell only one OFC set is needed. However, in the test–beam particle arrive asynchronously with respect to the data acquisition clock (DAQ) that is 25 ns long. To take the dependence of the physics pulse on the particle arrival time with respect to the DAQ clock into account, 25 OFC sets (one for each bin of 1 ns) are used for energy reconstruction. The correct set is chosen according to the particle arrival time measured by the beam line TDC [11]. There is also a separate set for each of the two read–out gains[5].

3.1.4. Absolute Electromagnetic Scale

The ionisation current is converted to an energy deposited in the liquid argon gap using $1/F_{\mu A\rightarrow \rm MeV} = f_{I/E}\cdot f_{\rm sampl}$, where $f_{I/E}$ is the current to energy conversion taking effects of the electrical field into account and $f_{\rm sampl}$ is the sampling fraction for electrons correcting for the energy deposited in the lead absorber that has been derived from the test–beam analysis of 2002[4]. It depends on the LAr temperature in the cryostat. In 2004 this temperature was precisely known, however in 2002 no precise measurement has been done and the energy scale has been derived by comparison to Monte Carlo simulations. Therefore an energy scale factor for all LAr cells has to be applied to take the different liquid argon temperatures into account. It is empirically determined using electrons with an energy of 180 GeV. In this analysis an overall factor of 1.038 is used. The systematic uncertainty on the absolute electromagnetic scale in the CTB is about 0.8% for the VLE data–set and 0.7% for the HE data–set [6].

3.2. Cell Energy Reconstruction of the Tile Calorimeter

The electronics calibration of the TileCal for the data taking period analysed here is in detail described in ref. [15]. A sketch of the signal chain in the TileCal and the electronic read–out and the calibration system is shown in Fig. 3.

During the CTB two electronic calibrations systems have been operational. The charge injection system (CIS) calibrates the response of the readout electronics and a radioactive caesium source (Cs) is used to measure the quality of the optical response and to equalise the cell response. The laser calibration system was not used in the CTB.

The scintillating light produced in the tiles is transported via wavelength shifting fibres into photo–multipliers (PMT). The PMTs amplify the signal and convert the optical signal into an electrical one. Each PMT channel has two analogue paths: the high and the low gain with approximately 82 counts/pC and 1.3 counts/pC [16]. The read–out electronics shapes, amplifies and digitises the signals from the PMTs. The shaped signals are sampled every 25 ns by a 10–bit ADC.

The cell energy is reconstructed as the average over the two channels each read–out by one PMT. The measured channel energy is reconstructed by:

$$E^{\rm rec}_{\rm chan} = F_{\rm pC\rightarrow\ GeV}\cdot F_{\rm ADC\rightarrow pC}\cdot F_{\rm Cs}\cdot A_{\rm fit}, \qquad (2)$$

[5] At the energies reachable at the test–beam only high and medium gains are used. In ATLAS a third gain (low gain) is used.

where $A_{\rm fit}$ is the peak height corrected for the baseline of the samples measured as a function of time t (see section 3.2.1), the factor $F_{\rm pC\rightarrow ADC}$ is the electronic calibration factor (see section 3.2.2), $F_{\rm Cs}$ corrects for cell non–uniformities using the caesium runs (see section 3.2.3) and $F_{\rm pC\rightarrow\ GeV}$ converts the measured charge to the absolute electromagnetic scale (see section 3.2.4).

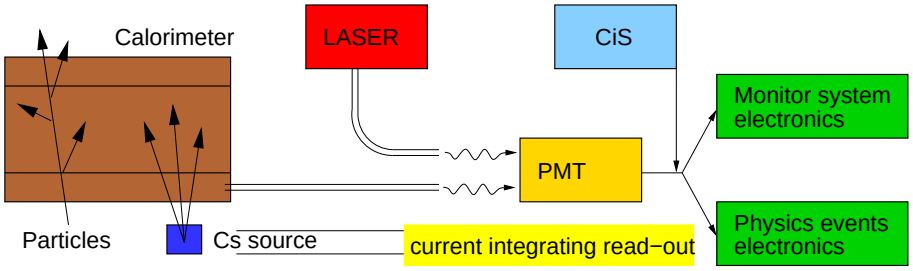

Figure 3: Sketch of the TileCal read–out chain and the calibration scheme.

3.2.1. Signal Amplitude Reconstruction from the Samples

The amplitude $A_{\rm fit}$, the baseline (pedestal) $P_{\rm fit}$ and the time[6] $\tau_{\rm fit}$, when the energy was deposited, is extracted by adjusting a parametrised pulse–shape $g(t)$ to the samples (S) (in ADC–counts) measured as a function of time t:

$$S(t) = A_{\rm fit}\ \ g(t - \tau_{\rm fit}) + P_{\rm fit}. \tag{3}$$

The reconstructed energy is given by $A_{\rm fit}$ that corresponds to peak height corrected for the baseline.

The pulse–shape is extracted using signals from pions depositing about 100 GeV in TileCal cells taking advantage of the asynchronous particle arrival time with respect to the DAQ clock. For each gain one pulse–shape is used.

Channel–to–channel variations of the pulse–shape are mainly observed in the few last signal samples (late sampling times). To reduce these variations only the first five samples are used in the fit. However, the pulse–shape slightly depends on the amount of the deposited energy and this can result in a misreconstruction of the peak amplitude by up to 1%. Since this effect is similar for the physics and the calibration pulse, the energy dependence of the physics pulse–shape is taken into account by the CIS calibration.

3.2.2. Electronic Calibration with the Charge Injection System

The electronics can be calibrated injecting a known charge at its input, i.e. the signal after the PMT. More details on the charge injection system (CIS) can be found in ref. [16].

Each channel is calibrated using calibration capacitors[7] that provide a well defined charge at the input of the read–out electronics. For a given input charge the signal amplitude is reconstructed using a dedicated pulse–shape corresponding to the calibration pulse[8], and taking into account a leakage pulse caused by the discharging mechanism.

In dedicated calibration runs the full range of charges is scanned and the relation between the injected charge and the reconstructed amplitude is determined. The maximal deviation of the ratio of the peak amplitude to the injected charge is about 2% in the low region of the low gain (around 110 pC). Using a simulation of the read–out electronics complemented with test bench measurements it was possible to show that this non–linearity is due to a cross–talk between the saturated high gain and the low gain branch of the read–out electronics.

The gain correction proceeds in two steps: first, a linear calibration factor is derived for each channel and for each gain and then the residual non–linearity (in the range from 10 to 500 pC) is corrected by a look–up table representing the average residual (over all channels).

[6] In case of a very small signal the time is fixed and only two parameters are fitted.

[7] The capacitances are chosen to be $5.2 \pm 2\%$ pF and $100 \pm 1\%$ pF.

[8] Since the calibration pulse is slightly faster that the one produced by a charged particle in the detector, the resulting form of the injected pulse is similar. However, the amplitude of the calibration pulse is 10% larger and the full width half maximum is 10% smaller than the one from the physics pulse.

In most regions the total uncertainty on the charge measurement on a single channel is at the level of about 1%. At low signals in low and high gain the main uncertainty is due to the resolution of the ADC and can reach a few percent for charges lower than 1 pC (high gain) and between 10 and 30 pC (low gain). The uncertainty of an energy measurement involving several cells is smaller than 1% over the whole covered energy range. Details of the electronic calibration and the associated systematic uncertainties can be found in ref. [16].

3.2.3. Cell Equalisation with a Caesium Source

The Caesium equalisation system [17, 18] monitors the quality of the optical response of each Tile calorimeter cell. It is used to adjust the PMT high voltage to equalise the response of all cells to a 0.5% level. The analysis of the calibration data also allows the derivation of additional cell corrections that can be applied off–line.

Differences in the cell response due to variations of the scintillator material, the optical fibres or connectors are equalised using special calibration runs where a Cs–137 γ–source that is moved by a hydraulic system orthogonally to the tile planes through a hole in the scintillating tiles, and passes every single scintillating tile and absorber plate. At the same time the current of each PMT is measured with integrating electronics[9].

The signal of each individual tile is determined assuming an energy sharing modelled by a function with a Gaussian core and an exponential tail, and by taking into account that part of the Cs–signal is measured in the neighbouring tiles[10] and that at the cell edges part of the signal is lost ("amplitude method").

The single tile response can be reconstructed with a precision of 2%, the average cell amplitude with a precision of 0.3%. In the CTB, the stability of the cell response during a period of four months was about 1% [15]. From the response of each cell to the Cs–signal the cell correction factor F_{Cs} given by the response of a given cell with respect to the average of all cells in the modules, can be determined and applied off–line when reconstructing the cell energy.

3.2.4. Absolute Electromagnetic Scale

The response of about 10% of the TileCal modules installed in the ATLAS detector has been studied using electron test–beams in 2002 and 2003 [19]. The average response to high–energy electrons impinging at a polar angle of 20^o on the TileCal measures the calibration factor $F_{\mathrm{pC}\rightarrow\ \mathrm{GeV}} = 1.05 \pm 0.003$ pC/GeV. and defines the "electromagnetic scale"[11].

The cell–to–cell variation, including the long–range variations between modules is $2.4 \pm 0.1\%$. The dominant part of the residual cell non–uniformity of about 2% for electrons is due to differences in the optical properties of the tiles and of the read–out fibres (intra–cell) [12].

Since the electron beam can only be used to calibrate the edge cells of the TileCal, a cell inter–calibration procedure based on the Cs–system is needed to equalise the BC and D cells with respect to the A cells. However, the cell inter–calibration can not be based on the Cs–signal alone, but also needs to take geometrical effects into account. Since the cell length increases along the direction parallel to the nominal particle impact direction, the distances between the Cs–holes get longer towards the end of TileCal and therefore, due to light attenuation in the tiles, the Cs–signal is more and more decreased. This effect can be measured using muons that impact the TileCal from the side and only travel in one tile row by comparing muons impacting different tiles [19]. The need for such a correction has also been shown on a test bench using a Strontium source scanned along the tiles [20]. The average measured correction for the three longitudinal compartments is given in Table 3. The correction factors are applied to each TileCal cell.

[9] The Cs calibration system uses a different read–out than the standard one. This is reason why the Cs–system can not provide an absolute energy calibration, but only gives the relative cell–to–cell calibration.

[10] The calibrated tile is the one closest to the source at a given moment. Typically 80% of the energy is measured in this tile and 20% in the neighbouring ones.

[11] Due to the varying size of the tiles and the iron absorber as a function of the particle impact point, the electrons response varies by about 5% between small angles $\eta = 0$ and large angle $\eta = 0.65$[19].

[12] Such differences can be determined by the Cs–calibration system, but not corrected for, since the smallest read–out entity is a cell and the particle impact on the cell is not known a–priori.

TileCal compartment	A	BC	D
Longitudinal weight	1.00	0.977 ± 0.002	0.919 ± 0.006

Table 3: Longitudinal weights applied to the TileCal compartments to correct for varying cell lengths not taken into account in the cell inter–calibration procedure. The energy calibration of the first TileCal compartment (A) is not changed.

The resulting rms spread of the pion response is $1.5 \pm 0.4\%$[15]. This spread includes the cell–to–cell and the module–to–module variation. The cell–to–cell pion response variation within one module is about 0.6–0.7%. It is mainly due to tile–to–tile differences estimated to be 0.5% and due to the uncertainty in the charge–injection calibration that contributes with 0.42%.

The absolute pion response uncertainty is estimated to 1% [15]. It is mainly due to variations in local module response and uncertainties in the charge–injection and caesium calibration.

3.3. Topological Cluster Algorithm

A detailed description of the topological cluster algorithm can be found in ref. [21]. Clusters group together nearby energy depositions that are likely to be caused by the same impinging particle. They are an efficient way to describe the topology of the energy depositions in the calorimeter. Clusters are derived from calorimeter cells by adding the energy in neighbouring cells using a dynamical topological cluster algorithm. The final, reconstructed object is called "topological cluster". The properties of clusters can be used for particle identification and energy calibration.

The algorithm starts with a seed cell, the cell with the highest (absolute) energy not yet included in a previously found topological cluster. All the cells in the neighbourhood of the cluster are included, if they have an (absolute) energy larger than a predefined threshold (neighbour threshold). The procedure is repeated until no cells in the neighbourhood of the cluster above the noise threshold are found. As a last step all cells surrounding the cluster, if they pass another predefined threshold (perimeter threshold), are also assigned to the cluster.

In the default configuration seed cells are required to have an energy larger than $S = 4$ standard deviations (σ) of the expected noise, neighbouring cells $N = 2\sigma$ and all perimeter cells are included ($P = 0\sigma$). The cut is applied on the absolute cell energy measured on the electromagnetic scale such that the energy measurement is not biased by the noise contribution[13]. In the following the default setting ($S = 4$, $N = 2$, $P = 0$) are used. The influence of the noise thresholds on the pion response is studied in detail in ref. [22].

The reconstructed cluster energy is obtained as the sum over the energies of all cells assigned to the cluster.

[13] In this way negative and positive noise cancels and the sum over all noise cells is zero.

Momentum (GeV)	η	Geometry					
		Far mat	Lead	Pixel	Al	SCT	Al
< 12.5	0.442	no	no	yes	no	yes	no
< 35	0.434	yes	yes	yes	no	yes	no
< 75	0.439	yes	no	yes	no	yes	no
< 150	0.438	yes	yes	yes	no	yes	no
< 250	0.431	yes	no	yes	10 mm	yes	20 mm

Table 4: Geometry used to simulate the test–beam set–up. Given is the pion energy range, the pseudo–rapidity impact point of the beam particles, the presence of far material (Far mat) consisting of air, beam line windows etc., a lead plate (Lead) to absorb electrons in the beam line, the presence of the Pixel and the SCT detectors and of two Aluminium plates (Al) between the Pixel and the SCT detector that have been installed for testing purposes.

4. Data-Set

The data used in this analysis were taken in September 2004, when all detectors were operated in the combined test–beam. Events are triggered by the S1 and S2 scintillators. A veto on the muon halo and the muon veto scintillator is applied on-line. Runs with beam momenta ranging from 2 to 180 GeV are used. No magnetic field was used to deflect the beam particle. The beam impinged on the calorimeter system at an angle corresponding to a virtual angle in the ATLAS experiment of $\eta = 0.45$ and $\phi = 0$. The beam with a momentum of 20 to 180 GeV are secondary beams while all other beam momenta are tertiary beams. The particles in the momentum range from 2 to 9 GeV are produced in the VLE beam line. The beam particle charge was negative[14]. In the following data (or simulations) with beam momenta between 2 and 9 GeV are called VLE (very low energy) data–set, HE (high energy) data–set for beam momenta from 20 to 180 GeV.

The HE and VLE data–set are listed in Table 5. For each nominal particle momentum the run number, the nominal particle type, the nominal and measured beam momentum, the electrical charge, the total number of events available and the number of selected and identified electrons and pions are given. The measurement of the beam momentum is described in section 2.2. The selection of events is explained in section 6.

In the VLE beam line the particle type is not well–defined by the beam setting and the nominal particle type is therefore labelled e/π. When available, a nominal electron (labelled e) or nominal pion (labelled π) run is used to select electrons or pions, respectively. For higher beam momenta $P_{\text{beam}} \geq 20$ GeV for nominal pion beams (labelled π) a piece of lead is installed in the beam line such that most of the electrons do not reach the scintillator trigger. For these beam momenta nominal electron runs (labelled e) are used to provide the electron control sample. The selection of identified pions and electrons is described in section 7.1.

For the run at 180 GeV only a nominal electron run is available and the pions contaminating the electron beam are selected[15]. In addition, for this run some aluminium plates were introduced before and after the SCT. For pions such changes in the geometry have only a small effect. In the MC simulation these geometry changes are taken into account (see Table 4). The TRT position in the VLE runs was at $y = 112$ mm while for the HE runs it was at $y = -8$ mm.

[14]The H8 VLE beam line can be operated with positively and negatively charged particles. It was explicitly checked that negative charge was selected.

[15]In the H8 beam line the pion contamination in nominal electron runs is relatively large.

Run-Nr	type	$\langle\eta\rangle$	$P_{\text{beam}}^{\text{nom}}$ (GeV)	$P_{\text{beam}}^{\text{meas}}$ (GeV)	charge	N_{events}	$N_{\text{electrons}}$	N_{pions}
2102099	e/π	0.443	2	2.05	$-$	390000	22498	1692
2102115	e/π							
2102117	e/π							
2102098	e/π	0.443	3	3.05	$-$	200000	16655	2891
2102097	e/π	0.443	5	5.09	$-$	200000	15983	7330
2102095	e/π	0.443	9	9.04	$-$	200000	10761	14299
2102096								
2102392	π	0.44	20	20.16	$+$	130000	14	20668
2102393								
2102394								
2102395								
2102396								
2102397	e					100000		16437
2102343	π	0.44	50	50.29	$+$	230000	17	58822
2102345	π							
2102347	π							
2102403	e							
2102410	e					200000	31930	
2102353	π	0.436	100	99.8	$+$	180000	4	40893
2102354								
2102355								
2102398	e					200000	26205	
2102225	e	0.432	180	179.67	$+$	110000	3060	12168

Table 5: Run number, nominal particle type, average pion impact point in the η–direction, nominal and measured beam momentum, charge of the beam particle, total number of events available and number of identified electrons and pions. Runs with equal particle type and beam particle momentum have been merged. The total number of events and identified particles refer to the merged data–set and is quoted for the first run of a given momentum and particle type.

5. Monte Carlo Simulation Tools

The Monte Carlo simulation models the interaction of particles with the detector material on a microscopic level. The visible deposited energy for each particle passing through the active part of a calorimeter cell is recorded and the energy deposits for this cell are summed up. This signal is convoluted with a model of the detector response including signal reduction due to saturation, the effect of the electrical field and of the electronic read–out chain.

The models to simulate particle interactions with the detector material are described in section 5.1. The simulation of the detector response is discussed in section 5.2.

5.1. Modelling of Particle Interactions with the Detector Material

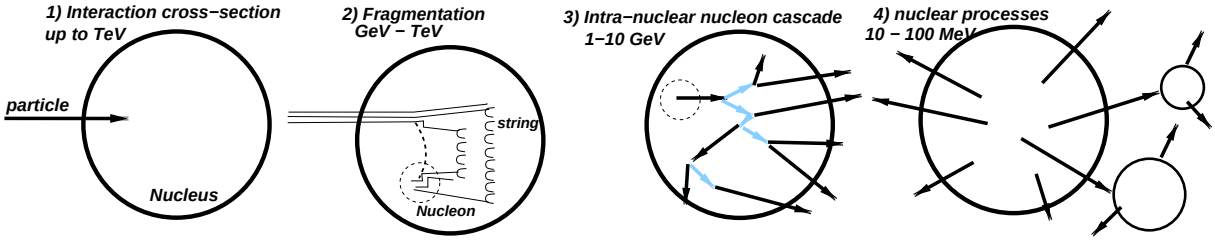

Figure 4: Sketch of the main strong interaction types needed to describe the interaction of hadrons in the detector material, along with their applicable energy ranges.

Physics list	Particle	Hadron energy range		
		Low (GeV)	Medium (GeV)	High (GeV)
QGSP	p,n,π		0–25 LEP	> 12 QGSP
QGSP_BERT	p,n,π	0–9.9 BERT	9.5–25 LEP	> 12 QGSP
QGSP_BERT_NQE	p,n,π	0–9.9 BERT	9.5–25 LEP	> 12 QGSP
QGSP_BERT_TRV	p,n,π	0–5.4 BERT	5.0–25 LEP	> 12 QGSP
QGSP_BERT_HP	n	0.02–9.9 BERT	9.5–25 LEP	> 12 QGSP
	p,π	0–9.9 BERT	9.5–25 LEP	> 12 QGSP
QGSP_BIC	p,n	0–9.9 BIC	9.5–25 LEP	> 12 QGSP
	π		0–25 LEP	> 12 QGSP
QGS_BIC	p,n	0–9.9 BIC	9.5–25 LEP	> 12 QGSP
	π	0–1.3 BIC	1.2–25 LEP	> 12 QGSP
QGSP_BIC_HP	n	0.02–9.9 BIC	9.5–25 LEP	> 12 QGSP
	p	0–9.9 BIC	9.5–25 LEP	> 12 QGSP
	π		0–25 LEP	> 12 QGSP
FTFP	p,n,π	0–5 LEP		> 4 FTF
FTFP_BERT	p,n,π	0–5 BERT		> 4 FTF
FTF_BIC	p,n,π	0–5 BIC		> 4 FTF

Table 6: Kinematic range of validity for the hadron interaction models used in the various physics lists in Geant4. Physics lists labelled with HP use a high precision model for neutron interactions at low energies, i.e. below 20 MeV.

The simulation of the particle interactions with calorimeter modules is performed within the ATLAS software framework ATHENA[16] using the Geant4 [17] simulation tool–kit [23].

The tracking follows all particles down to zero kinetic energy. However, to improve application performances, Geant4 implements a production cut: electrons, positrons and gammas are created from an interaction, if they have enough energy to travel a minimum expected travel path (range), typically

[16] Version 12.0.95 is used.
[17] Version 9.1 patch0 is used.

1 mm. The value of the production cut is tuned in a way such that the CPU performance of the application is improved without deterioration of the simulation quality. Besides purely electromagnetic processes, hadron interactions and photo–nuclear interactions are also simulated. Neutrons are followed in detail up to 10 μsec. After that time all their energy is deposited at their current location.

Fig. 4 shows a sketch of the four phases needed to model the strong interaction of a hadron with a nucleus. The hadron interaction is modelled in four different ways depending on the energy range:

1. Interaction with the nucleus:
   The probability of an interaction is determined from parametrised experimental cross–sections (up to 10 TeV). The reaction cross–sections for various processes (nuclear fission and capture, elastic and inelastic scattering) are parametrised using the Axen–Wellisch [24] or the Barashenkov [25] parametrisation in case of inelastic reactions. The total cross–section is given by the Barashenkov [25] parametrisation.
2. Fragmentation of the nucleus:
   The fragmentation of the partons produced in the hadron nucleon collision is simulated and the types, energies and directions of the produced particles are defined ($\approx$ 10 GeVto 10 TeV).
   For the fragmentation one can either use the Low Energy Parametrised (LEP) or the High Energy Parametrised (HEP) model or phenomenological fragmentation models based on strings: the quark gluon string (QGS) model [26, 27, 28, 29, 30], or the Fritiof (FTF) model [31, 32, 33, 34].
   Since Geant4 version 8.3 the inelastic hadron–nucleus scattering is complemented by quasi-elastic (QE) scattering, where a nucleon scatters elastically on a nucleon in the nucleus. This process takes about 5–10% of the total cross–section and therefore decreases the contribution from deep–inelastic scattering (based e.g. on QGS).
3. Intra–nuclear cascades:
   The interactions of the hadrons in the medium of the nucleus are modelled using intra–nuclear nucleon cascades (1 to 10 GeV).
   For the intra–nuclear cascade either the Bertini (BERT) [35, 36, 37] or the binary cascade (BIC) [38] model is available. In addition, elastic scattering of protons and neutrons is included, mainly based on parametrisation of forward and backward diffractive cross–section measurements.
4. Nuclear processes:
   The remnants of the nuclei are de–excited or split via spallation, break–up, fission etc. (1 – 100 MeV). At this stage a sizable number of nucleons, preferentially neutrons, can be evaporated. The binding energy to release these nucleons is taken from the initial hadrons. The total amount of energy absorbed through nuclear processes can be as high as 20 – 40% and fluctuates significantly event–by–event.
   For the de–excitation of the remnant nuclei and for nucleon-nucleus interactions the pre–compound model (P) is used in the energy range of 0 – 200 MeV[18]. Once an equilibrium is reached in the nucleus, nuclear evaporation and break–up are modelled. In addition, capture of particles at rest in nuclei and nuclear decays are simulated in a crude parametrised way or, for all physics lists except LHEP and only for negatively charged particles, using the chiral invariant phase space (CHIPS) model. Precise models for neutrons transport and neutron nucleus interactions based on data tables are available within the high–precision neutron model (HP) for neutrons from thermal energies up to 20 MeV.

In the following the main hadronic interaction models are shortly described:

- Low and High Energy Parametrised Model (LEP and HEP):
  The LEP model for interactions of hadrons at low energies and the HEP model for higher energies use parametrisation of measured and extrapolated reaction cross–sections, particle spectra and multiplicities for the simulation of the hadron showers. Several parameters have been tuned in a global fit to describe a large amount of hadron–hadron scattering data.

  The parametrised models provide fast simulation, but baryon and meson resonances are not produced and the secondary angular distributions for low energy reactions of O(100 MeV) can not be

[18] Physics lists with the binary cascade included make use of pre–compound model only below 45 MeV kinetic energy.

described in detail. Also, energy and momentum conservation is not ensured for each interaction. This model is a re–implementation of the GHEISHA model in Geant3.21 [39].

- Quark Gluon String Model (QGS):
  The QGS model[26, 27, 28, 29, 30] describes hadron–nucleus interactions by selecting the collision partners from the nucleus, splitting the nucleon into quarks and di–quarks and forming and fragmenting excited strings. As a last step the nucleus is de–excited.

  The hadron–nucleon cross–sections are calculated in the quasi–eikonal approximation and assuming parton density distributions for the hadrons and the nucleons. The probability of an inelastic collision with a nucleon is calculated using the Regge–Gribov approach[40]. The initial interaction is modelled via Pomeron exchange that mediates the strong interaction[19] (dashed line in Fig. 4b). The Pomeron trajectories (describing the energy and spin dependence of the coupling) have been obtained from fits to data.

  Strings are constructed (from the Pomerons) between the quarks from the projectile or from the target nuclei following the colour flow. The quarks from the projectile and the target are generated from the parton density distributions derived from hadron structure functions.

  Hadrons are produced from the strings by successively breaking strings into hadrons until the string mass is so low that two hadrons can be created. The transverse momentum distribution of the hadrons is sampled from a Gaussian distribution with an average of 500 MeV; the longitudinal momentum distribution is sampled from fragmentation functions obtained from data.

- Fritiof fragmentation model (FTF):
  The FTF model[31, 32, 33, 34] is a string–dynamical hadronic interaction model without colour exchange. It foresees an exchange of the longitudinal momenta of the initial hadrons leading to two independent highly excited final state strings that are fragmented according to the Lund model[41].

  When two hadrons collide a chain of dipoles is created. Each dipole carries a fraction of the total hadron energy and the dipoles can exchange momentum.

  The momentum transfers between the hadrons is represented by independent and incoherent scattering between pairs of dipoles. Unless there is a hard scattering in the event, there is no re–ordering of the dipole chain, i.e. no quantum numbers are exchanged.

  The final state after the collision consists of two excited hadron states. Highly excited mass states are possible, even if the transverse momentum exchange is very small, because the longitudinal momentum exchange can be large. If the masses of the excited states are minimal, diffractive events are produced. In this case the momentum transfer between the two systems falls off exponentially. The decays of the excited states are handled with the Lund fragmentation model. The rapidly separating colour charges also cause the emission of gluons.

  Nuclei are modelled as ensembles of nucleons subject to Fermi motion within the nucleus, while taking the nuclear binding energy into account. An impinging hadron that passes through the nucleus produces a set of independent collisions with the nucleons. In each collision the impinging hadron and its collision partner loses longitudinal momentum.

  Interactions of the produced hadrons with each other are not taken into account.

- Bertini nucleon–nucleon scattering (BERT):
  The Bertini model handles the intra–nuclear hadronic interactions of hadrons[20] with kinetic energies below about 10 GeV, and then de–excites the residual nucleus.

  The Bertini model is based on classical scattering. The hadron–nucleon cross–sections and the angular distributions of the emerging particles are taken from experimental data. The nucleus is modelled via step–like nuclear density distributions.

[19] The Pomeron describes in the Regge–Gribov approach the interaction of two hadrons in the t–channel. In the interaction no quantum numbers are exchanged. Characteristic of a Pomeron exchange is that the cross–section slowly rises with energy towards high energy.

[20] The scattering can be initiated by protons, neutrons, pions or kaons.

The projectile is then transported along straight lines through the nuclear medium (see Fig. 4c) and interacts according to the free hadron–nucleon total cross–section. The nuclear medium is approximated by concentric constant–density shells. At the shell boundaries a particle can be reflected or transmitted. The secondaries from the initial or subsequent interactions are also propagated in the nuclear medium and interact until they leave the nucleus.

During the cascade excited residual nuclei are formed, which can evaporate neutrons or alpha particles and radiate photons due to inter–nuclear transitions, as well as undergo weak decays with subsequent de–excitation (see Fig. 4d).

- Binary nucleon–nucleon scattering (BIC):
  A 3D–model of the nucleus placing nucleons in space according to nuclear densities is used. The nucleon momenta are taken from a Fermi gas model. The incident particles and subsequent secondaries are propagated through the nucleus along curved paths according to the equation of motion in the nuclear potential. Hadron–nucleon collisions are either elastic[21] or form a resonances (such as delta particles and higher mass states up to about 2 GeV), which decay according to their quantum numbers. The kinematics is based on $2 \rightarrow 2$ or $2 \rightarrow 1$ interactions with the target nucleus.

  The resonances can either interact or decay. The cascade stops when the mean energy of all scattered particles is in the range of 10 to 20 MeV.

Within the Geant4 simulation framework several models can be used to simulate the interaction of particles with matter. The applicability of the model depends on the particle type, the energy range and the target material. A sketch of the available interaction models and their approximate energy range is shown in Fig. 5.

A "physics list" is a consistent collection of models that covers the interaction of all particles in the whole energy range from thermal energies up to several TeV. Depending on the application, the required physics performance and the available computing time, different physics lists can be chosen.

The range of applicability of the available models to compose a physics lists for each particle type is shown in Table. 4. In the overlap region of two models, one model is chosen based on a linearly varying probability. The lower (higher) value gives the energy point where only the model valid at lower (higher) energies is used.

[21] At low energies elastic hadron–nucleon scattering is the only possibility.

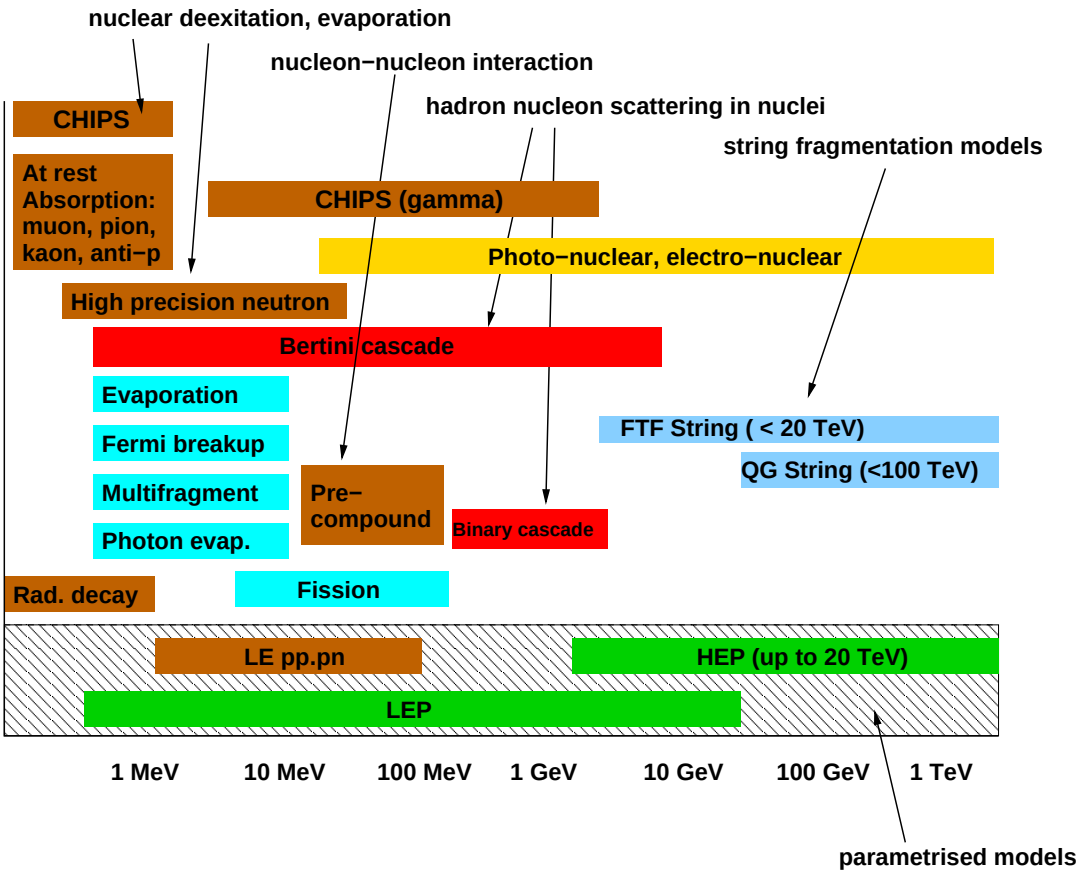

Figure 5: Sketch of the models used to simulate hadronic interactions depending on the energy of a particle in a hadron shower. The dashed area indicates the parametrised models.

5.2. Modelling of the Detector Response

5.2.1. The LAr Calorimeter

The simulation set–up of the LAr calorimeter module is based on an ensemble of lead absorbers and electrodes arranged in an accordion shape. The absorber thickness[22] is about 2.21 mm , the Lar drift gap is 2.1 mm and the electrode thickness is 0.275 mm. The electrode is made out of a mixture of copper and kapton. The absorber is constructed from an effective material representing a single mixture of lead, iron and glue. The free space between the absorbers and the electrodes is filled with liquid argon. The material of the spacers (honeycomb) is neglected.

The visible energy deposited in the liquid argon for each calorimeter cell is recorded.

Recombination of electrons produced in the liquid argon depending on the electrical field are included in an effective way using current maps from which the fraction of charge reaching the electrodes is calculated as a function of the position of the energy deposition. The drift time is taken into account. Measured values from ref. [42] are used.

The maps of the induced current are calculated taking into account the distortion of the electric field in the accordion structure. Normalisation factors equalising the response in the regions of uniform electrical field are applied to ensure correct inter–calibration of the accordion compartments.

Recombination effects for high ionising charged hadrons depending on the amount of deposited energy are emulated using Birks law[23] [44, 45]. The response reduction of the deposited energy E_0 to the measurable energy E is parametrised as:

$$\frac{E}{E_0} = \frac{A}{1 + k\ dE/dx}, \tag{4}$$

where dE/dx is the deposited energy of the particle and the parameter k is set to $k = 0.0486$ (g/cm^2) MeV[24]. The overall normalisation parameter is taken such that the response for electrons is not changed, i.e. $A = 1.008$. The choice of the parameters and the implementation is discussed in ref. [46].

Effects of the electronics chain are taken into account in the digitisation step. The signal is simulated and then reconstructed as it would be in real data. This takes into account possible biases from the energy reconstruction algorithm, from the ADC conversion, gain switch, etc.. The sampling fraction used to convert the energy deposited in the liquid argon to the total electromagnetic energy (including the absorber) is $f_{samp} = 0.1667$ [11].

Simulation and digitisation in the LAr calorimeter is described in detail in ref. [47, 48].

5.2.2. The Tile Calorimeter

The simulation of the TileCal uses the detailed structure of the scintillating tiles and the iron absorber.

The simulation of the TileCal scintillators includes saturation effects modelled according to Birks law and the effects of photo–statistics in the photo–multipliers. However, no attempt is made to describe the detailed optical properties of the scintillating tiles and the read–out fibres. Also the light attenuation between the two PMTs is not modelled. A simple linear interpolation is used to distribute the energy to the PMT on each cell side. The maximal drop of the signal between the two PMTs of a cell due to non–linearities is not larger than 5%.

The response attenuation of organic scintillators due to quenching can be taken into account according to:

$$\frac{E}{E_0} = \frac{1}{1 + k_1\ dE/dx + k_2\ (dE/dx)^2}, \tag{5}$$

where $k_1 = 0.013$ g/(MeV cm^2) and $k_2 = 9.6 \cdot 10^{-6}$ g^2/(MeV^2 cm^4). These values correspond to measurements on organic scintillators[49]. For particles with a charge larger than the elementary charge, such as alpha particles, the parameter k_1 is reduced by 7.2/12.6.

[22] The absorber thickness corresponds to the average of the measured ones[9].

[23] Birks law was originally derived to describe the saturation of scintillators. Later it was found that such a law can also describe saturation effects in LAr calorimeters. For a recent discussion see ref. [43].

[24] The approximation that the electric field is 10 kV/cm through the electrodes is made.

The number of photo–electrons (pe) produced in the photo–multiplier is emulated using a Poisson distribution with a mean of 70 pe/GeV. This number has been adjusted to well describe the width of the muon signal[50].

The sampling fraction to convert the visible energy deposited in the scintillator to the total visible energy deposited in both the active and the passive material used is $f_{\mathrm{samp}} = 1./34.3$.

5.2.3. Calorimeter Noise Simulation

For both calorimeters, the electronic noise was extracted from experimental data using randomly triggered events. A Gaussian parametrisation of the noise is used. The noise is added incoherently to the energy of each cell or PMT in the MC samples. In the LAr calorimeter the noise auto–correlation between different time samples is also taken into account.

In the LAr calorimeter, cross–talk effects between neighbouring cells (between the cells of the first compartment and the ones in the second and the third compartment) are taken into account.

Coherent noise is not simulated, but known to be relatively small [51]. For all data taking periods the same noise is assumed. It has been checked that for the data–set under study here, the measured noise is well described by the MC simulation[50].

5.2.4. Treatment of the Time Structure of Hadron Showers

The energy deposits by particles in a hadron shower can arrive at different times. While the electromagnetic energy component is deposited immediately when the particles interact with the detector, energy deposits caused by neutrons can be several milliseconds later, since thermal neutrons can scatter around in the calorimeter material for a long time. An example of a late energy deposition caused by neutrons is the one by electrons produced in pair–production from photons emitted from nuclei that had been excited by a low energetic neutron.

However, the calorimeter is only sensitive in a certain time window that is defined by the read–out electronics. The typical time where the calorimeter measures energy depositions is 20–30 ns. For both the LAr and the Tile calorimeter, this effect is taken into account in the simulation by determining the energy deposition as a function of the time (in bins of 2.5 ns) and in the digitisation step by convoluting this time profile with the pulse–shape used to reconstruct the energy from the samples.

5.2.5. Simulation of the Inner Detector

The three parts (Pixel, SCT, and TRT) of the ID are described by the centrally administrated GeoModel. GeoModel provides type, amount, and positions of all the material used in the ID, including the active detector parts and the dead material such as structural supports and services.

The Pixel and SCT detectors are modelled by silicon wafers, electronics, cooling, and other services. The Pixel detector consists of three compartments, the SCT of four. The TRT is made up of Kapton/Mylar[25] straws of 4 mm radius containing a gas mixture of O_2, CO_2, and Xe in proportions 3%, 27%, and 70%, respectively. The straws are surrounded by a light stringy radiator material.

The material model is validated through comparison of the GeoModel and the measured weight of the detector parts, which is accurate to a few percent for the barrel part [7].

The energy deposit from physics interactions are converted into an amount of ionisation, which is then drifted to the near–by anode, where it gives rise to a signal. This signal is the output of the digitisation step, and can be compared to the output of the actual detector. The conversion of energy deposits to ionisation includes the recapture probability, drift velocity variations, noise and dead channels, known response of front–end electronics, pulse shaping, and conversion into bits through a threshold (two in the case of the TRT). Unlike the simulation, the digitisation is carried out by custom software packages specific to each sub–detector, due to technological differences between these.

Particularly for the study at hand, the two TRT thresholds in simulation are tuned to match the test–beam data, since accurate calculations are not easily obtainable. The probability of passing the higher threshold (HT) level has an onset at a Lorentz gamma–factor of ≈ 1000, and is well described for all

[25] Kapton and Mylar are trademarks.

particle types by a logistic sigmoid function as follows:

$$p_{\mathrm{HT}}(\gamma) = \underbrace{0.0264 + 0.00025 \times \log_{10}(\gamma)}_{\text{ionisation part}} + \underbrace{\frac{0.153}{1 + \exp(-(\log_{10}(\gamma) - 3.30)/0.270)}}_{\text{transition radiation part}}. \quad (6)$$

The values are obtained by adjusting them to data. The separation between electrons and pions (and on a statistical basis pions and protons) is based on this function.

The use of the transition radiation to identify electrons and pions is discussed in section 7.1.

5.2.6. Simulation of the Combined Set-up

The sub-detectors described above are placed as in the real test–beam set–up (see section 2.1). However, the beam line detectors are not included. The trigger scintillators are not simulated[26].

The simulation also includes the cryostat walls of the LAr calorimeter, the ROHACELL block to exclude the liquid argon before the presampler and the LAr calorimeter. The read-out electronics and cables are simulated in an effective way.

In order to facilitate the simulation of the beam divergence the simulation is started at $x = 1.1$ m. The beam divergence has been measured using tracks in the Pixel and the SCT detector. The polar and azimuthal angles and the closest impact points in the direction transverse to the beam axis are measured and they are included in the simulation. After including the measured beam divergence good agreement with the data is achieved.

For the HE data–set an additional aluminium plate corresponding to $15\%X_0$ ("far material") has been put at 1 m before the point $x = 0$ that would correspond to the beam interaction point in the ATLAS geometry. This models in an effective way the material that is crossed by the beam, i.e. the air, the beam line windows, the Cherenkov counter etc.. This far material is needed to properly describe the energy sharing between the first and second compartment for electrons in the LAr calorimeter in the HE runs [6]. For the VLE data–set no far material needs to be added, since the beam momentum selection is done near the detector set–up.

Effects due to the beam line optics which determine down to which energy a particle can still enter the detector set–up can be calculated using a detailed beam line simulation. Such acceptance corrections are important for electrons, but can be neglected for pions.

5.2.7. Simulated Data–Sets

In the simulation negatively charged pions have been used[27].

A large sample of events was generated for each considered physics list and for each beam momentum and each particle type. The Monte Carlo sample is always larger than the corresponding data sample.

The simulation is done at the nominal beam energy, but in the analysis the cell energy of the simulated events are rescaled to the measured beam momentum given in Table 5. Where necessary, simulated pions and protons samples are mixed together according to the measured proton fraction (see Table 10).

The impact point of the particles to the calorimeter has been adjusted for each run. To exactly reproduce the η and ϕ barycentre of the shower in the calorimeter, a reweighting of the simulated events to the η and ϕ distribution in the data is performed.

Pion decays are taken out of the simulation by removing all muons passing the TRT detector that are produced in a pion decay[28].

[26] The effect of the trigger acceptance is emulated by requiring a long track in the TRT.

[27] It was checked that the Monte Carlo prediction is the same for positively charged pions in the Geant4 simulation.

[28] Since the length of the beam line is different in data and Monte Carlo simulation it is better to evaluate the systematics due to pion decays in the data instead of simulating the pion decay. Moreover, since the trigger acceptance is not correctly modelled, the momentum distribution of the pion decays in the Monte Carlo simulation does not correspond to the one in data.

6. Event Selection

The off-line event selection is based on the beam monitor detectors and the tracking system. It is explained in the following:

1. Scintillator signal compatible with one particle:
   One physics trigger and a signal in the S1 scintillator that is compatible with one charged particle ($150 < \text{S1} < 1000$ ADC–counts) is required. The signal in the muon beam halo scintillator must be smaller than 4000 ADC–counts.
2. Event time in fiducial LAr time reconstruction interval:
   In some of the events the time given by the trigger is close to the beginning or the end of the particle arrival time with respect to the DAQ clock signal that has a period of 25 ns (see section 3.1). In this case the LAr reconstruction can not choose the correct OFC parameter set with the required precision and therefore such events are rejected[29].
3. Particle close to the beam line:
   Three beam chambers are used to remove particles that are in the halo of the beam: BC–1 and BC0 for all data and, in addition, BC–2 for the VLE data.
   First the two beam chambers BC–1 and BC0 in the HE beam line are aligned with respect to each other and then the difference in each of the transverse directions is required to be within three times the root-mean-square of the distribution (see ref. [5, 6] for more details). Different values are used for the VLE and the HE data–sets. To ensure that a particle passes through the VLE beam line, a hit in BC–2 close to the beam line is required.
4. No coherent noise in the presampler:
   In some of the events the presampler cells were subject to bursts of coherent noise[30] that changed the pedestal values in either the positive or the negative direction affecting most of the channels in the module. In such cases, a large number of cells can be included in a topological cluster (see section 3.3) and the sum of all presampler cells can be very large (positive or negative). To remove such events the sum of all cells outside the nominal η beam impact point, η_{nom}, ($\eta_{\text{nom}} + 0.1 \leq \eta_{\text{cell}} \leq \eta_{\text{nom}} - 0.1$) should be smaller than 3 GeV or larger than -3 GeV.
5. One good track in the full tracking system:
   The track reconstruction provides tracks in the three individual tracking detectors (Pixel, SCT and TRT) as well as global tracks where the hits in the three subsystems are fitted together. Because of residual alignment problems, the global tracks in some cases do not contain the TRT track. Therefore, both the global and the stand-alone TRT tracks are used to reduce the number of events that interact strongly before or in the tracking system.
   At least one global track with more than six Pixel or SCT hits and one TRT track with more than 30 low threshold hits are required. This requirement ensures that the particle actually passes through the Pixel and SCT detectors and does not, for instance, interact with the (close–by) support structures of these detectors. No other reconstructed TRT track is allowed[31].
   As an example, the TRT hit distribution in the x-y plane is shown in Fig. 6 for an event with a beam momentum of 3 GeV that successfully passes the electron selection (a) and a pion with 2 GeV that did not fulfil the requirements on the total number of TRT hits (b). The pion in Fig. 6b interacts strongly with the TRT material shortly before the end of the TRT and 3–4 outgoing tracks are produced. Two of the outgoing particles have a large number of higher-threshold hits and are therefore likely to be protons at low momenta.
6. TileCal reconstructed time within fiducial volume and no bad TileCal photo–multiplier signal:
   The reconstructed time in the TileCal has to be in a fiducial time range. The time requirement reject off-axis muons from the HE beam line in the VLE data–set. Details are given in section 7.3.1.
   In some of the events, photo–multiplier signals appear in low gain, but have a signal that is compatible with noise[32]. Since for these signals, the energy can not be reliably measured, events are rejected, if such a problem is observed for any of the photo–multipliers.

[29] Technically, this is achieved by requiring that there is at least one reconstructed calorimeter cell.
[30] The coherent noise was correlated to a grounding problem.
[31] Reconstructed tracks in the TRT have more than 20 hits.
[32] The reason for this is unclear. The only explanation put forward for this problem is that it is caused by a change of the signal base–line due to large signals recorded before the event in question.

Selection	Nominal beam momentum in GeV							
	2	3	5	9	20	50	100	180
Event timing:	97.24%	97.27%	97.22%	97.21%	97.20%	97.18%	97.25%	97.07%
Scintillators:	73.66%	74.61%	75.27%	74.88%	80.72%	76.63%	77.01%	72.61%
$E_{\text{min}}^{\text{cluster}}$	-	-	-	-	73.45%	71.86%	64.70%	64.44%
Beam chambers:	28.33%	31.55%	31.52%	28.16%	33.72%	33.46%	31.15%	30.5%
PS coherent noise:	26.84%	30.01%	29.92%	26.73%	31.79%	31.50%	28.70%	30.5%
One good tracks:	14.00%	18.73%	22.55%	25.08%	25.08%	30.28%	27.52%	28.17%
Noise in low gain:	13.80%	17.76%	22.13%	24.61%	–	–	–	–
TileCal Timing :	13.46%	17.76%	21.08%	22.95%	–	–	–	–
Muon rejection:	13.34%	17.61%	20.09%	22.94%	–	–	–	–

Table 7: Fraction of events remaining after each individual selection cuts for each considered beam momentum. The cuts are successively applied from top to bottom. The fraction is given with respect to the total number of events available.

7. Muon rejection:
   To reject muons a signal compatible with noise is required in the muon scintillator downstream of the beam line (μ_{tag})[33]. This muon tagger is able to positively identify muons moving close to the beam axis with an efficiency of 98% [50]. However, its acceptance is not large enough to reject all muons in the beam or the beam halo. Therefore, additional cuts are required.
   In the HE data–set, the sum of the energy in the two topological clusters (see section 3.3) with the highest energy is required to be at least 5 GeV. Such a cut does not bias the pion sample and efficiently removes all muon events.
   In the VLE data–set, muons can not be removed with a cut on the total energy, because the energy deposits from pions are in the same energy range. Besides muons at the beam momentum there are also muons at high momenta produced by the secondary beam. Such muons accidentally pass through the HE beam line and often leave a signal in the calorimeter that does not coincide with the time given by the trigger. Such events are rejected by a cut on the reconstructed time of the TileCal cells, if at least one TileCal cell with a signal above 5 standard deviations of the noise is found outside a small time window (see section 7.3 for more details).
   In addition, muons from pion decays are removed by an estimator constructed from the shape of the expected energy deposition of muons in the calorimeter (see section 7.3.2 and Table 12).

The fraction of events removed by the various selection cuts are summarised in Table 7. The individual cuts are applied one after another from top to bottom. The fraction of remaining events is given with respect to the total number of events available in the run (see Table 5).

The rejection factors are similar for all studied beam momenta. Only the requirement of one long track shows some variation with the beam momentum. The largest fraction of events is removed by the cuts on the scintillator and the beam chambers, which are applied first. The large rejection factors due to the requirement of accepting only particles close to the beam line in the beam chambers is caused by a malfunctioning of the beam chambers that for many events are not able to measure the position of the particles[34].

The requirement of one long track removes about 1% to 10% of the events surviving the cuts applied before. The fraction of rejected events decreases for increasing pion momentum. In the VLE data–set the largest part of the events are rejected by the requirement on the Pixel and the SCT hits. Only about 0.1 to 0.3% of the events are removed by requiring a long TRT track. However, in the HE data–set the amount of events removed by the Pixel and SCT requirement and the one of the TRT is about equal[35].

[33] Since the pedestal is different in the two data–sets, for the VLE data, $370 < \mu_{\text{tag}} < 400$ ADC–counts and for the HE data $360 < \mu_{\text{tag}} < 450$ ADC–counts is required.

[34] Technically, this can be recognised by a zero in the TDC signal of the beam chambers that is used to reconstruct the position where the particle crossed the wire.

[35] Only at 20 GeV about 5% of the events are removed by the TRT requirement.

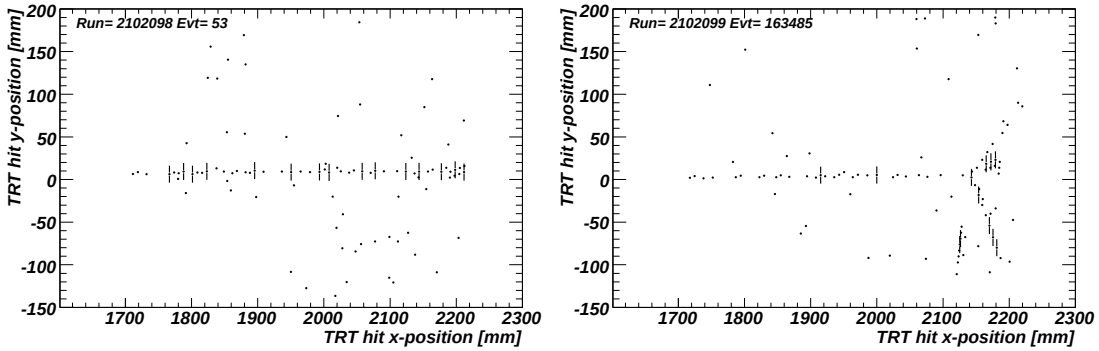

a) b)

Figure 6: Example of the hit distribution in the TRT in the x-y plane for an identified electron with a beam momentum of 3 GeV (a) and for an identified pion at 2 GeV (b). The pion event does not pass the event selection criteria on the number of TRT track hits, the electron does. Each dot corresponds to a TRT hit passing the low threshold. The small vertical lines denote a TRT hit that passes the higher threshold.

7. Particle Identification

The hadron beams produced at the H8 beam line contain in general a mixture of electrons, muons, pions, protons and, possibly, also kaons. The beam composition depends on the beam momentum, the used target (primary, secondary or tertiary) and the beam line optics.

The various detectors in the beam line and the ATLAS inner detector system can be used to identify particles of certain types and can measure the possible contamination by other particle types. In order not to bias the calorimeter response, only minimal use is made of the calorimeter itself for particle identification.

7.1. Electron and Pion Identification

Electrons are separated from pions using the Cherenkov counter in the VLE beam line and the TRT. Since these detectors are uncorrelated and can provide rather clean samples of pions and electrons, they can be mutually used to determine the purity of the selected sample.

The pressure of the Cherenkov counter gas can be set such that electrons give a large signal while pions give a signal compatible with noise. A large Cherenkov signal is therefore likely to come from an electron while a low signal from a pion. The TRT detector is also able to identify electrons using transition radiation[36] (TR) interacting with the Xenon in the TRT straws. Transition radiation leads to a larger number of signals above the higher threshold (HT). The probability for an electron to produce a HT hit is typically 18–20%, while it is 3–4% for other particles (mainly caused by fluctuations in the energy deposit (dE/dx)), depending on Lorentz γ–factor (see Fig. 9a). The number of higher-threshold (HT) track hits of a given track (N_{HT}) can therefore be used to separate electrons from pions.

In the HE data–set, where no Cherenkov counter was available, the identification of electrons and pions is achieved by using the number of HT hits in the TRT and the fraction of the energy in the LAr calorimeter to the total energy ($E_{\mathrm{LAr}}/E_{\mathrm{tot}}$). The energy is obtained from a sum over all topological clusters in the event. The selection criteria are summarised in Table 8.

In the VLE sample the separation of pions from electrons is more difficult, since the signals are more similar, but one can make use of the presence of a Cherenkov counter. The distribution of the Cherenkov counter signal for beam momenta of 2, 3, 5 and 9 GeV is shown in Fig. 7. The distribution of the HT hits is shown in Fig. 8. The closed points show the distribution of the data with all event selection cuts applied (see section 6). There are clearly two distinct classes of events corresponding to electrons and pions.

Since the Cherenkov counter and the TRT provide independent measurements, the purity of the signal can be obtained from two control samples where electrons and pions with high purity are selected. The

[36]Transition radiation is emitted when a charged particle passes the interface between two materials with different dielectric constants. The effect is only significant at high Lorentz γ–factor (> 1000), and thus is mostly caused by electrons.

Data–set	VLE				HE	
Particle type	electron		pion		electron	pion
Selection	standard	control	standard	control	standard	standard
Cherenkov (ADC counts)	> 650	> 850	< 600	< 580		
Number of HT hits (N_{HT})	> 5	> 8	< 3	< 2	> 5	< 3
$E_{\mathrm{LAr}}/E_{\mathrm{tot}}$		> 0.99			> 0.99	< 0.99
$E_{\mathrm{LAr,1}}/E_{\mathrm{LAr,2}}$		> 0.6		< 0.3		

Table 8: Selection criteria to identify electrons and pions in the VLE and HE data–sets. Given are the values to select the standard data sample (standard) and the control samples (control) with a very high particle type purity.

P_{beam}	Cherenkov		TRT	
(GeV)	eff_π (%)	cont_e (%)	eff_π (%)	cont_e (%)
2	85.5	5.3	87.8	3.7
3	87.9	1.2	85.8	0.8
5	84.8	0.3	84.8	0.2
9	86.2	0.06	82.5	0.05

Table 9: Efficiency to identify pions (eff_π) and the residual electron contamination (cont_e) in the standard pion sample selected with the Cherenkov counter signal and the number of higher threshold hits in the TRT. Since the measurements are independent the combined performance can be obtained my multiplication.

selection criteria of the control sample are given in Table. 8. To improve the purity of the control samples, the ratio of the energy in the first and second compartment of the LAr calorimeter[37] is used in addition to the Cherenkov and TRT selection criteria.

The pure pion (electron) sample is shown as solid (dashed) line in Fig. 7 and Fig. 8. The electron and pion samples are normalised to match the distribution of all data in the low and high signal regions, where the purity is high. The sum of the normalised control samples describes the distribution of all events well. The pion–electron separation becomes more difficult towards lower energy.

The shape of the control samples can be used to determine the best selection criteria for the standard sample. For test–beam analysis it is important that a sample with high purity is selected and enough events are retained to study the calorimeter response. The chosen selection cuts are summarised in Table 8.

The efficiency and purity of the obtained standard event sample can be determined using the shape of the normalised control samples by counting the number of selected events in both samples. This method assumes that the residual contamination in the control samples is negligible[38]. The results are summarised in Table 9.

The pion selection efficiency is about 85% for the Cherenkov counter and the TRT separately. Generally, the electron contamination increases towards low beam momenta. The electron contamination is 0.25% for simultaneous cuts on the Cherenkov and the TRT. The relative statistical uncertainty on the results in Table 9 is typically about 1% for efficiencies and about 10% for contaminations. The number of selected pion and electron events is given in Table 5.

[37] The energy is reconstructed in a standard electron cluster using the cells corresponding to a η and ϕ region of three cells in the middle layer around the cell with the highest energy[4, 11].

[38] Actually at 2 GeV the shape of the pion control sample exhibits some electron contamination. However, the effect on the pion purity of the standard sample is still negligible.

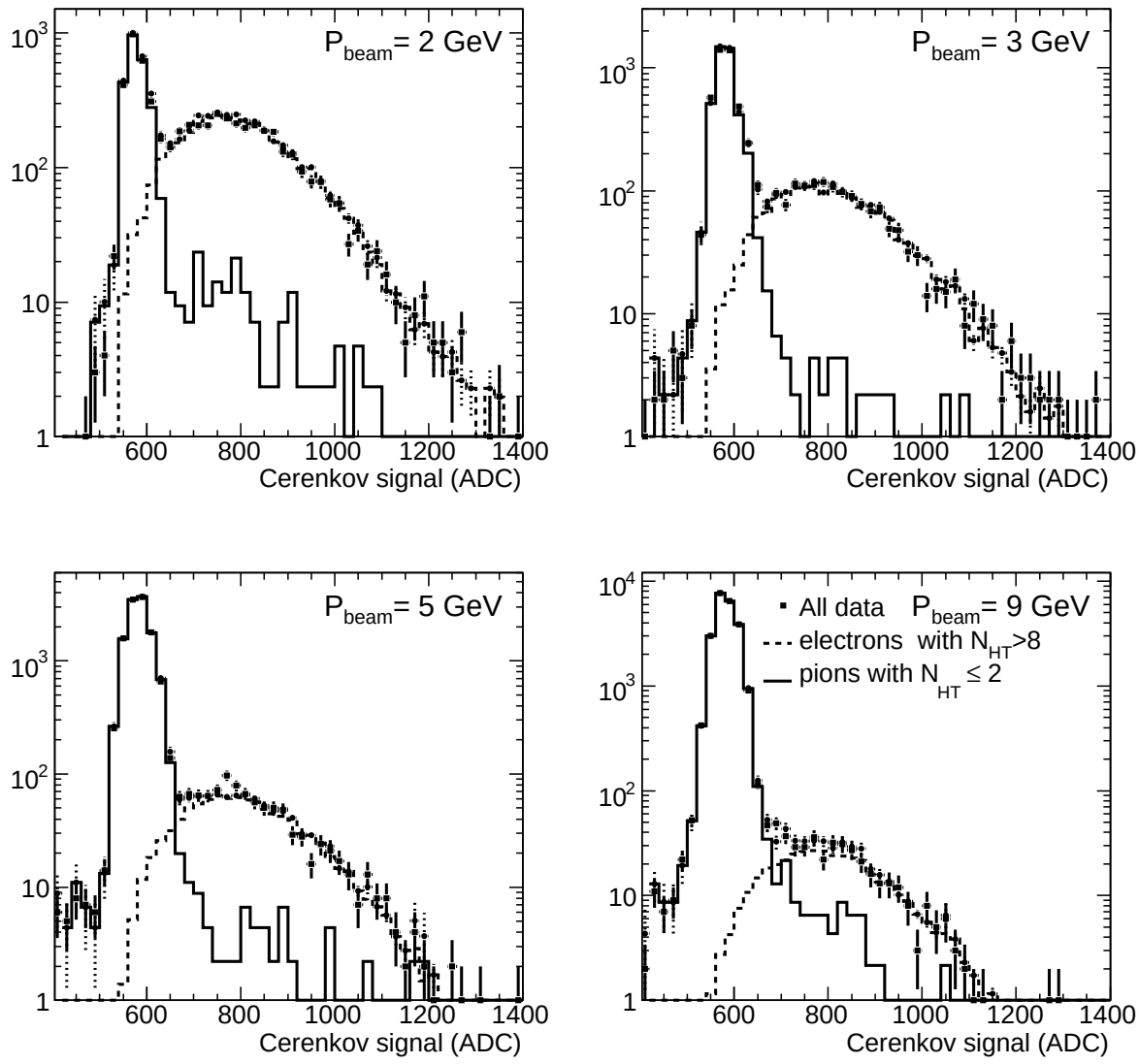

Figure 7: Distribution of the signal measured in the Cherenkov counter (in ADC–counts) for beam momenta of 2, 3, 5 and 9 GeV. Shown are all events after the final event selection except a cut on the Cherenkov counter signal (closed points) and two control data–sets with high purity electrons (dashed line) and pions (solid line). The dotted line close to the data points shows the sum of the normalised electron and pion distribution from the control samples.

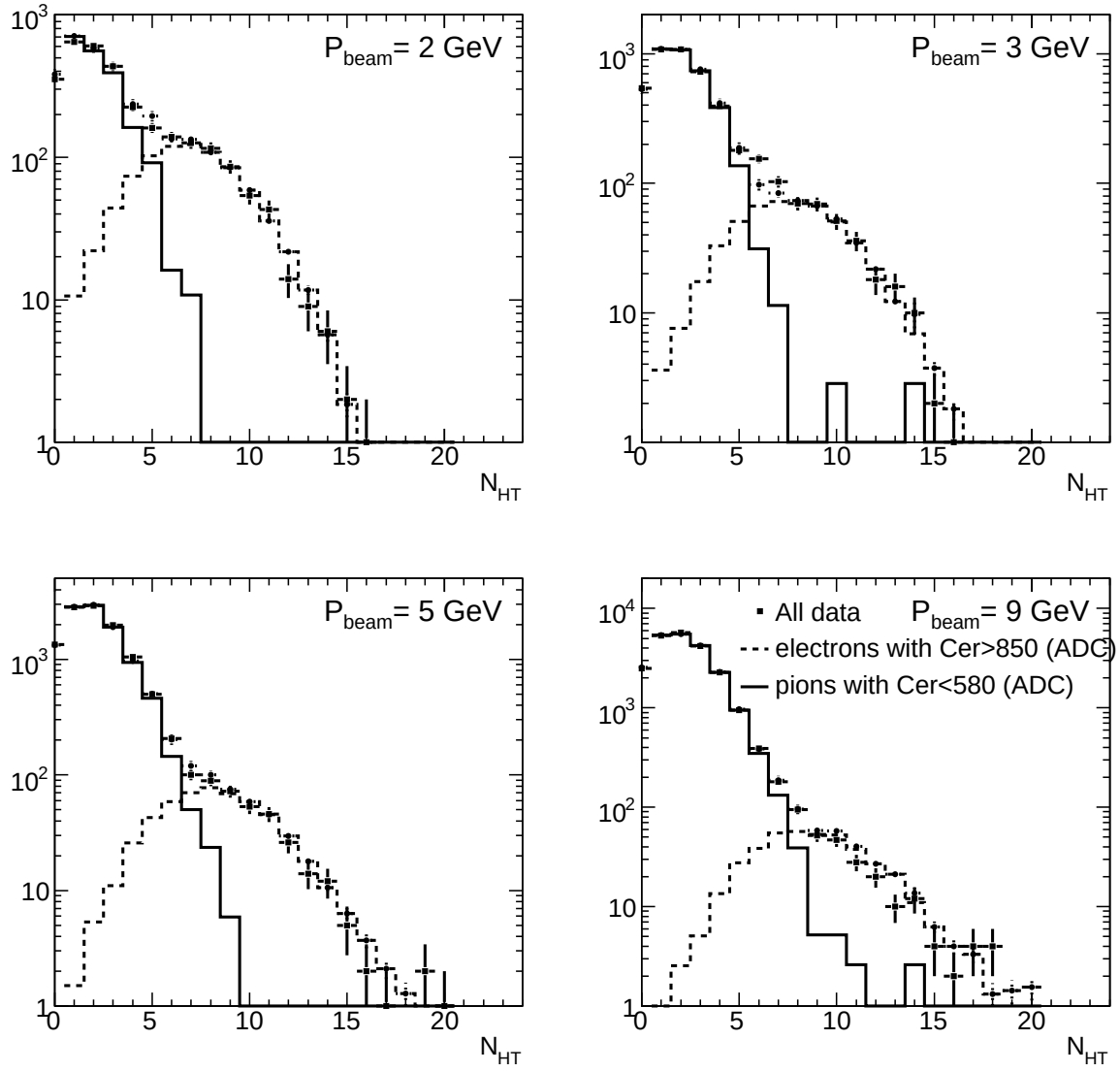

Figure 8: Distribution of the number of higher threshold hits of a TRT track ($N_{\rm HT}$) for beam momenta of 2, 3, 5 and 9 GeV. Shown are all events after the final event selection except a cut on $N_{\rm HT}$ (closed points) and two control data–sets with high purity electrons (dashed line) and pions (solid line). The dotted line close to the data points shows the sum of the normalised electron and pion distribution from the control samples.

P_{beam} (GeV)	P_{HT}^{π} (%)	P_{HT}^{p} (%)	$P_{\text{HT}}^{\text{meas}}$ (%)	f_p
20	3.40	2.98	3.46 ± 0.09	-0.15 ± 0.32
50	4.19	3.12	3.71 ± 0.08	0.45 ± 0.12
80	5.15	3.22	4.07 ± 0.09	0.56 ± 0.07
100	5.83	3.28	4.28 ± 0.08	0.61 ± 0.06
180	8.49	3.56	4.74 ± 0.07	0.76 ± 0.04

Table 10: Proton fraction (f_p) for each beam momentum as calculated from comparing the HT probability $P_{\text{HT}}^{\text{meas}}$ to the expected probabilities for pions and protons ($P_{\text{HT}}^{\pi,p}$). The quoted uncertainties are statistical and systematical.

7.2. Proton Contamination

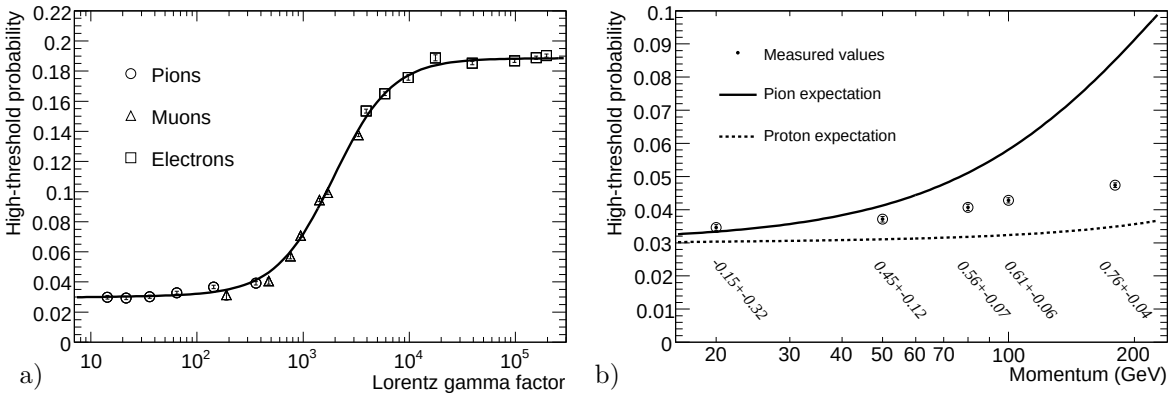

Figure 9: a) Probability that the measured charge of a TRT hit passes the higher threshold as a function of the Lorentz γ–factor of the track for pions, muons and electrons. The line shows a parametrisation used in the analysis. b) Higher threshold probability as a function of the beam momentum. The measured probability is shown as open circles; the closed points show the mean values, together with the uncertainty. The lines show the expected probability for pions and protons based on the parametrisation.

The TRT was designed to identify electrons that emit a large amount of TR due to their high Lorentz γ–factor. The probability that hits from an electron track pass the higher level threshold has already been exploited in section 7.1 to separate electrons from pions.

On a statistical basis this feature can also be used to separate pions from protons at high momenta, since pions begin to emit TR above beam momenta of about 30 GeV, which is not the case for protons (until 300 GeV). Using a test–beam sample of identified muons and electrons at various beam momenta the shape of the HT probability P_{HT} as a function of the Lorentz γ–factor can be measured[7] (see Fig. 9a).

Using an appropriate parametrisation of P_{HT}, the expected HT probability can be calculated for pions P_{HT}^{π} and for protons P_{HT}^{p} (see Fig. 9b). By comparing P_{HT}^{π} and P_{HT}^{p} with the measured probability, $P_{\text{HT}}^{\text{meas}}$, the fraction of protons in the beam can be determined for each run.

The HT probability $P_{\text{HT}}^{\text{meas}}$ was measured in the positive pion runs with beam momenta of 20, 50, 80, 100 and 180 GeV (see Fig. 9b). For each momentum, the fraction of protons in the pion beam (f_p) is then determined as:

$$f_p = \frac{P_{\text{HT}}^{\pi} - P_{\text{HT}}^{\text{meas}}}{P_{\text{HT}}^{\pi} - P_{\text{HT}}^{p}}. \tag{7}$$

The obtained values are summarised in Tab. 10 and also displayed in Fig. 9. The quoted uncertainties are both statistical and systematic. The systematic uncertainties on the proton fraction are due to uncertainties in the shape of the P_{HT} and due to an overall scale uncertainty that takes variations between runs, particle types and event selection into account. The first uncertainty is calculated using a different parametrisation of P_{HT} and is found to be 2.5% on the proton fraction. The other effects are estimated to be 0.1% in P_{HT} and hence depend on the beam momentum.

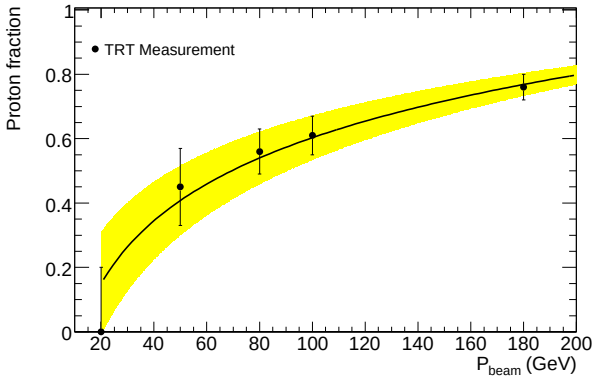

Figure 10: Proton fraction in nominal pion runs as a function of the beam momentum in the H8 beam line. Shown as closed circles is the transition radiation TRT measurement as a function of the beam momentum. The line indicates a parametrisation of the beam momentum dependence adjusted to the data. The band illustrates the uncertainty obtained from repeating the fit from the points offset by the systematic uncertainty.

For the VLE runs negatively charged pions have been used. In these runs there is no proton contamination and the anti–proton contamination is negligible.

Fig. 10 shows the proton fraction as a function of the beam momentum (closed points). The solid line indicates a parametrisation of the dependence of the proton fraction on the beam momentum according to a function of the form $a + b \log P_{\mathrm{beam}}$ that is adjusted to the measurements above or equal 50 GeV. The band illustrates the uncertainty on the parametrisation obtained by shifting the measurements by one standard deviation of their uncertainty up and down and refitting these modified data points.

The results can also be compared to measurements based on a Cherenkov counter in the HE beam line used in the 2002 TileCal test–beam performed in the same beam line[52, 53]. These earlier measurement agree well with the 2004 results for 50 and 100 GeV. At 20 GeV only a beam with negatively charged pions was available. For a beam momentum of 180 GeV the measurement based on the Cherenkov counter in 2002 are lower by 15%. This might be explained by different beam settings[39].

[39] For the 2002 analysis a nominal electron run has been used.

7.3. Muon Contamination

Muons in hadron beams can either stem from pion in-flight decays or be produced at the target and follow the same trajectory as the hadrons. In the VLE data–sets muons can either be produced in the HE beam line and overlay the pion signal or they can be produced by pion decays after passing the VLE momentum selection.

Beam momentum (GeV)	2	3	5	9
$N^{e}_{E_{\mathrm{Tile,D}}>0.35\ \mathrm{GeV}}/N^{e}_{\mathrm{tot}}$ (%)	0.2 ± 0.03	0.4 ± 0.05	0.4 ± 0.04	0.4 ± 0.06
$N^{\pi}_{E_{\mathrm{Tile,D}}>0.35\ \mathrm{GeV}}/N^{\pi}_{\mathrm{tot}}$ (%)	2.4 ± 0.4	5.1 ± 0.4	2.7 ± 0.2	2.6 ± 0.1
$N^{\pi}_{\mathrm{out-of-time\ tail\ shape}}/N^{\pi}_{\mathrm{tot}}$ (%)	1.1 ± 0.3	1.3 ± 0.2	1.5 ± 0.1	1.3 ± 0.1

Table 11: Estimations of the fraction of events with a muon from the high energy beam line overlayed on the triggered event as estimated from the TileCal energy depositions in the last compartment for events with selected electrons (e) and pions (π) and as estimated from an extrapolation of the out–of–time PMT signal distribution in TileCal to the in–time region used in the event selection.

7.3.1. Overlayed Muons from the High Energy Beam Line

In the VLE data–set muons can follow the HE beam line and reach the LAr and TileCal, by–passing the muon veto that was not fully efficient. These muons are displaced with respect to the nominal beam impact point and are not in time. Their momentum is 40 to 80 GeV.

The number of muons in the VLE data–set can be determined using the measured arrival time of the energy deposit in a TileCal cell, since off–axis muons are expected to come at a different time than the particle that sets the trigger. Moreover, it can be estimated from the energy deposits in the last TileCal compartment in events with selected electrons and pions. Each of these methods has a different systematic uncertainty. A more detailed description of the three methods is given in what follows:

1. Estimation based on timing information:
   When the energy is reconstructed for each TileCal cell, the particle arrival time at the cell with respect to the DAQ time (t_{trigger}) is measured (see section 3.2).
   To reconstruct the cell time distribution ($t_{\mathrm{tile,cell}}$), the average of the two PMTs of this cell is used. Only PMTs with a signal well above noise are used ($E^{\mathrm{rec}}_{\mathrm{cell}} > 5\sigma_{\mathrm{noise}}$). The noise level σ_{noise} corresponds to the average PMT noise level measured per Tile layer and is obtained using random events. The time measurement for each PMT is calibrated with the measured arrival time of on–axis particles in the HE data–set measured for each TileCal PMT ($t^{\mathrm{calib}}_{\mathrm{PMT}} = t^{\mathrm{rec}}_{\mathrm{PMT}} - t^{\mathrm{offset}}_{\mathrm{PMT}}$). From this calibrated PMT time the time when the particle passes the trigger with respect to the DAQ clock (t_{trigger}) is subtracted to obtain the final time measurement.
   The calibrated reconstructed cell time is shown in Fig. 11 for beam momenta of 2, 3, 5 and 9 GeV. The normalisation is such that a weight corresponding to the inverse number of PMTs above the required noise threshold in the event is applied for each entry such that each event effectively corresponds to one entry in the time distribution. For selected pion events (solid lines) a peak around 0 ns with a width of about 10 ns is seen. These events arrive in time. Only events for which all cells have measured times between the vertical lines are accepted in the analysis (see section 6). The shape of the time distribution of muons overlayed to triggered events can be estimated from the shape of the measured time distribution for selected electrons (dashed lines). The distribution is normalised to the number of pion events in the tail of the pion distribution. The time distribution of overlayed muons is rather flat. Only for the events with beam momentum of 2 GeV there seem to be more events at positive than at negative times. The out–of–time muon fraction is then given by the normalised number of electron events to the total number of events within the time window. The estimated muon contamination is reported in the last row of Table 11. The estimated fraction of HE muons in the pion sample is 1–2 %.
2. Estimation based on the Tile energy distribution in events with identified electrons:
   The contamination of muons overlayed to the event under study can also be estimated from the number of events with a significant energy measured in the last TileCal compartment for events where an electron has been identified (see section 7.1). For electrons only noise is expected in the

TileCal. The energy in the last TileCal compartment is reconstructed as the sum over all topological clusters and all events with a total energy above 0.35 GeV are counted as muon background.
The estimated muon contamination in the electron sample is reported in the first row of Table 11. For all studied beam momenta the fraction of events with muons from the HE beam line is below 0.5%. Similar results are obtained, if all the cells in the TileCal are used instead of only the energy deposition in the last TileCal compartment.

3. Estimation based on the Tile energy distribution in events with identified pion:
Events with an identified electron can be used to estimate the number of overlayed muons to a good event. However, a muon from the HE beam line can occasionally be the only particle in the event: such events would be identified as pions. This background is suppressed by the requirement that there must be a signal in the BC–2 chamber that is located in the VLE beam line. The remaining background can be estimated using the same method as above using identified pion events. Since the hadronic shower development for pions even at low energies can reach the last TileCal compartment and muons can be produced in a hadron shower, this method gives only the maximal possible muon contamination in the pion sample. Pion decays to muons are also included in this estimate. This background is suppressed with the methods described in section 7.3.2)[40].
The maximally possible contamination of muon from the HE beam line in the pion sample is about 2–5%. The results are given in the second row of Table 11.

In conclusion, after applying strict selection criteria the number of muons passing through the high energy beam line is small. It will be neglected in the following analysis.

[40] For the background evaluation presented in this section the likelihood to identify muons from pion decays has not been applied. With this cut the maximally allowed muon contamination is below 1% for all pion momenta.

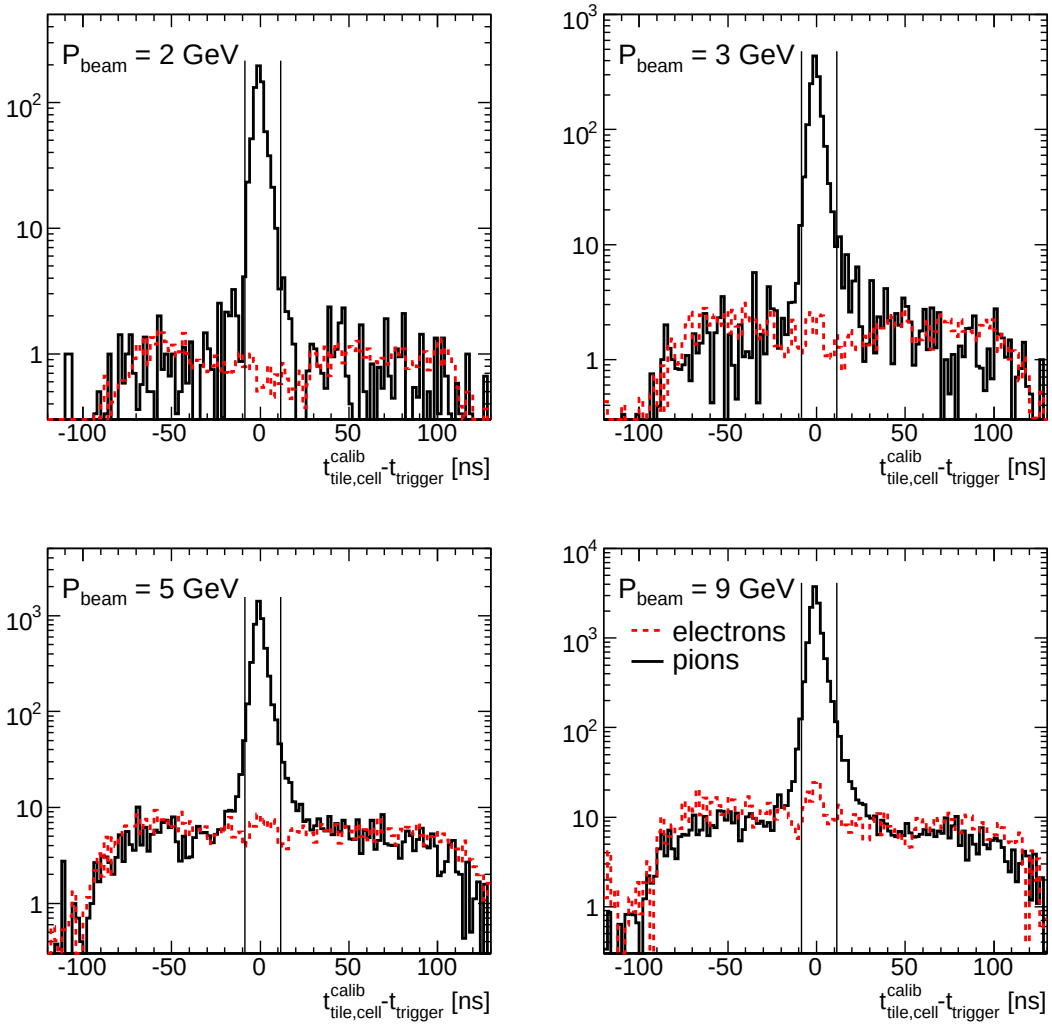

Figure 11: Distribution of the calibrated reconstructed time in each TileCal cells with $E_{\mathrm{rec}}^{\mathrm{cell}} > 5\sigma_{\mathrm{noise}}$ with respect to the time when the particle passes the scintillator trigger for beam momenta from 2 to 9 GeV. Shown are selected pion events (black solid line) and selected electron events (red dashed lines). To represent the background shape the electron events are normalised to the number of pions in the tails. The vertical lines indicate the time window in which all cells of an event have to be accepted.

7.3.2. Muons from Pion Decays

Muons from pion decays have momenta lower or equal to the beam momentum. The pion decay kinematics implies that the muon momentum is between $0.57 < P_\mu/P_\pi < 1$, where P_μ (P_π) is the momentum of the muon (pion). However, the lower the muon momentum the lower the probability that the muon passes through the thin trigger scintillator. From a simulation of the beam line it is estimated that the momentum from muons produced in pion decays peaks near the nominal beam momentum. The lowest momenta are suppressed by the trigger acceptance by about a factor of 5–10 [54].

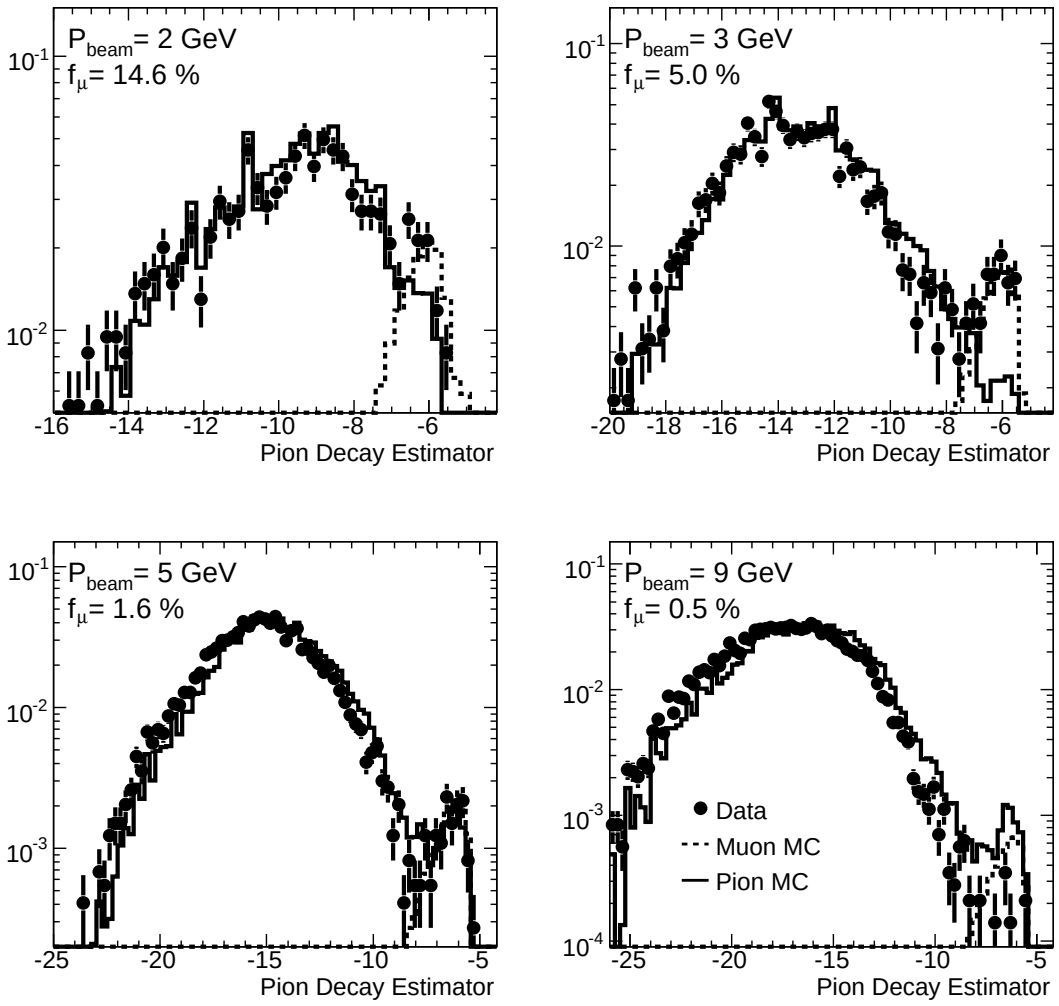

Figure 12: Shape of the pion decay estimator distribution describing, if a pion decays before or in the calorimeter for beam momenta of 2, 3, 5 and 9 GeV. The closed circles denote the data, the solid line shows a pion Monte Carlo simulation (without pion decays). The dashed lines show a simulation of muons at the pion momentum scaled down by the factor f_μ that is given in the left upper corner of each figure.

The energy deposits of a muon from a pion decay can be estimated using a muon simulation. The muon energy deposition in the calorimeter is well reproduced by the Monte Carlo simulation [19, 15, 50]. The mean energy is reproduced to 2% and the energy distribution is reproduced within 10%. The expected signal of a muon in the Tile calorimeter varies from about 2 GeV at low momenta to about 3 GeV at high momenta (200 GeV) [50].

Using a muon simulation the probability that in a given event the energy deposit in the calorimeter

P_{beam} (GeV)	2	3	5	9
f_μ (%)	15.2	5.1	1.6	0.6
PionDecayEst$^\mu$ cut	-7.5	-7.5	-8.0	-8.0

Table 12: Fraction of low energy muons in the pion sample (f_μ) (before applying the selection) and cut values on the pion decay estimator (PionDecayEst$_\mu$) used to select pion events.

compartment i is compatible with a muon (P_i^μ) can be calculated and an estimator that the total energy in the calorimeter is due to muons can be constructed:

$$\text{PionDecayEst}_\mu = \prod_i P_\mu^i, \text{ where } i = 1, 2, 4, 5, 6. \tag{8}$$

The index i denotes the calorimeter compartment, i.e. $i = 1, 2$ for the first and second compartment in the LAr calorimeter and $i = 4, 5, 6$ for the three TileCal compartments. Only in these compartments the signal–to–background ratio is large enough to identify a signal from a muon.

The muon decay estimator has a high value, if the energy deposits in all calorimeter compartments are compatible with the one expected from a muon. The estimator is shown in Fig. 12 for the VLE data–set. The data are shown as closed points. For beam momenta larger than 3 GeV two distinct classes of events are clearly visible. The solid line shows the results of a pion simulation. For not too large values the shape of the data distribution is reasonably well described by the pion simulation. The dashed line shows a muon simulation that describes the peak for large estimator values. The separation of pions and low energy muons works well for beam momenta above 2 GeV.

The fraction of low energy decay muons (f_μ) in the pion sample can be obtained from a fit of the pion and muon simulation to the shape of the data distribution using:

$$\text{PionDecayEst}^{\text{Data}} = f_\mu \ \text{PionDecayEst}_\mu^{\text{MC}} + (1 - f_\mu) \ \text{PionDecayEst}_\pi^{\text{MC}}. \tag{9}$$

In the pion simulation, events where the pion decays in or before the TRT have been removed. However, the sample contains events where the pion decays after the TRT. This explains the peak observed in the pion simulation at large pion decay estimator values. In order to extract f_μ the shape of the pion decay estimator simulation from the region next to the muon peak has been extrapolated using an exponential function.

The fits of the pion decay estimator using the expected pion and muon shapes is shown in Fig. 12. A peak at low likelihood values is clearly visible. The extracted muon fraction from pion decays is summarised in Table 12. The pion decay fraction increases for decreasing beam momentum.

At $P_{\text{beam}} = 2$ GeVthe estimated muon fraction from pion decays is about 15%. For $P_{\text{beam}} = 3$ GeV and $P_{\text{beam}} = 5$ GeVthe muon fraction is 5% and 2%. For $P_{\text{beam}} = 9$ GeV a second peak is only visible in the simulation, but barely in the data. The muon fraction of $f_\mu = 0.5\%$ is overestimated.

The muon estimator is used in the selection of the pion events. The cut values are given in Table 12. The fraction of muons left after the cut is negligible. The values are chosen such that the bias on the pion response introduced by this cut will be included in the systematic uncertainty of the pion response. It is estimated by not applying the likelihood selection.

8. Energy Measurement Uncertainties

The uncertainty on the reconstructed pion energy is calculated taking the cell energy distribution for each event into account. The following main uncertainties in the energy measurement are considered:

1. The absolute energy electromagnetic scale uncertainty in the LAr: 0.8% for momenta below 10 GeV and 0.7% above 10 GeV (see section 3.1.4).
2. The absolute energy scale uncertainty in the TileCal: 1.0% (see section 3.2.4).
3. The uncertainty due to the longitudinal weights of the TileCal (see section 3.2.4 and Table 3).
4. The uncertainty due to the pion decay cut evaluated by using or not using the pion decay cut.

The uncertainty on the absolute electromagnetic scale in the LAr and the TileCal is correlated among all cells and therefore directly influences the pion energy. The uncertainty is calculated by scaling each cell energy with the respective factor up and down. The uncertainties due to the longitudinal weights are evaluated by adding the modified cell energies in quadrature. The considered uncertainties are given in Table 3.

At very low energies the data sample is contaminated by muons from pion decays. These events have a higher energy response and therefore can bias the measurement. They are removed by a cut on the pion decay likelihood (see section 7.3.2) defined on the energy distribution in the calorimeter compartments. Since the likelihood selection also removes some pion events a bias might be introduced. To estimate this bias the pion response can be studied with and without the likelihood cut. This evaluation represents an overestimation of the true effect. The introduced uncertainty on the mean pion response due to the removal of pion decays is 10% at 2 GeV and 3% at 3 GeV and negligible for higher pion momenta. The uncertainty on the beam momentum is about 0.7% and is discussed in section 2.2.

The resulting uncertainties on the response and the resolution are listed in Table 18. The statistical uncertainty is smaller than 1% for all pion momenta. The uncertainty on the energy scale affects the combined pion response by about 0.9%. The uncertainty due to the longitudinal weights is very small.

9. Mean Energy Response and Energy Resolution

In this section the response and the energy resolution are measured and the data are compared to the Monte Carlo simulations. The energy is measured using all topological clusters in the calorimeters using the standard thresholds $S = 4$, $N = 2$ and $P = 0$. The mean energy is given by the average of the energy distribution. The energy resolution is described by the root–mean–square (RMS).

The data are not corrected for proton contamination. Instead, in the Monte Carlo simulation pions and protons are mixed together according to the mean proton fraction as measured in the data.

In section 9.1 the response and resolution is measured for all selected events, i.e. the combined response of the LAr and the TileCal is studied. The total energy distribution as well as the individual energy distribution in the electromagnetic and hadronic calorimeters are presented. In addition, the mean energy fraction contained in the electromagnetic calorimeter is studied. In section 9.2 only events where the pion passes through the LAr calorimeter as a minimally ionising particle are selected and the response and the resolution are measured.

9.1. Combined Response and Resolution of the LAr and the Tile Calorimeter

9.1.1. Combined Total Energy Distribution

The energy distribution measured in the LAr and the TileCal calorimeters for all beam momenta are shown in Fig. 13. Data are shown as closed circles, the Monte Carlo simulation for various physics lists are shown as solid lines. The data are best described by the QGSP_BERT physics list (solid line).

While for high pion momenta the energy distribution is approximately Gaussian towards low momenta the distribution gets a bit skewed towards low values.

9.1.2. Combined Response

The mean response and the resolution as a function of the beam momentum is presented in Fig. 14 and Fig. 15. Data are shown as closed circles, the Monte Carlo simulation for various physics lists are shown as lines. The mean pion response relative to the beam momentum increases from 0.4 at 2 GeV to 0.75 at 180 GeV. The relative resolution improves from about 60% at 2 GeV to about 10% at 180 GeV. The exact numerical values together with the estimated uncertainties are given in Table 18.

Above beam momenta of 10 GeV the pion response increases approximately logarithmically towards higher beam momenta. This can be explained by an increasing energy fraction that is deposited electromagnetically. Below 10 GeV the increase of the response is still approximately logarithmic but the slope is steeper. The shape of the increase of the pion response with the pion momentum is largely influenced by the large relative energy losses in the dead material and the higher relative signal cut by the noise thresholds as well as by the energy leaking out transverse to the shower axis.

The pion response in the data is best described by the QGSP_BERT physics list (solid line). The data are described within 5% in the VLE range and within 1% for higher momenta. The uncertainty for 2 GeV and 3 GeV due to muon contamination is large. The response for the QGSP physics list is about 5 – 10% lower than the one measured in the data. The Fritiof model is about 2–3% too low at high pion momenta ($P_{\text{beam}} > 10$ GeV), but a few per cent too high at low pion momenta(3–5%). As in the case of the QGSP model adding the Bertini cascade increases the response, which is in better agreement with the data at high energy (+1%), but worse at low energies (5–10%). At 5 and 9 GeV the FTFP_BERT model predicts a mean energy that is 10% higher than the one in the data.

Fig. 15a) shows a comparison of the pion response in the data with physics lists using alternative models of the nucleon–nucleon cascades. The variants of the Bertini cascade give little changes in the response. The QGSP model together with the binary cascade (QGSP_BIC) is below the data by about 5 – 10% for VLE data and in agreement with data at high pion momenta. The QGS_BIC is in better agreement with the data than the QGSP_BIC at low momentum. The latter is in slightly better agreement with the data. This means that including a pion nucleon cascade in the low–energetic range gives some improvements. As in the case of the FTFP_BERT physics list, FTF_BIC predicts a response that is too high by 5% to 10% with respect to the data.

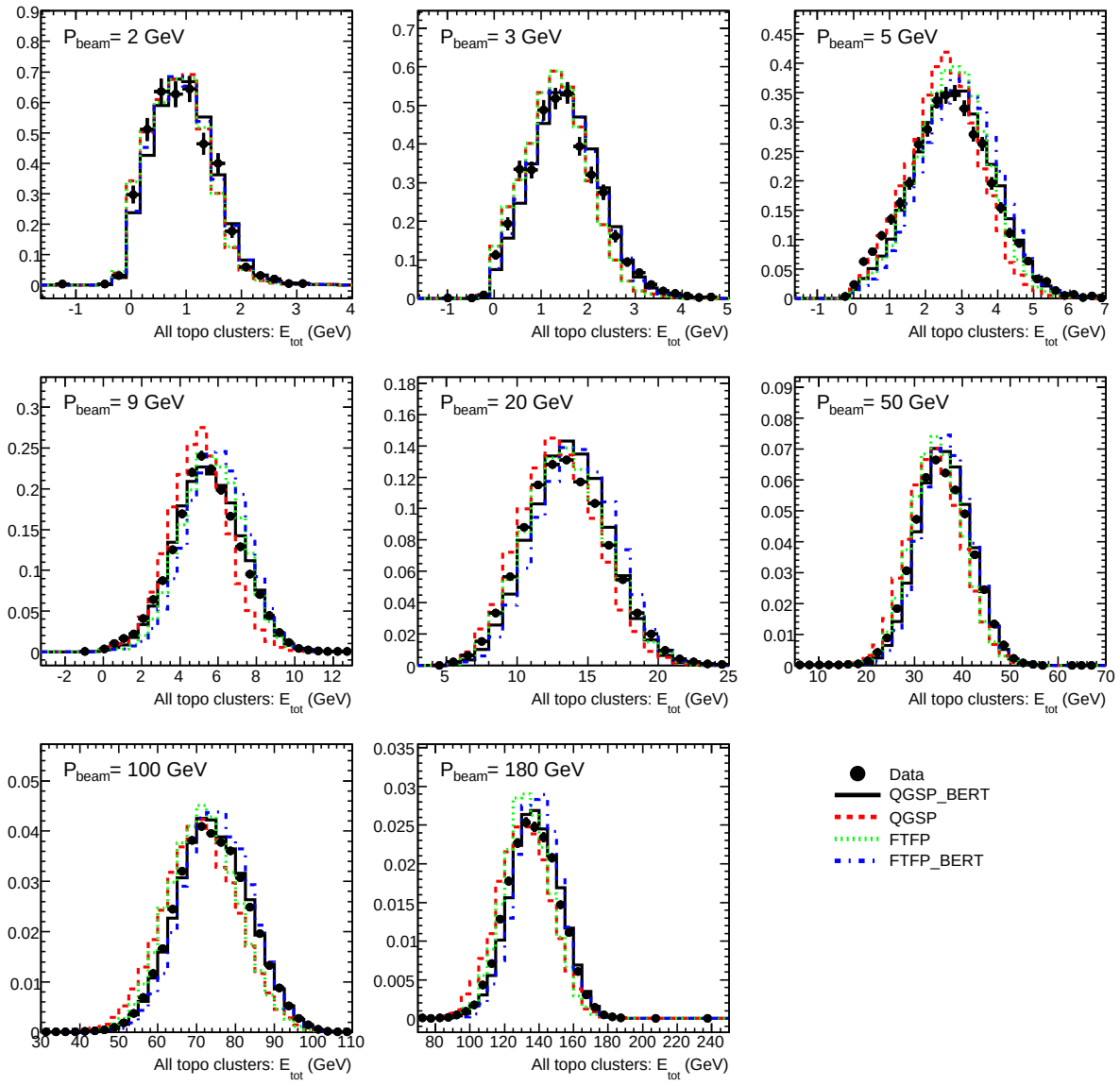

Figure 13: Total energy distribution of pions for beam momenta of 2 – 180 GeV. Data are shown as closed points and Monte Carlo simulations as lines. Only statistical uncertainties are shown.

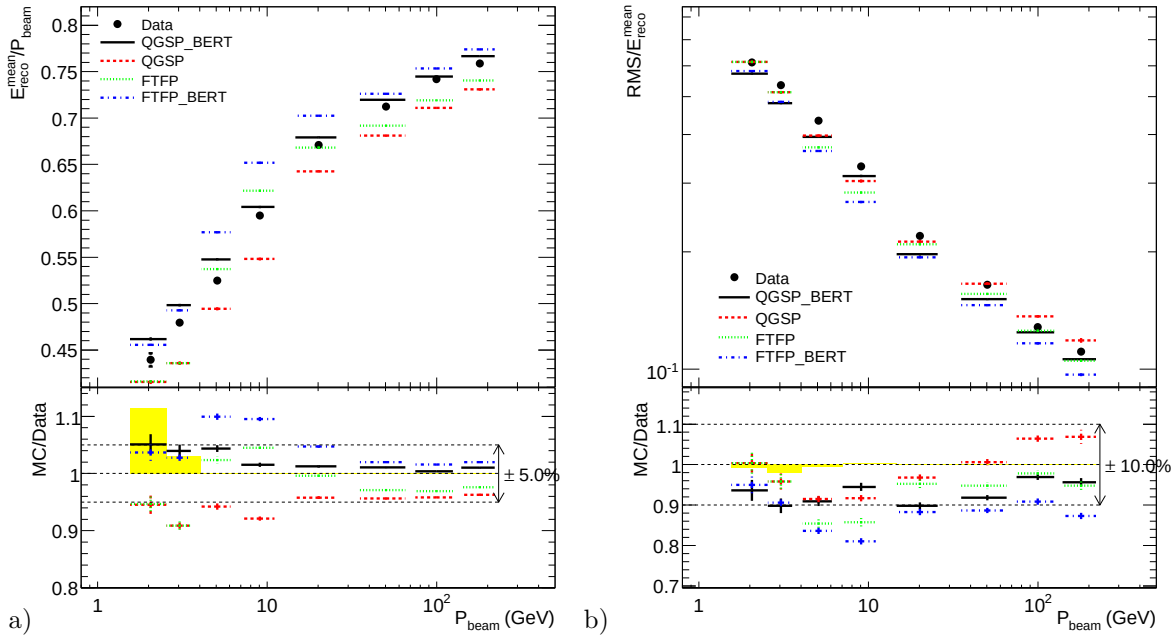

Figure 14: Mean energy (a) and resolution (b) for pions at beam momenta from 2 – 180 GeV. Shown are data as closed points and Monte Carlo simulations as lines. Only statistical uncertainties are shown. The light band indicates the uncertainty due to the likelihood cut to remove muons from pion decays.

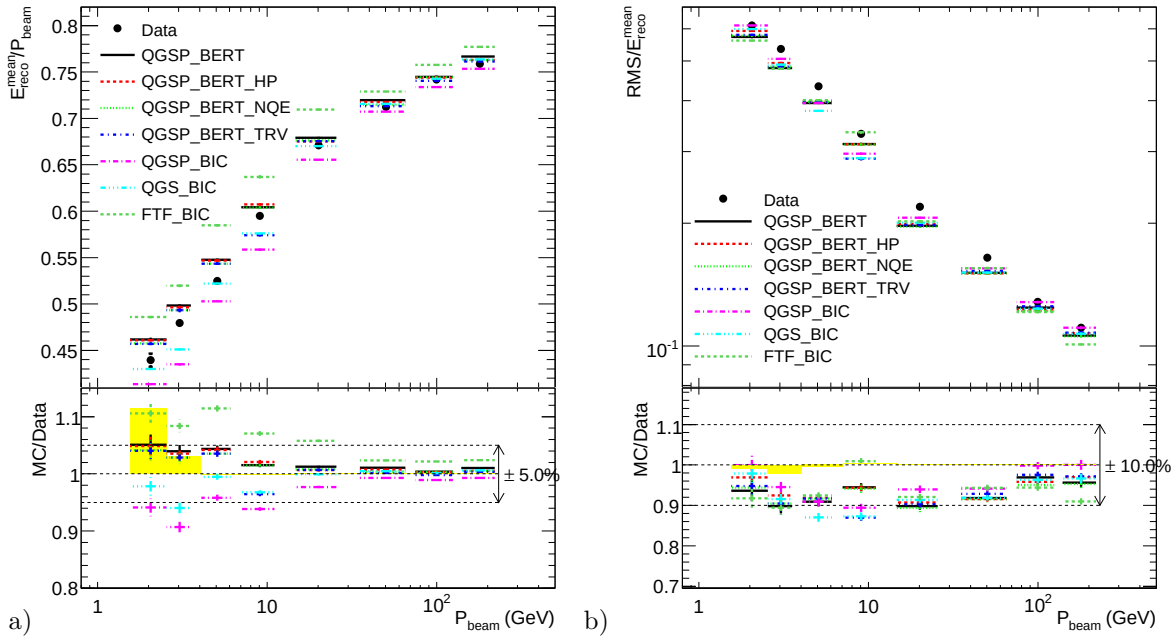

Figure 15: Mean energy (a) and resolution (b) for pions at beam momenta of 2–180 GeV. Shown are data as closed points and Monte Carlo simulations showing variants in the nuclear cascade models as lines. Only statistical uncertainties are shown. The light band indicates the uncertainty due to the likelihood cut to remove muons from pion decays.

9.1.3. Combined Resolution

The pion resolution quoted as the RMS divided by the mean energy is shown in Fig. 14b) and Fig. 15b). It ranges from about 60% at low momenta to about 10% at high energy.

The Monte Carlo simulation predicts in general a better resolution than the one measured in the data. The resolution in the simulation is better than about 10% in the VLE range and about 5% at higher momenta. At high momenta adding the cascade models to the QGSP or FTFP models makes the resolution narrower which is in worse agreement with the data.

However, the QGSP model gives a too broad resolution (by 5 – 10%) for pion momenta of 100 and 180 GeV. The QGSP_BERT model predicts a resolution that is lower by 5 – 10% than in the data for all pion momenta. The variants of the nuclear cascade models have only little influence on the resolution (see Fig. 15b). The FTF_BIC model is in a better agreement with the data than the FTFP_BERT model.

9.1.4. Energy Distribution in the LAr Calorimeter

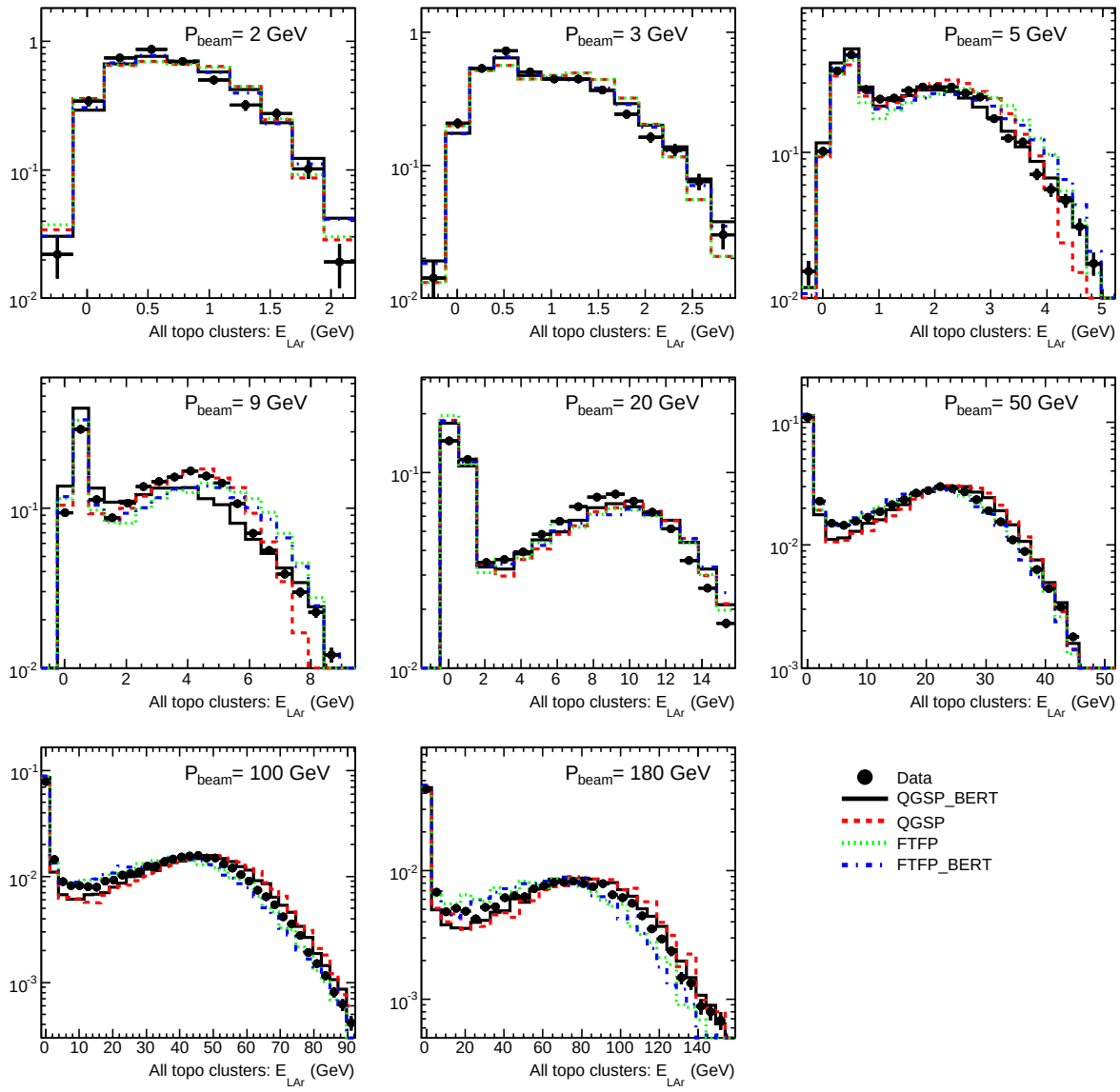

Figure 16: Energy distribution in the LAr calorimeter for pions with beam momenta of 2 to 180 GeV. Shown are data as closed points and Monte Carlo simulations as lines. Only statistical uncertainties are shown.

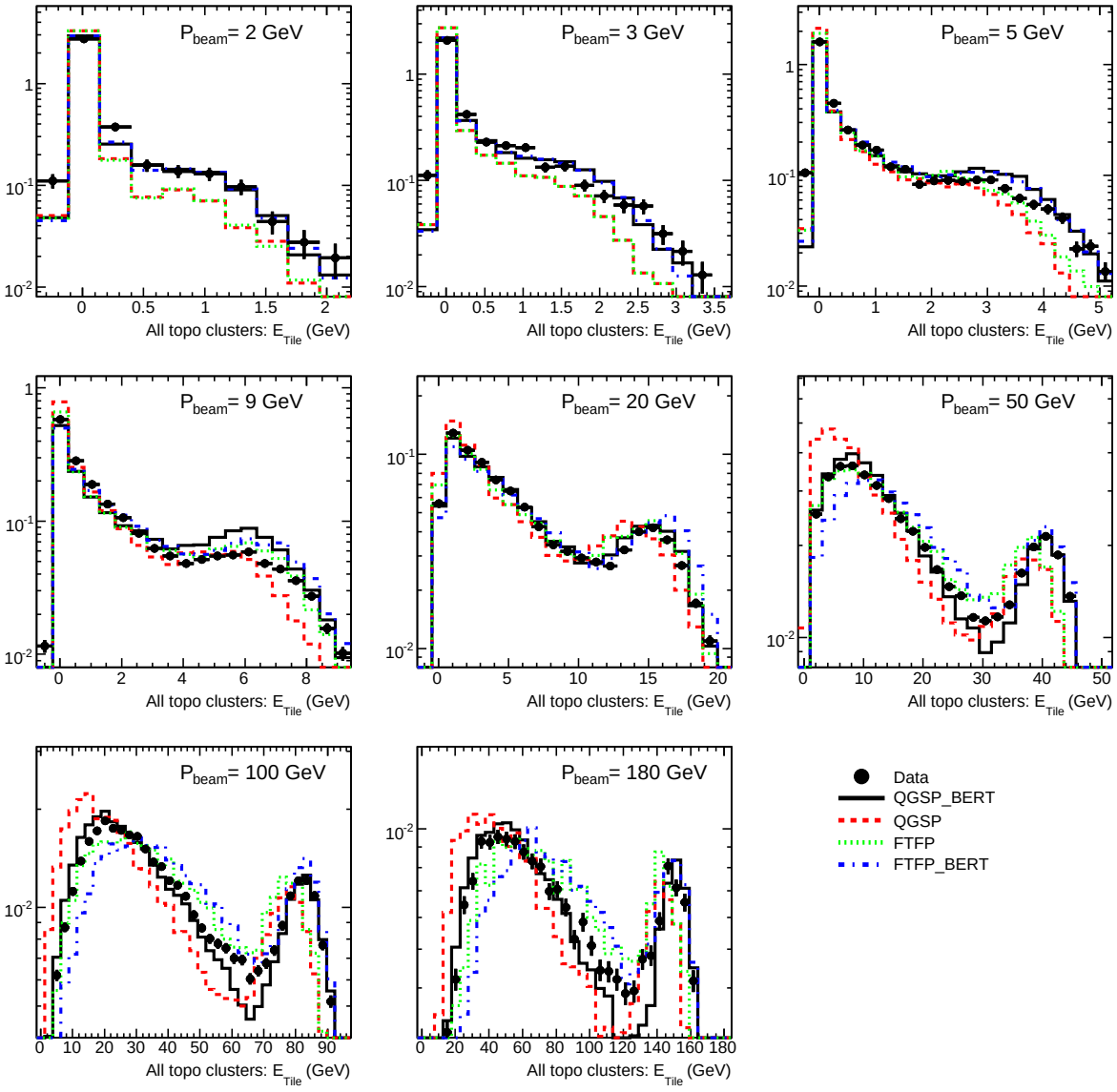

Figure 17: Energy distribution in the TileCal for pions with beam momenta of 2 to 180 GeV. Shown are data as closed points and Monte Carlo simulations as lines. Only statistical uncertainties are shown.

The energy distributions in the LAr calorimeter only are shown in Fig. 16. Data are shown as closed circles, Monte Carlo simulations are overlayed as lines. At pion momenta of 2 and 3 GeV the distribution peaks around 0.5 GeV roughly corresponding to the energy deposited by a minimally ionising particle, along with a tail towards higher energy depositions, corresponding to pions interacting hadronically in the LAr calorimeter. For pions at higher momenta this tail develops to a distribution with an approximate Gaussian shape peaking roughly at 40% of the total pion momentum and at the same time the number of events with little energy deposits increases. For high pion momenta the Monte Carlo simulation based on the QGSP model deposits too much energy in the LAr calorimeter, i.e. the shower starts earlier than in the data. For low pion momenta the Fritiof model gives a better description of the large energy deposits in the LAr . Only at 9 GeV QGSP using the Bertini intra–nuclear cascade produce too many events where the pions pass as minimally ionising particles through the LAr calorimeter and not large enough energy depositions are produced. The Fritiof model is in better agreement and reproduces bast the large energy depositions. Without the Bertini cascade the description of the total energy distribution in the LAr is better.

9.1.5. Energy Distribution in the Tile Calorimeter

Fig. 17 shows the energy distribution in the TileCal, which is anti–correlated to the energy distribution in the LAr. For low pion momenta the energy deposition in the TileCal are for most events rather small, i.e. around the expected noise value. With increasing momentum more and more pions deposit most of their energy in the TileCal. At high energy there is a double peak structure caused by events that start to shower already in LAr as opposed to events that pass as minimally ionising particles through the LAr calorimeter and deposit almost all their energy in the TileCal.

This behaviour is approximately modelled by the Monte Carlo simulations, but none of the models gives a good description of the data. QGSP predicts energy distributions that are shifted towards lower momenta and the amount of energy deposited in the TileCal for the events where the pion deposited most of its energy in the TileCal is too low. The shower starts and ends too early. Adding the Bertini cascade makes the showers longer and the data are better described, but the dip between the narrow high energy peak and the wide low energy peak is in particular not well described. In particular QGSP_BERT gives a good description of the data.

A similar trend is observed for the FTFP model. This is, however, less pronounced since the FTFP model produces longer showers than the QGSP model. The FTFP_BERT model describes well the peak and the dip, but predicts a distribution that is shifted to large values for the pions that start to shower in the LAr . The energy distribution of the events that deposit most of their energy in the TileCal is rather well described. This is in agreement with the results obtained in the 2002 test–beam where only the TileCal was exposed to a beam [15, 53].

9.1.6. Mean Energy Fraction in the Electromagnetic Calorimeter

The mean fraction of the energy deposited in the LAr calorimeter with respect to the total deposited energy is shown in Fig. 18a). As the pion momentum increases relatively less energy is deposited in the electromagnetic calorimeter. At 2 GeV the electromagnetic fraction is about 80% while at 180 GeV it is about 40%. For pions with a momentum of 2 GeV all models predict a higher energy fraction in the LAr calorimeter than measured in the data. The best data description is obtained with QGSP_BERT and FTFP_BERT. For 5–9 GeV pions the prediction from QGSP_BERT is a bit below the data, while FTFP_BERT describes the data better. For pions with momenta higher than 9 GeV QGSP_BERT is above the data, while FTFP_BERT is below. The shower predicted by the QGSP_BERT physics list is too short while the one predicted by FTFP_BERT is too long.

For the Fritiof model without the Bertini cascade more energy then in the data is deposited in the LAr calorimeter in contrast to what is found for the QGSP model. Changing the limit of applicability for the Bertini cascade (QGSP_BERT_TRV) improves the description of the point at 9 GeV, but has little influence for the other pion momenta. The FTFP model is also too high at low pion momenta, but gives a good description at high momenta.

The QGSP model together with the binary cascade (QGSP_BIC) gives a similar description of the data at high pion momenta, but a worse description for low pion momenta. As in the QGSP model the energy in the LAr calorimeter is too high. The Fritiof model with the binary cascade (FTF_BIC) gives

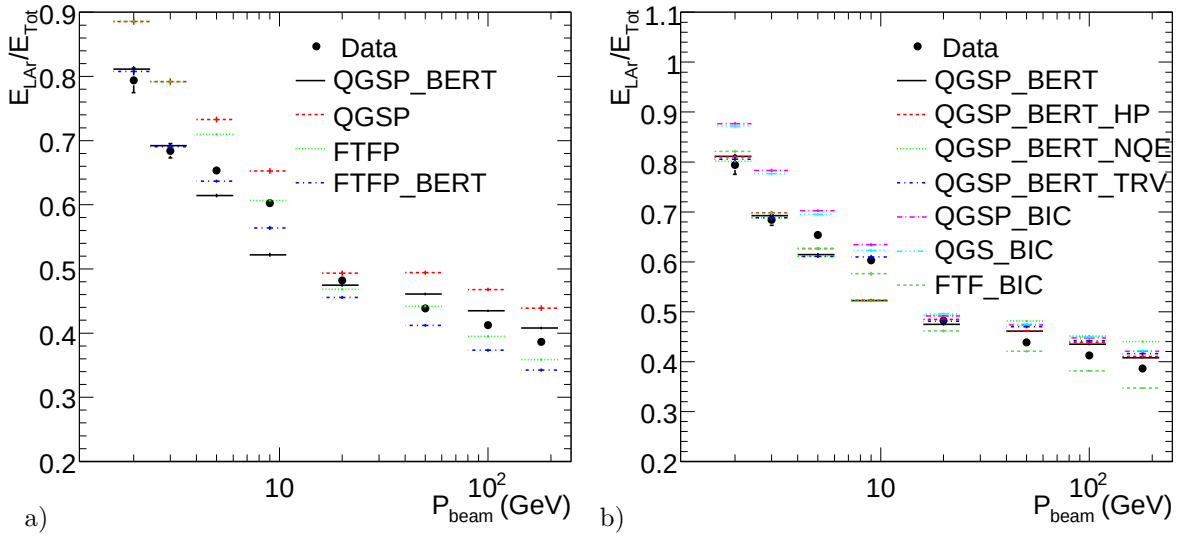

Figure 18: Mean energy fraction measured in the electromagnetic calorimeter with respect to the total energy as a function of the beam momentum for pions from 2 to 180 GeV. Shown are data as closed points and Monte Carlo simulations as lines. Only statistical uncertainties are shown. The light band indicates the uncertainty due to the likelihood cut to remove muons from pion decays.

a good description of the data up to 50 GeVand it is this model that leads to the best description of the data. For very high momentum it falls below the data.

9.2. Tile Calorimeter Response Requiring Minimally Ionising Particles in LAr

To study the response of the TileCal to pions it is interesting to select events where pions deposit only little energy in the LAr calorimeter. This allows for comparisons to previous test–beam measurements where the TileCal alone was exposed to a beam. Furthermore, these data can be useful for understanding the in–situ calorimeter calibration in ATLAS using isolated tracks from minimum bias events[55][41], where the neutral pions that are produced together with the charged pions in a jet lead to purely electromagnetic energy deposits and are absorbed in the LAr calorimeter.

Pions passing as minimally ionising particles through the LAr calorimeter deposit only little energy. To select such events the energy reconstruction method for muons is followed[15, 50]: the cell with the highest energy in a small cone of $R = 0.1$ around the nominal beam impact point is selected and its energy is added to the energy of the cell's nearest neighbour in the ϕ–direction with the highest energy. The sum of the energies of these two cells is called E_{mip} in the following.

A minimally ionising pion is then defined by requiring $E_{\mathrm{mip}} < 300$ MeV in the first and the second calorimeter compartment and $E_{\mathrm{mip}} < 100$ MeV in the third compartment.

9.2.1. Energy Distribution in TileCal

Fig. 19 shows the energy distribution in the TileCal for such events. As in the case of the inclusive sample (see Fig. 13) for low pion momenta $P_{\mathrm{beam}} \leq 5$ GeV there is still a large fraction of events where pions loose very little or no energy in the TileCal. These are therefore pions that deposit little energy in both calorimeters. The number of events depositing nearly no energy in TileCal decreases towards high pion momenta. For pion momenta with $P_{\mathrm{beam}} = 9$ GeV the peak around the noise value almost disappears and for $P_{\mathrm{beam}} > 9$ GeV an approximately Gaussian distribution with a peak around 70–80% of the pion momentum is measured.

[41] In such analyses the aim is to calibrate the hadronic response using momentum measurements from the tracking detector. Therefore, events where the charged pion is accompanied with neutral pions have to be suppressed or very restrictive cuts have to be applied such that only little energy is deposited in the LAr calorimeter.

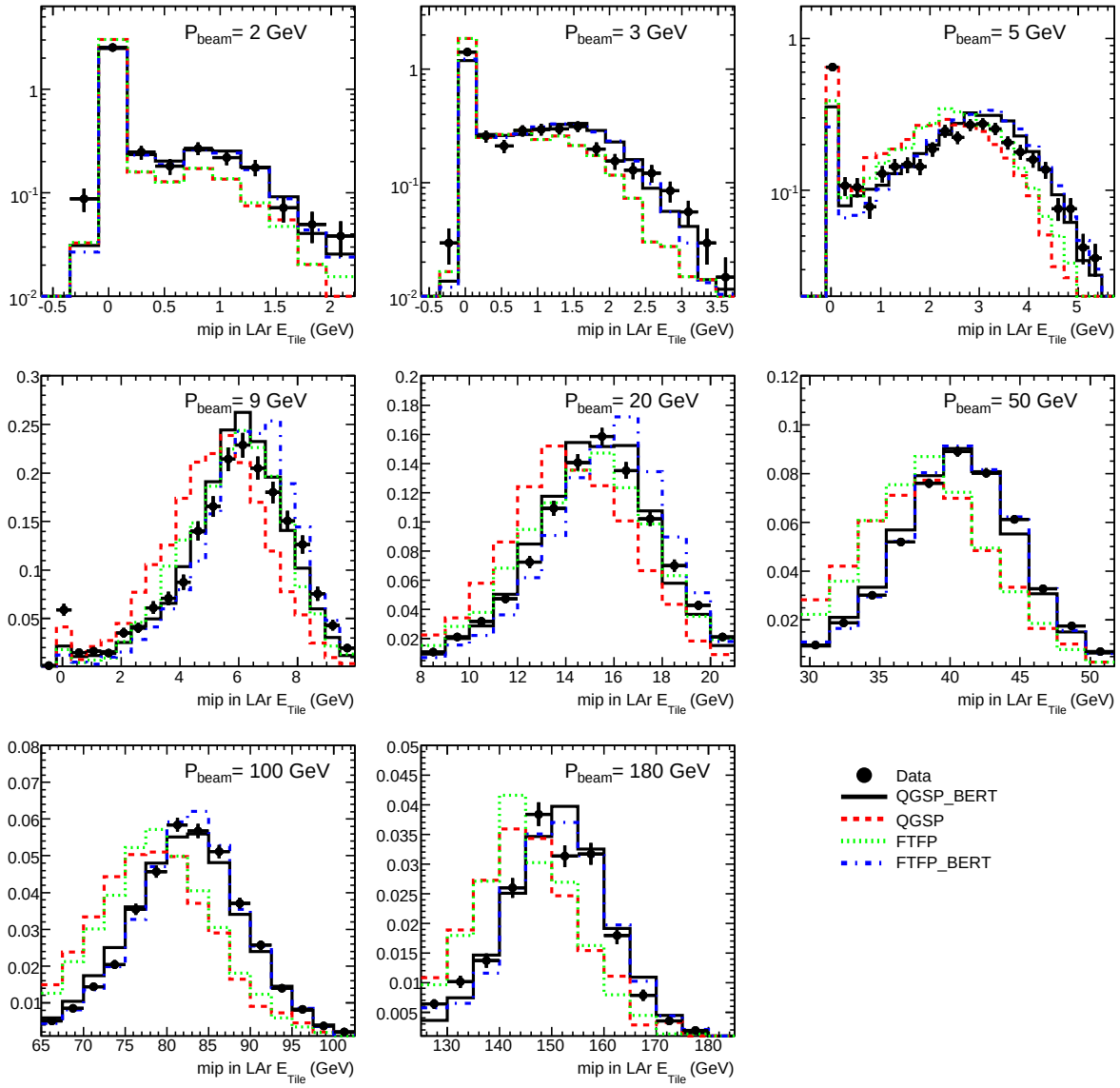

Figure 19: Total energy distribution in the TileCal for pions with beam momenta of 2–180 GeV for events where the pion passes as minimally ionising particle through the LAr calorimeter are selected. Shown are data as closed points and Monte Carlo simulations as lines. Only statistical uncertainties are shown.

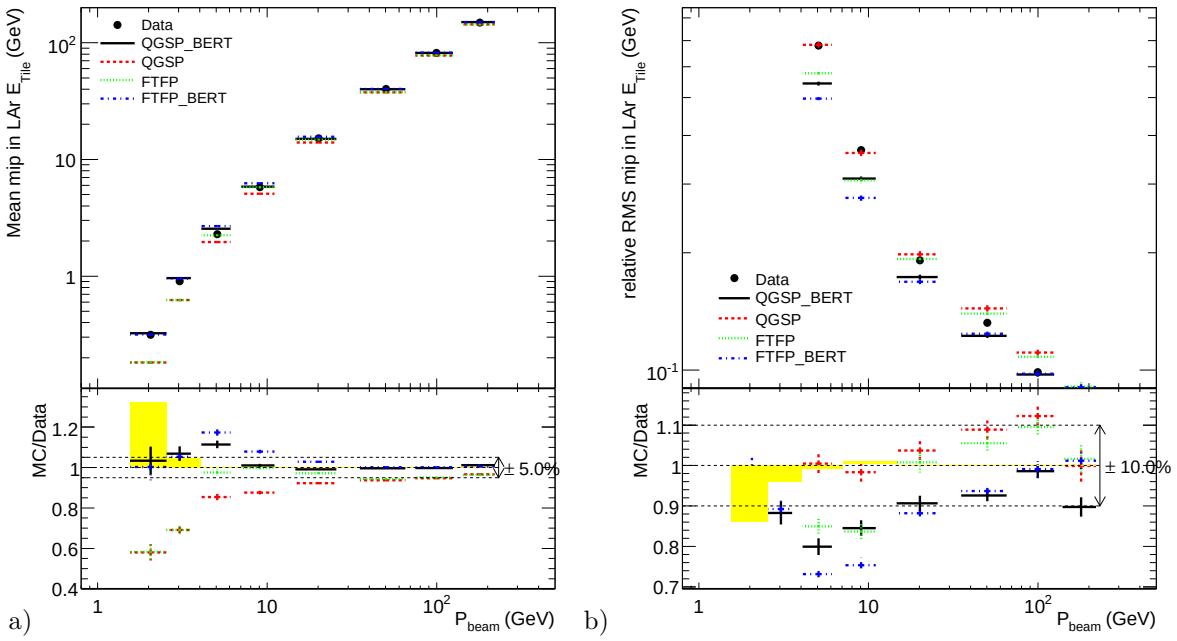

Figure 20: Mean energy for pions passing as minimally ionising particles through the LAr calorimeter with beam momenta from 2 to 180 GeV. Shown are data as closed points and Monte Carlo simulations as lines. Only statistical uncertainties are shown. The light band indicates the uncertainty due to the likelihood cut to remove muons from pion decays.

The Monte Carlo simulations are able to describe the data distribution. The best description is obtained by the models using the Bertini cascade. The QGSP and the FTFP model predict an energy distribution that is shifted towards smaller values.

9.2.2. Response in TileCal

Fig. 20 shows the mean pion energy (a) and the energy resolution (b) for pions passing as minimally ionising particles through the LAr calorimeter as a function of the beam momentum. Fig. 21a) shows a comparison of the results for the inclusive sample where the energy is measured with the LAr and the TileCal and the sample where the pions showers mainly in TileCal. The mean response and the resolution as a function of the beam momentum together with the uncertainty on the energy measurement are summarised in Table 19.

The Monte Carlo models describe the pion response measured in the data within a few per cent for pion momenta larger than 9 GeV. The QGSP and the FTFP models are below the data by about 5%. However, the Monte Carlo models have problems to describe the data for low pion momenta. QGSP and FTFP are lower by 40% at 2 GeV, but the agreement with data gets better towards higher momenta (−8% at 20 GeV). For 5 and 9 GeV FTFP describes the data within 3%.

Adding the Bertini cascade increases the response for both the QGSP and the FTFP model. For high pion momenta the increase is a few per cent, while at low pion momenta the signal increases by up to 20%. For 2 and 3 GeV this is in better agreement with the data (5–10% for QGSP_BERT and 5–15% for FTFP_BERT). As in the case of all pions the Fritiof model predicts a pion response for pion momenta of 5 GeV and 9 GeV that is too high. At low pion momenta the description by QGSP_BERT is slightly worse than in the combined case where the energy is measured in both calorimeters. The mean response is about 5–10% too high. For high momenta pions the response is well described.

9.2.3. Resolution in TileCal

The pion resolution follows a similar trend than the response: for low pion momenta the resolution for the pion that shower only in TileCal is much worse than in the case of the combined response, while for high pion momenta the resolution is better (see Fig. 21b). This behaviour can be explained by the different influence of the losses in the dead material and the LAr calorimeter. In particular, the bad

resolution at low pion momentum is due to the large losses in front of TileCal. The better resolution at large pion momenta is due to the reduced dead material losses when the pion shower mainly in TileCal and to the good TileCal energy resolution. Moreover, the longitudinal shower fluctuations are reduced when only one calorimeter is involved, since the hadronic compensation is different in the LAr and TileCal.

The resolution is described within 5–10% for high pion momenta above 10 GeV. Both the QGSP and the FTFP models predict a resolution wider than the one in the data. Adding the Bertini cascade make the resolution narrower than the one in the data (5–10%).

For low pion momenta the resolution is badly described and the Monte Carlo models make very different predictions: QGSP_BERT and FTFP_BERT are by 20–30% below the data for 3–9 GeV, but agree for 2 GeV. QGSP gives a resolution close to the data for 5 and 9 GeV, but is 20% (40%) too high for 3 (2) GeV. However, given the complex shape of the energy distribution for low pion momentum the interpretation of these results is difficult.

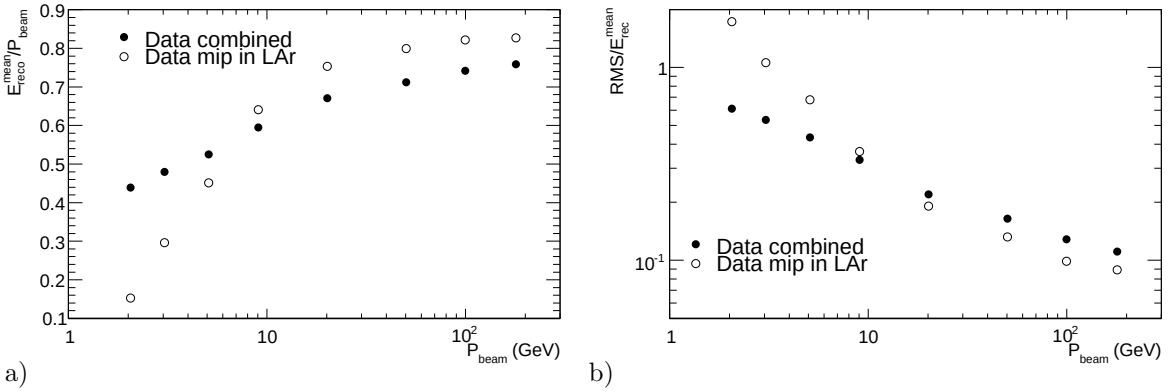

Figure 21: Comparison of the mean energy (a) and of the relative resolution (b) obtained from the combined the energy measurement in LAr and TileCal (closed circle) and the TileCal alone (open circles) for pions passing as minimally ionising particles through the LAr calorimeter as a function of the beam momentum.

10. Comparison to Earlier Results on Response and Resolution

10.1. Earlier CTB Results at Low Pion Momenta

The results obtained in this analysis can be compared to the ones from ref. [1], where a different data–set of the CTB has been studied. The experimental set–up of the earlier run period used in ref. [1] was the same as in this analysis, but in the inner detector system only the TRT was operational. Moreover, the beam steering was different leading to a much larger muon contamination of the pion beam. Therefore the available event statistics was much lower. In this earlier run period a full scan of beam impact points and more beam momenta were available. Here, we compare to the results obtained at $\eta_{\rm nom} = 0.45$.

There are three main differences between this and the earlier analysis:

- The energy is reconstructed by summing all cell energies in a small cone around the beam impact point. This method is well suited for a test-beam analysis. This energy reconstruction method gives similar results (within about 1%) as the sum over all topological clusters [22]. For the data comparison the results of this analysis are also measured using the sum of all cells in a cone.

- The results quoted in ref. [1] refer to the peak of the distribution obtained by fitting a Gaussian distribution around the mean. An iteration is used to well centre the Gaussian distribution. The fit is performed within two standard deviations. For the data comparison the results of this analysis will also be done using the peak instead of the mean.

- To remove muons contaminating the pion beam, in ref. [1] the energy in the last TileCal compartment is required to be compatible with noise ($E_6 < 0.16$ GeV). This biases the mean energy by up to 5% [1]. For the data comparison the results of this analysis will be compared with and without the cut on the last TileCal compartment.

Fig. 22a) shows a comparison of the data and the Monte Carlo simulation based on the QGSP_BERT physics list presented in this analysis and the data from ref. [1]. The two data sets clearly show a different dependence on the beam momentum. The agreement between the two data sets improves as the beam energy increases going from 3% at 3 GeV to 1% at 9 GeV. The difference between the two data sets is probably due to the different strategy used to cut the muon contamination. However, the available statistics does not allow to draw definite conclusions.

Fig. 22b) illustrates the influence of the requirement on the last TileCal compartment on the pion energy. With this requirement the pion response is about 3% lower at 9 GeV and 4% lower at 3 GeV. This behaviour is well reproduced in the Monte Carlo simulation. Also shown is the ratio between the data of ref. [1] and the data in this analysis without a requirement on the last TileCal compartment. This comparison demonstrates that the response difference of the data in ref. [1] and the data in this analysis can be partly explained with the different selection criteria.

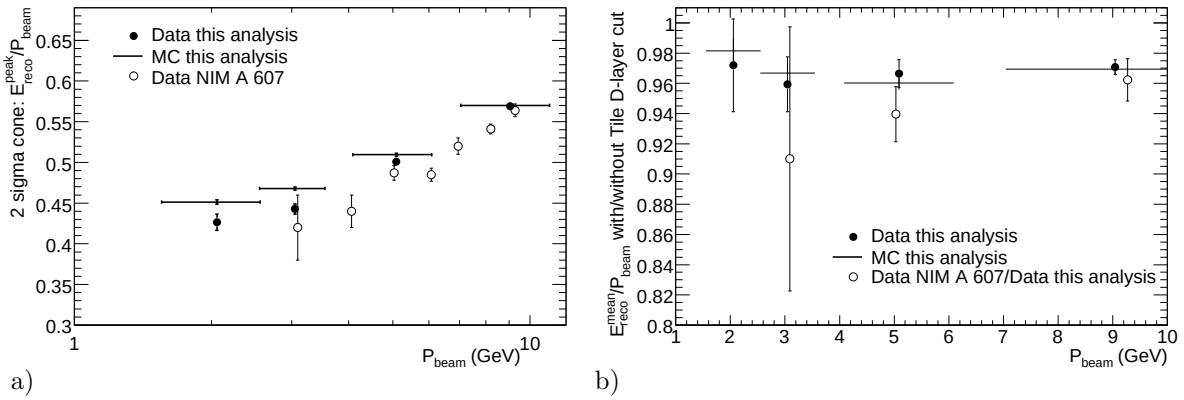

Figure 22: a) Pion response as a function of the beam momentum for the CTB data from ref. [1] and data as well as Monte Carlo simulations obtained in this analysis. For the purpose of comparison the response refers to the peak of the distribution, the energy is reconstructed using the sum of all cells above a noise threshold of two standard deviations and a cut on the last TileCal compartment is applied. b) Pion response ratio with and without a cut on the last TileCal compartment for data (closed circles) and Monte Carlo simulation (lines) for the data presented in this analysis. Added is the ratio of the data from ref. [1] and data in this analysis without a cut on the last TileCal compartment.

10.2. Earlier CTB Results at High Pion Momenta

Results from the same data-sets for beam momenta at 20, 50, 100 and 180 GeV can also be found in ref. [56], where the quoted response refers to the peak value. These results are in very good agreement with this analysis, when comparing peak reponse values.

Results at high beam momenta have also been published in ref. [57]. The data have been taken in an earlier CTB data taking period where the inner detector was not yet fully installed. These data refer to the peak of the pion response in the calorimeter, i.e. they have been corrected for energy losses in the dead material before the calorimeter (about 1%) and for proton contamination at 20, 50 and 100 GeV[42]. The data in this analysis and the one presented in ref. [57] are in reasonable agreement. The largest deviations of about 3% are seen at 20 GeV and at 180 GeV.

At 20 GeV the difference can be explained by the different energy reconstruction methods. In ref. [57] all calorimeter cell above 2σ of the noise are added up, while in this analysis topological clusters are used. The pion response reconstructed with topological clusters is about 4% higher than the one reconstructed with a cone and applying a noise suppression on the cell level [22].

The difference at 180 GeV can be explained by response differences between of a pure pion beam as available in ref. [57] and the hadron beam with a large proton contamination as presented in this analysis [58].

[42] At 180 GeV a negative pion beam without proton contamination was available.

P_{beam} (GeV)	20	50	100	180
Peak				
CTB04 data	0.762	0.809	0.830	0.834
TB02 data	0.825	0.849	0.858	0.861
proton correction	1.002	1.014	1.018	1.019
dead material correction	1.085	1.036	1.020	1.012
Sigma				
CTB04 data	0.169	0.109	0.080	0.070
TB02 data	0.137	0.100	0.077	0.069
proton correction	1.002	1.019	1.039	1.063
dead material correction	0.800	0.900	0.950	0.980

Table 13: Data from the CTB04 where the pion trasverses the LAr calorimeter as minimally ionising particle and the TB02 together with the correction factors for proton contamination and for energy losses in the dead material to be applied to the CTB04 data.

10.3. Earlier Test-beam Results with TileCal Only

The data where the pion traverses the LAr calorimeter as minimally ionising particle can be compared to data of an earlier test–beam where only the TileCal has been exposed to a pion beam [15]. These data have been taken in 2002 (TB02) and only data above 20 GeV are available.

Also for these data the response and resolution refers to the peak and the width of a Gaussian distribution and, for the purpose of comparison, the same definition was adapted (see Table 13).

In the TB02 data a Cherenkov counter has been used to identify pions. The CTB data therefore have to be corrected for proton contamination. The correction factors from ref. [58] are used. They are based on the results in [52, 53]. The CTB data need also to be corrected for energy losses in front of the calorimeter, in the LAr calorimeter and in the material between the LAr and the Tile calorimeter. This correction is calculated using a Monte Carlo simulation for events that traverse the LAr calorimeter as minimally ionising particles. The correction factor are given in Table 13.

Fig. 23a) and Fig. 23b) shows the comparison of the TB02 and the CTB data. After correction for proton contamination and dead material energy losses are applied, the data agree well.

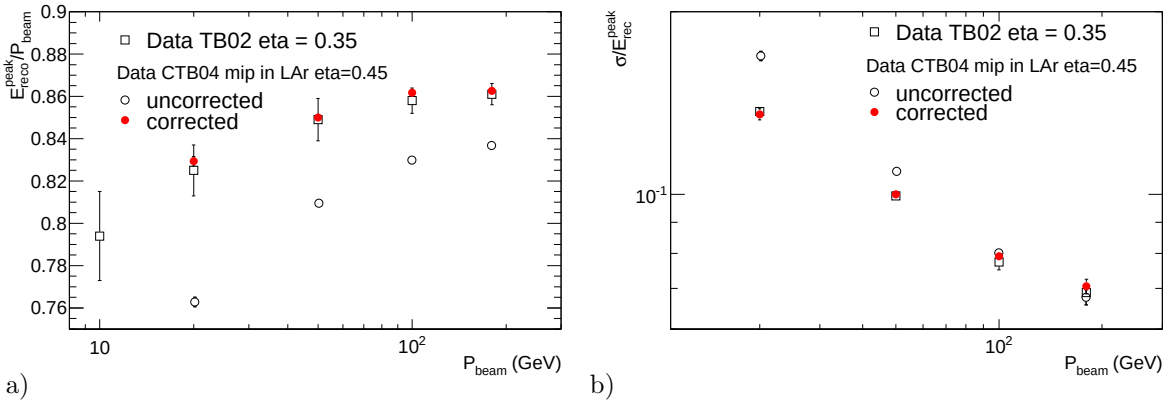

Figure 23: a) Pion response (a) and resolution (b) as a function of the beam momentum for data where only the TileCal has been exposed to pion beams [15] (closed circles). Also shown are CTB data for events where the pions traverse the LAr calorimeter as minimally ionising particle (open circles). The red circles show the CTB data after applying correction for dead material and proton contamination.

11. Longitudinal Shower Profiles

The fine longitudinal segmentation of the ATLAS barrel calorimeter in seven compartments can be used to study the longitudinal shower development.

11.1. Definition

The mean energy deposited in each calorimeter compartment is divided by the compartment width and by the total pion energy and measured as a function of the distance the shower has traversed in the calorimeter. The compartment width is expressed in units of nuclear interaction lengths and is measured at the middle of each compartment. It refers to the impact point at $\eta = 0.45$. The quoted length includes the material in front of the calorimeter and the material between the calorimeters (see Table 2).

11.2. Comparisons of Data and Monte Carlo Simulations

Fig. 24 shows the longitudinal pion shower profile for low pion momenta from 2 to 9 GeV and Fig. 25 for high pion momenta of 20 to 180 GeV. The hadronic shower quickly rises and reaches a maximum around about 1 λ and then exponentially falls off towards the end of the calorimeter. In the last compartment of the TileCal, i.e. after about 8 λ, most of the pion energy is deposited and the shower ends. At low pion momenta the shower rises more quickly than at high pion momenta. The shower penetrates deeper into the calorimeter towards high pion momenta.

At high pion momenta ($P_{\mathrm{beam}} > 10$ GeV) (see Fig. 25) the QGSP model predicts a mean energy that is in the second Tile calorimeter compartment 20% lower than the one measured in the data. With the Bertini cascade the data are better described, but the shower is still shorter than the one in the data (5–10%). It is interesting that the shower is significantly shorter when the quasi-elastic scattering process is switched off.

The Fritiof fragmentation leads to a shower longer than the one produced by the QGS fragmentation. The second TileCal compartment is described within ± 2 %. By adding the Bertini intra–nuclear cascade the showers get longer. This is in worse agreement with the data.

At very low pion momenta (see Fig. 24) the start of the shower (i.e. the first 1–2 λ) is described by the models within 10%. However, at the end of the shower the QGSP as well as the FTFP models predicts a response much lower than the data (30–70%). The shower development is therefore too short. Adding the Bertini cascade gives a slightly better description of the data at 2 and 3 GeV, but a too long shower at 5 and 9 GeV (+10–20%). The Fritiof model with the binary cascade describes the data within 10–20% at 5 and 9 GeV.

In conclusion, the addition of the Bertini model makes the shower longer. This is generally in better agreement with the data, but the response towards the shower end remains too low. High pion momenta are generally better described than low pion momenta. The agreement for high pion momenta ($P_{\mathrm{beam}} > 10$ GeV) is within 10-20% for all calorimeter compartments, while for low pion momenta large discrepancies are seen.

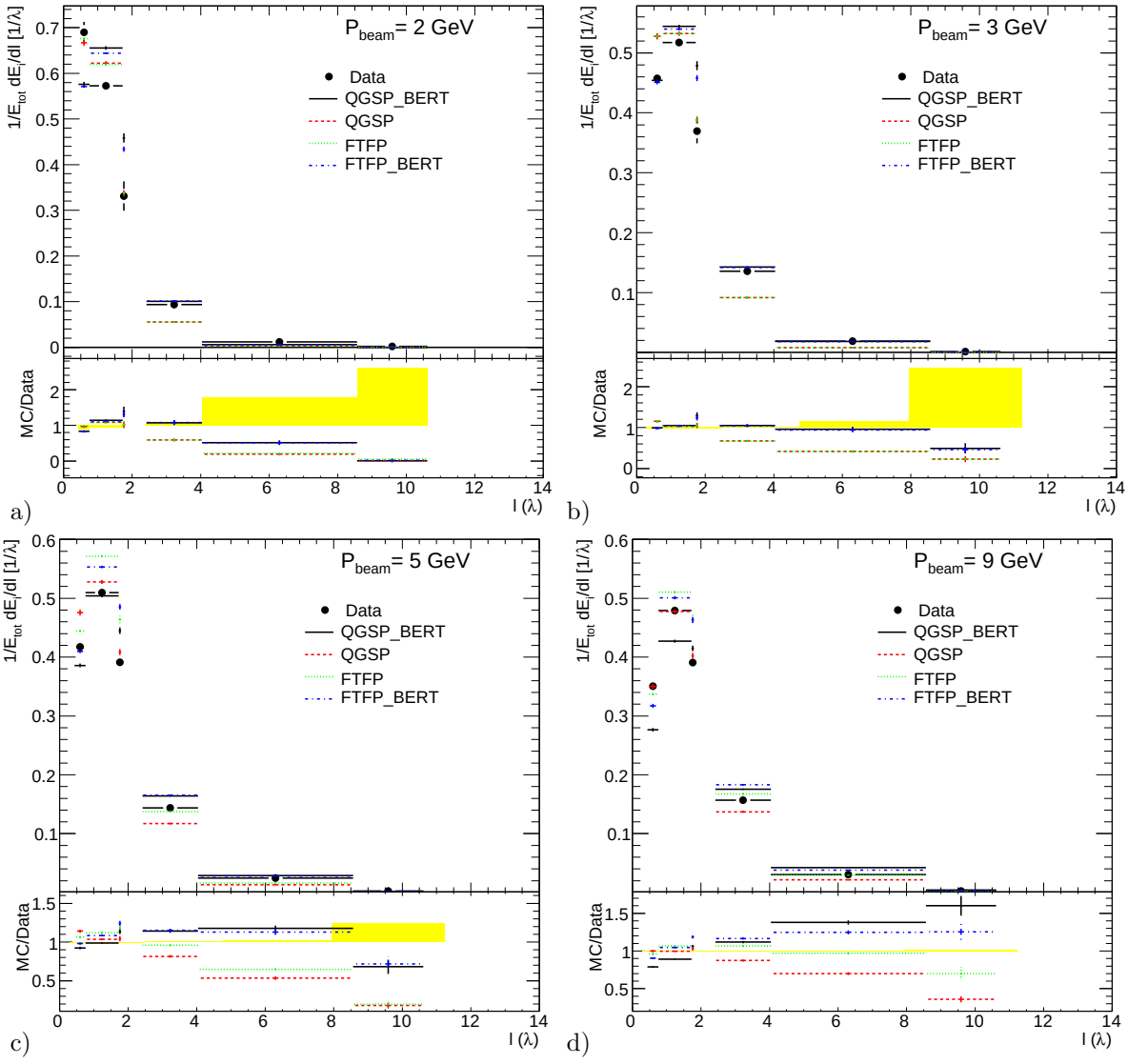

Figure 24: Relative mean energy per unit length per calorimeter compartment as a function of the material length the hadronic shower has traversed measured in nuclear interaction lengths for beam momenta of 2, 3, 5 and 9 GeV. Shown are data as closed points and Monte Carlo simulations as lines. Only statistical uncertainties are shown. The light band indicates the uncertainty due to the likelihood cut to remove muons from pion decays.

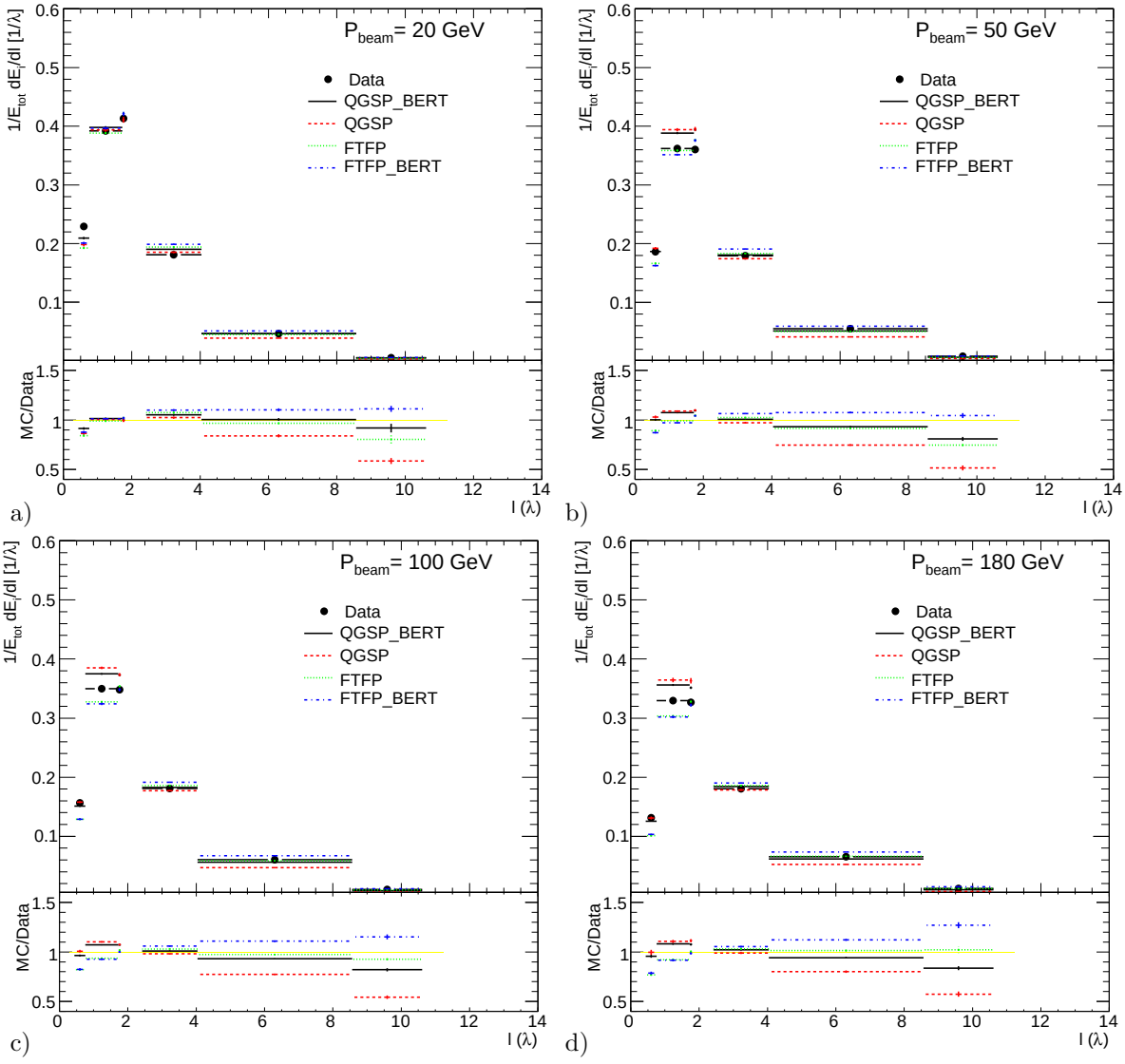

Figure 25: Relative mean energy per unit length per calorimeter compartment as a function of the material length the hadronic shower has traversed measured in nuclear interaction lengths for beam momenta of 20, 50, 100 and 180 GeV. Shown are data as closed points and Monte Carlo simulations as lines. Only statistical uncertainties are shown. The light band indicates the uncertainty due to the likelihood cut to remove muons from pion decays.

12. Transverse Shower Profile

The fine granularity of the ATLAS barrel calorimeter and, in particular, of the LAr calorimeter allows the transverse hadronic shower profile to be studied in great detail. The transverse shower development is measured using the energy flow in the η–direction, since the granularity is finer than the one in the ϕ–direction.

12.1. Mean Transverse Shower Profile per Calorimeter Compartment

12.1.1. Definition

For each event first the mean η position in each calorimeter compartment is determined:

$$\langle \eta \rangle = \frac{\Sigma_i \eta_i E_i}{\Sigma_i E_i}, \tag{10}$$

where the sum runs over all cells (in the particular calorimeter compartment) that are included in topological clusters. The variable E_i denotes the energy deposition in each compartment cell and η_i corresponds to the position of the cell centre.

The mean transverse hadronic shower profile for each calorimeter compartment is then measured as:

$$\frac{1}{E}\frac{dE}{d\eta_{\rm bin}} = \frac{1}{\Sigma_{\rm ev}\Sigma_i\ E_i}\frac{\Sigma_{\rm ev}\Sigma_i E_i\ (\eta_i - \langle\eta\rangle)}{\Delta\eta_{\rm bin}}, \tag{11}$$

where the first sum runs over all events and the second one over all cells in a given compartment and $\Delta\eta_{\rm bin}$ is the cell granularity corresponding to the bin width in the η–direction.

12.1.2. Dependence on the Shower Depth

The transverse shower profile for pions with a momentum of 5 GeV is shown in Fig. 26a) and of 100 GeV in Fig. 26b). The results from the first and second compartment in the LAr calorimeter and the first and second compartment in the TileCal are overlayed. Only data are shown. The varying granularity of the shower profiles corresponds to the varying calorimeter granularity.

At the beginning the shower is well centred around the shower axis. As the shower develops the transverse energy profile becomes wider. It is interesting that for 100 GeV pions the transverse shower profile is wider in the first than in the second compartment: this might indicate an increased back–scattering contribution.

As already observed in the case of electrons [4, 5], the transverse shower profile is wider at positive η–values with respect to the shower axis than for negative ones.

12.1.3. Dependence on the Pion Momentum

Fig. 27 shows the dependence of the transverse shower profiles on the pion momentum for the first and second compartments in the LAr and TileCal calorimeters. The shower becomes wider for decreasing pion momenta. The shower becomes narrower for increasing pion momenta. This can be partly interpreted as a kinematic effect and and as increased electromagnetic energy fraction at high pion momenta that favours energy deposits near the shower. It also indicates the decreased role of the neutrons at high energies. Only the first LAr compartment exhibits a different behaviour. There the shower is narrowest for pions with 5 GeV and widest for pions with 9 GeV, while the transverse profiles at 50 GeV and 180 GeV lie in between.

12.1.4. Comparison of Data and Monte Carlo Simulations

Fig. 28 and Fig. 29 show a comparison of the data with Monte Carlo simulations for the LAr (a,c) and TileCal (b,d) middle compartment for pions with momenta of 5 GeV (a,b) and 100 GeV (c,d). The transverse shower profile at the beginning of the shower is well described by all Monte Carlo simulation models. Only at the end of the shower the transverse shower profile in the Monte Carlo simulation is narrower than the one in the data (see Fig. 28b and d). For pions at low and at high momenta adding the Bertini intra–nuclear cascade to either the QGSP or the FTF model makes the shower wider, but not as wide as measured in the data. The Bertini and the binary cascade give comparable results.

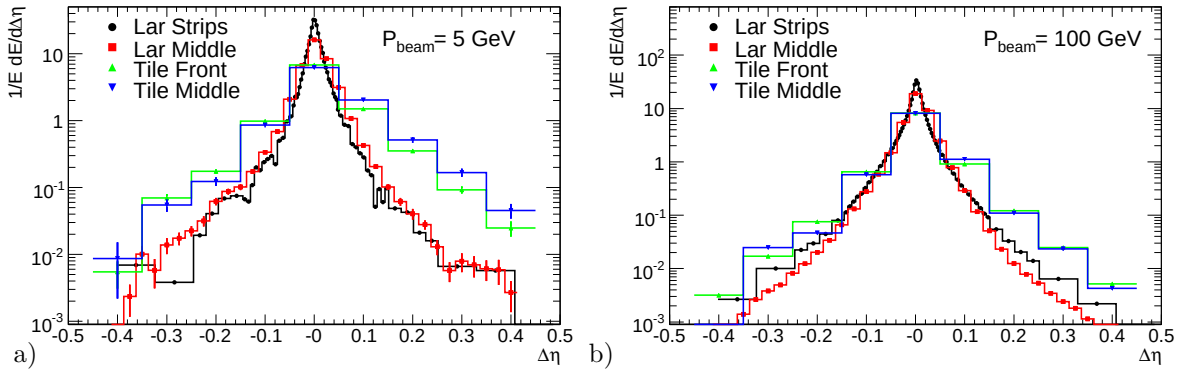

Figure 26: Mean transverse shower profile as a function of the distance of the calorimeter cells and the shower axis in the η–direction. Shown are results for various calorimeter compartments for a 5 (a) and a 100 GeV (b) pion beam. Only data and statistical uncertainties are shown. The bins are larger in the shower tails to reduce statistical fluctuations. The light band indicates the uncertainty due to the likelihood cut to remove muons from pion decays.

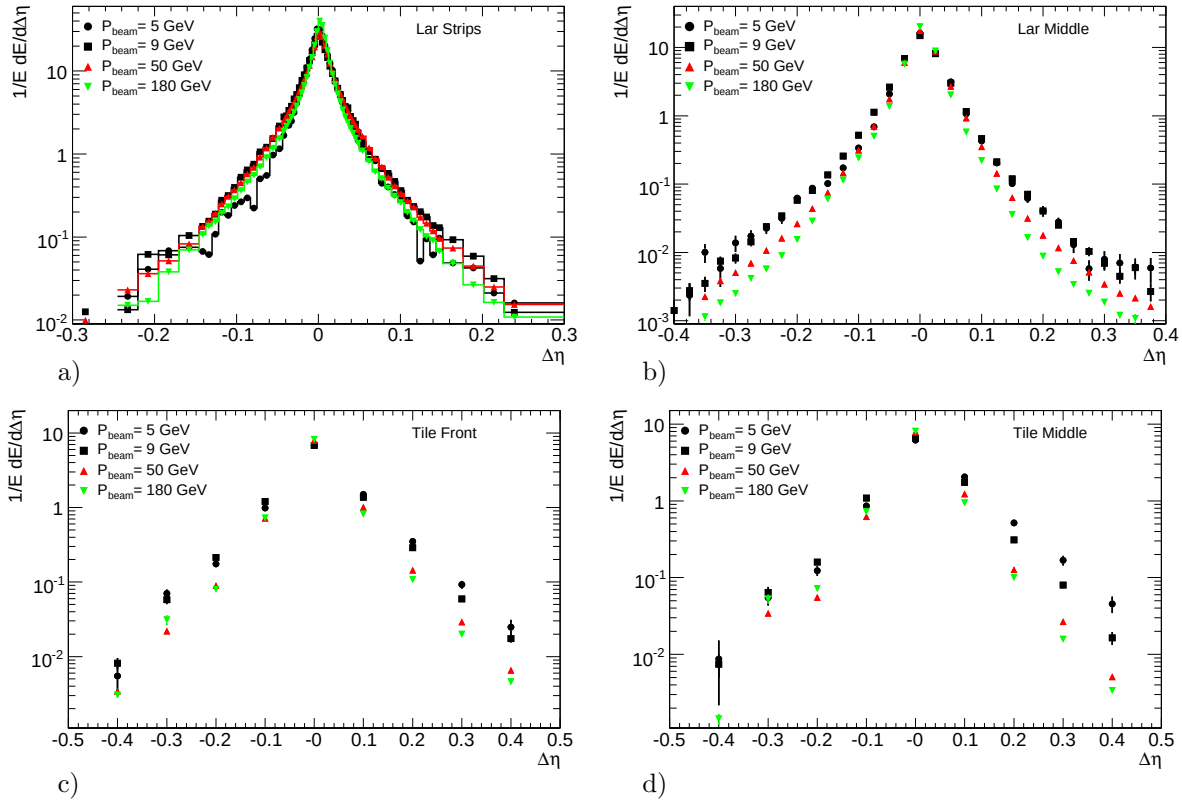

Figure 27: Mean transverse shower profile in the LAr strip (a), the LAr middle (b), the TileCal front (c) and the TileCal middle compartment (d) in the η–direction for pions with beam momenta at 5, 9, 50 and 180 GeV. Only data and statistical uncertainties are shown. The light band indicates the uncertainty due to the likelihood cut to remove muons from pion decays.

The increase of the energy deposit far from the shower axis is probably due to the increased production of neutrons when adding the Bertini cascade. It is interesting to note that the QGSP_BERT_HP and the QGSP_BIC_HP do not improve the description of the data, since they do not widen the transverse shower profile of the middle compartment in TileCal. On the contrary, in the middle compartment of the LAr calorimeter more energy is measured in the far tail of the transverse shower development. For low and high pion momenta this is not in agreement with the data (see Fig. 29 a,c). Once can deduce that the shower development in the tails far away from the shower axis is not so much influenced by neutrons at thermal energies, but rather by neutrons in the nuclear regime. The overshoot in the beginning of the showering is probably due to an increased back–scattering for which low energetic neutrons play a more important role.

In conclusion, the transverse shower profile is well described at the shower start, but at the end of the shower in the data are wider than in the Monte Carlo simulation.

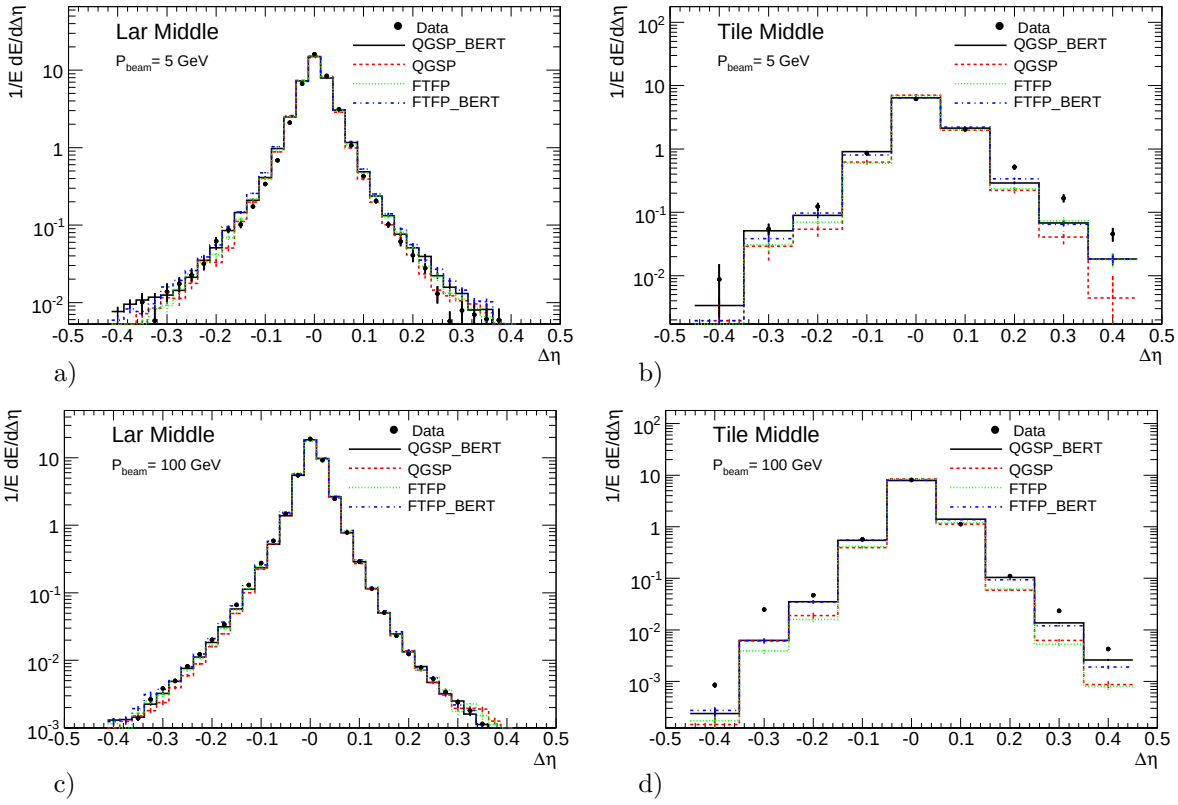

Figure 28: Mean transverse shower profile as a function of the distance of the calorimeter cells and the shower axis in the η-direction. $\Delta\eta = 0$ corresponds to the nominal beam direction. Shown are results for the LAr (a,c) and TileCal (b,d) middle compartments of a 5 (a,b) GeV and a 100 GeV (c,d) pion beam. Data are shown as closed circles, Monte Carlo simulations are overlayed as lines. Only statistical uncertainties are shown. The light band indicates the uncertainty due to the likelihood cut to remove muons from pion decays.

12.2. Energy Fraction in a Narrow Cone

The radial extension can also be studied by summing all the energy in a narrow cone around the shower axis and dividing this quantity by the total energy in a larger cone:

$$E_{\text{core}} = \Sigma_{\text{cells with d}\phi,\text{d}\eta<0.1}\ E_{\text{cell}}/\Sigma_{\text{cells with d}\phi,\text{d}\eta<0.3}\ E_{\text{cell}}, \tag{12}$$

where $d\eta = \eta_{\text{cell}} - \eta_{\text{nom}}$ ($d\phi = \phi_{\text{cell}} - \phi_{\text{nom}}$) and η_{nom} (ϕ_{nom}) is the nominal beam impact position. The small cone is defined such that in the TileCal only one cell per compartment is taken. All cells in topological clusters are used.

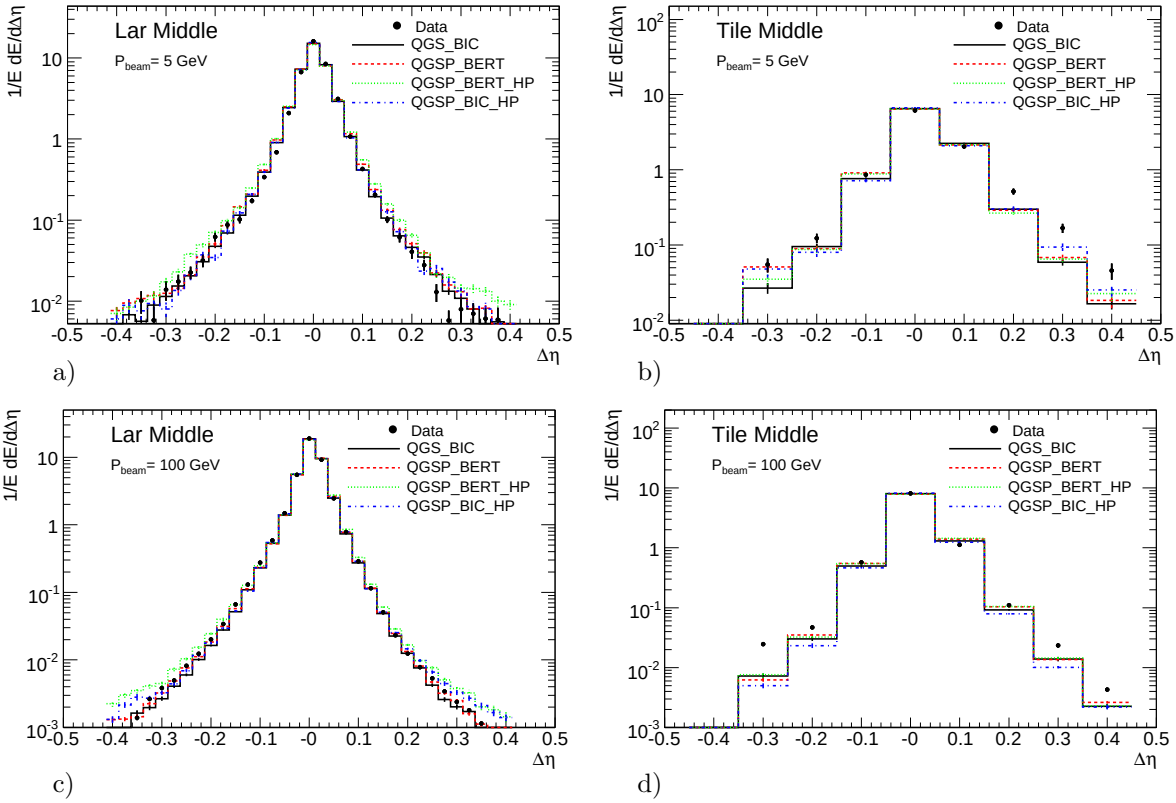

Figure 29: Mean transverse shower profile as a function of the distance of the calorimeter cells and the shower axis in the η-direction. $\Delta\eta = 0$ corresponds to the nominal beam direction. Shown are results for the LAr (a,c) and TileCal (b,d) middle compartments for a 5 (a,b) and a 100 GeV (c,d) pion beam. Data are shown as closed circles, Monte Carlo simulations are overlayed as lines. Only statistical uncertainties are shown. The light band indicates the uncertainty due to the likelihood cut to remove muons from pion decays.

The E_{core} observable is better suited to study event-by-event fluctuations than the mean radial shower profiles. Moreover, this observable depends less on the correlation of the longitudinal and transverse shower development, since the sum over the cell energies extends over all calorimeter compartments.

The distribution of E_{core} is shown in Fig. 30 for data and Monte Carlo simulations for pion momenta of 2 to 180 GeV. The shower becomes narrower towards larger pion momenta. Below 9 GeV the peak of the distribution shifts towards 1, i.e. most of the events deposit all their energy in a narrow cone. However, the fluctuations in the transverse energy deposits become larger and the number of events which deposits most of their energy out–side the narrow cone increases. A certain fraction of events deposit no energy near the shower axis ($E_{\text{core}} = 0$). The fraction of such events increases as the energy decreases. In most of these events all the energy is deposited outside the narrow cone. Their energy is uniformly distributed in η. It is likely that these events are caused by strong interactions before the calorimeter (and after the TRT) where the secondary particles produced in the inelastic collisions have been scattered under large angles.

Fig. 31 shows the mean energy fraction in the narrow cone as a function of the beam momentum. The QGSP model produces for all pion momenta showers that are too narrow. For high pion momenta the peak is shifted to higher values and for low pion momenta the large tail at low E_{core} is too small. The mean E_{core} is about 5% too high. The Fritiof model makes the same predictions for $P_{\text{beam}} < 10$ GeV, but produces showers that are a bit wider for high pion momenta (+4%).

Adding the Bertini cascade makes the shower wider for both the QGSP and the Fritiof model. The E_{core} distribution is well described by these models (within 3% for 3–9 GeVand −4% at 2 GeV). The variants of the Bertini cascade do not change the radial shower extension. The QGSP model with the binary case produces showers that are laterally too narrow. The quasi-elastic scattering has no influence on the transverse energy deposition. The mean E_{core} is 5% too high. The Fritiof model together with the binary cascade produces showers that are well described. The mean E_{core} is 3–6% lower than the one in the data for $P_{\text{beam}} < 10$ GeV, but describes the data for high pion momenta (+1%). The FTF_BIC model gives a bit narrower shower at lower momenta (−5%), but is the same at higher momenta

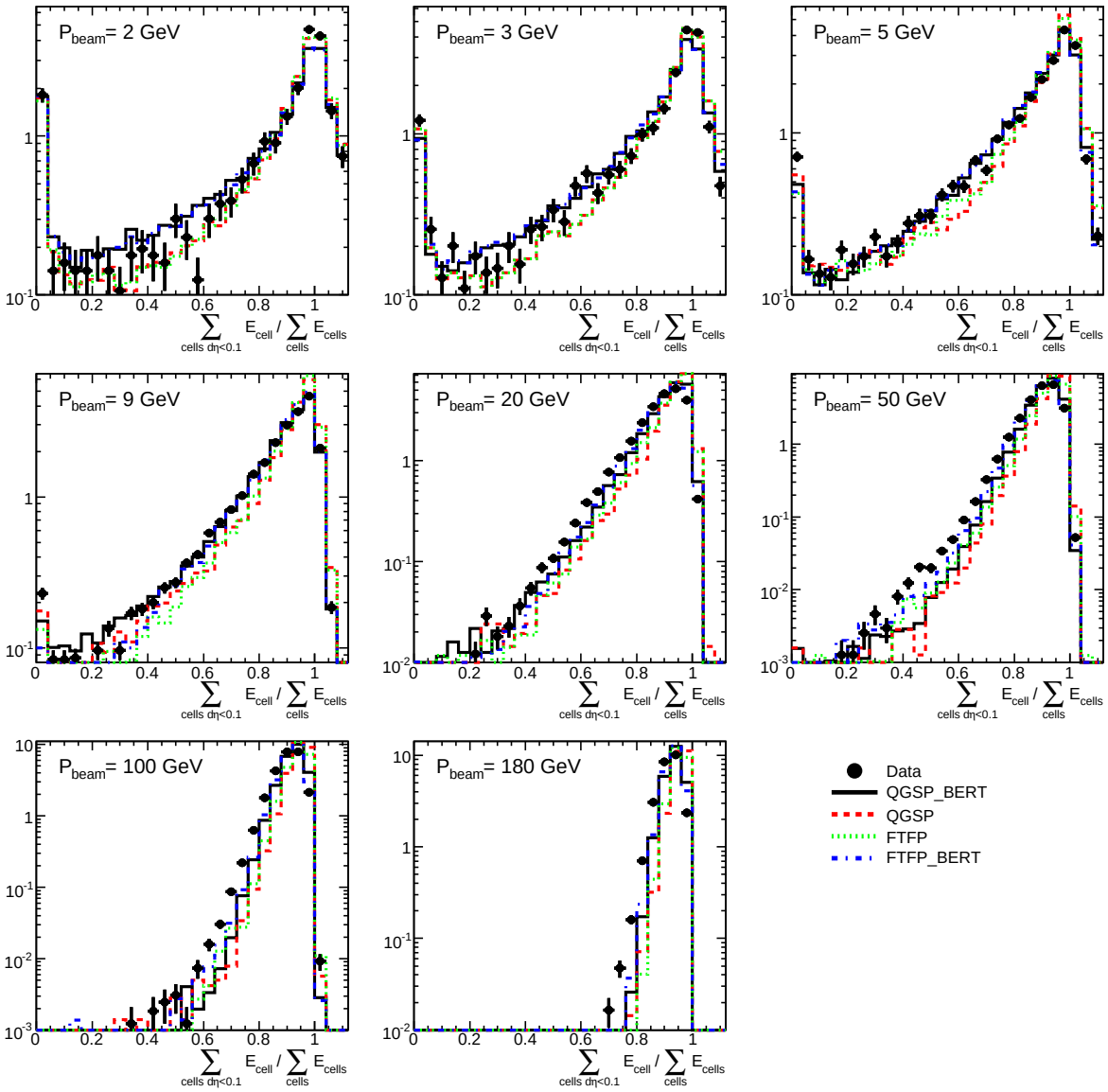

Figure 30: Distribution of the energy fraction of the shower core to the total energy (E_{core}) for pions with beam momenta from 2 to 180 GeV. Shown are data as closed points and Monte Carlo simulations as lines. Only statistical uncertainties are shown.

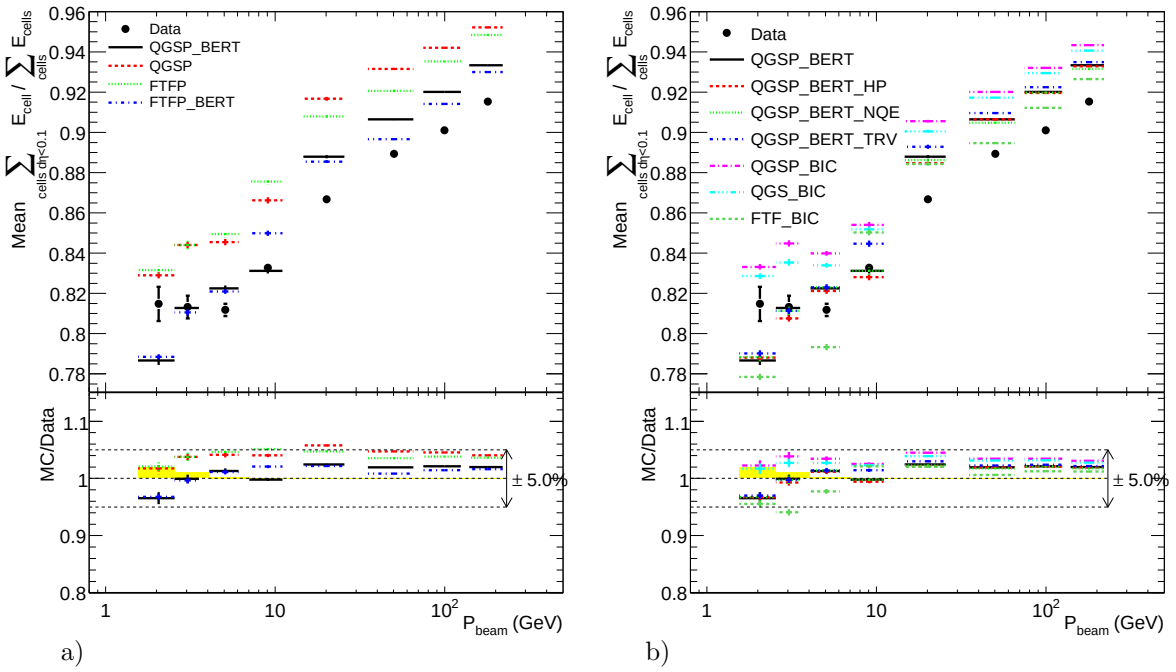

Figure 31: Mean energy fraction of the shower core to the total energy E_{core} for pions with beam momenta from 2 to 180 GeV. Shown are data as closed points and Monte Carlo simulations as lines. Only statistical uncertainties are shown. The light band indicates the uncertainty due to the likelihood cut to remove muons from pion decays.

13. Topological Cluster Moments

Thanks to the fine granularity of the ATLAS barrel calorimeter the shower topology can be well measured. It is convenient to describe the shower topology by the so–called *cluster moments*[43]. For each topological cluster the topology of the energy distribution in the cells belonging to the cluster can be characterised by one well defined property.

The cluster moments describe the transverse and longitudinal extension of the shower and the energy density. Examples are the mean shower depth along the shower axis, the shower length along and perpendicular to the shower axis, the energy fraction per calorimeter compartment or the energy fraction in the cell with the maximal energy or the one closest to the shower axis in each calorimeter compartment. The exact definition of the cluster moments is given in section 13.1. More details can be found in [59].

In ATLAS cluster moments are used within the "local hadron calibration" scheme [59]. This calibration concept foresees to apply energy corrections based on the topology of the energy distribution in a cluster. These corrections are derived from Monte Carlo simulations. Cluster moments serve to identify clusters where all the energy has been deposited electromagnetically (like from neutral pions) to calculate corrections for the calorimeter non–compensation and to calculate the corrections of energy deposits outside the calorimeter ("dead material corrections")[44] or not included in any topological clusters ("out–of–cluster corrections").

Cluster moments can also be exploited for particle identification in ATLAS. They form a basis to define jet moments that can be used to select and calibrate jets. One possible future application is the recognition of clusters from low energy hadrons produced in an additional collision not associated to the hard scattering.

In the test–beam the quality of the Monte Carlo simulation to describe the shower topology can be assessed in a clean environment with one single pion impinging on the calorimeter. Cluster moments that

[43] Some of the "cluster moments" defined in the following are not "moments" in the strict mathematical sense. A better name would be "cluster properties". Here we adopt the ATLAS naming convention.

[44] In ATLAS, dead material corrections are mainly based on the energy distribution in the calorimeter compartments. They have already been discussed in section 11.

are described by Monte Carlo simulations can be considered to be used in ATLAS, while cluster moments that are not well described should not be used for the analysis of ATLAS data.

Cluster moments are also a powerful tool to assess the Monte Carlo models in a comprehensive way. They might therefore facilitate insights in the deficiencies of the present Monte Carlo simulations. Therefore in section 13.2 detailed comparisons of the full plethora of physics lists to the data are presented.

13.1. Definition of Cluster Moments

In the following the cluster moments for which comparisons of data and Monte Carlo simulations have been carried out are defined:

$$\langle O^n \rangle = \frac{1}{E_{\text{norm}}} \cdot \sum_{\{i\,|E_i>0\}} E_i\, O^n \;\text{ with the normalisation }\; E_{\text{norm}} = \sum_{\{i\,|E_i>0\}} E_i, \tag{13}$$

where E_i is the reconstructed energy in cell i and n is the degree of the moment and O the observable. The moment is calculated with the constituent cells of the cluster. Only cells with a positive energy enter the computation of the moments.

Some of the moments refer to the shower axis which can be calculated by a principal component analysis of the energy weighted spatial correlation with respect to the centre of the cluster constituent cells. Only cells with positive energy are used:

$$C_{xx} = \frac{1}{w} \sum_{\{i\,|E_i>0\}} E_i^2\,(x_i - \langle x \rangle)^2, \tag{14}$$

$$C_{xy} = \frac{1}{w} \sum_{\{i\,|E_i>0\}} E_i^2\,(x_i - \langle x \rangle)\,(y_i - \langle y \rangle), \tag{15}$$

where the normalisation constant is calculated with:

$$w = \sum_{\{i\,|E_i>0\}} E_i^2. \tag{16}$$

The other components C_{xz}, C_{yy}, C_{yz}, C_{zz} are calculated according to C_{xx} and C_{xy} and can be combined in the symmetric matrix:

$$C = \begin{pmatrix} C_{xx} & C_{xy} & C_{xz} \\ C_{xy} & C_{yy} & C_{yz} \\ C_{xz} & C_{yz} & C_{zz} \end{pmatrix}. \tag{17}$$

With $\vec{i}$ being the vector from the interaction point (IP) to the barycentre of the cluster and $\vec{e}_{0,1,2}$ the eigenvectors of C, the shower axis $\vec{s}$ is given by:

$$\begin{aligned} \vec{s} = \vec{e}_{0,1,2} \;\text{ with smallest }\; & \angle(\vec{i}, \vec{e}_{0,1,2}), \text{if } \angle(\vec{i}, \vec{e}_{0,1,2}) \leq 30^\circ \\ & \vec{i}, \text{if } \angle(\vec{i}, \vec{e}_{0,1,2}) > 30^\circ. \end{aligned} \tag{18}$$

With the shower centre $\vec{c}$ and the shower axis $\vec{s}$ the distance of a cell i to the cluster centre along the shower axis:

$$\lambda_i = (\,\vec{x}_i - \vec{c}\,) \cdot \vec{s}, \tag{19}$$

and the radial distance of a cell i to the shower axis:

$$r_i = |\,(\,\vec{x}_i - \vec{c}\,) \times \vec{s}\,| \tag{20}$$

can be defined (see Fig. 32).

The following moments are calculated in addition to $\vec{c}$:

- $\langle r^2 \rangle$: second moment in r, the transverse shower width.
- $\langle \lambda^2 \rangle$: second moment in λ, the longitudinal shower length.
- $\langle \rho \rangle$: first moment in energy density $\rho = E/V$, with V being the cell volume.

- $\langle \rho^2 \rangle$: second moment in energy density.

Several quantities to estimate shower properties are computed:

- λ_{centre}: distance of the shower centre from the calorimeter front face measured along the shower axis (shower depth).
- f_{max}: energy fraction in the most energetic cell with respect to the cluster energy.
- f_{core}: sum of the energy fractions in the most energetic cells per compartment with respect to the cluster energy.

An illustration of the cluster moments is shown in Fig. 32[45].

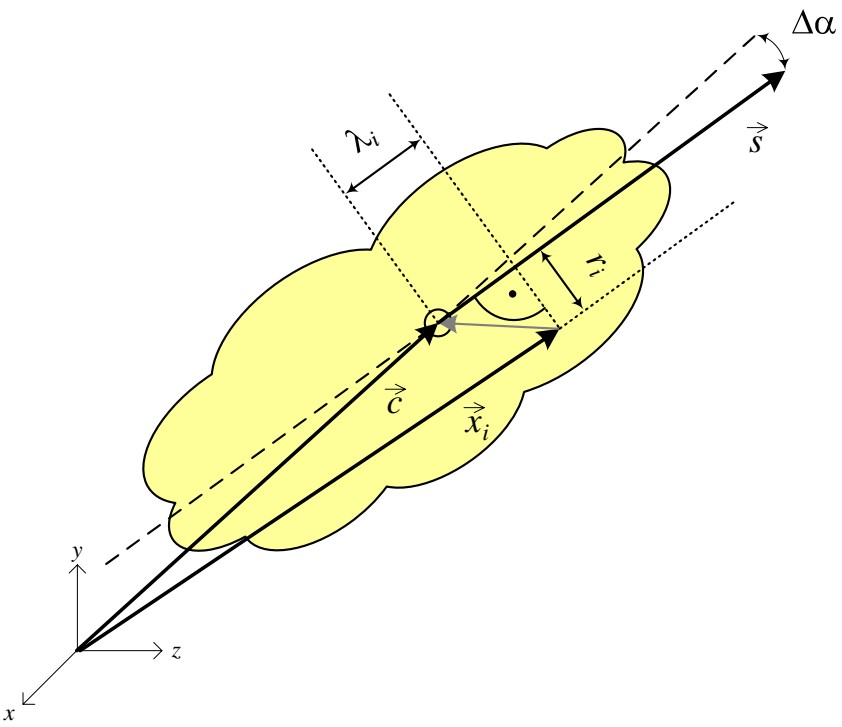

Figure 32: Sketch showing the variable used in the definition of the topological cluster moments.

For all cluster moments an energy weighted average over all topological clusters with a cluster mean pseudo–rapidity[46] $|\eta_{cl} - \eta_{\text{nom}}| < 0.3$ is used.

[45] We thank P. Loch for providing this figure.
[46] Calculated as cluster moment according to eq. 13.

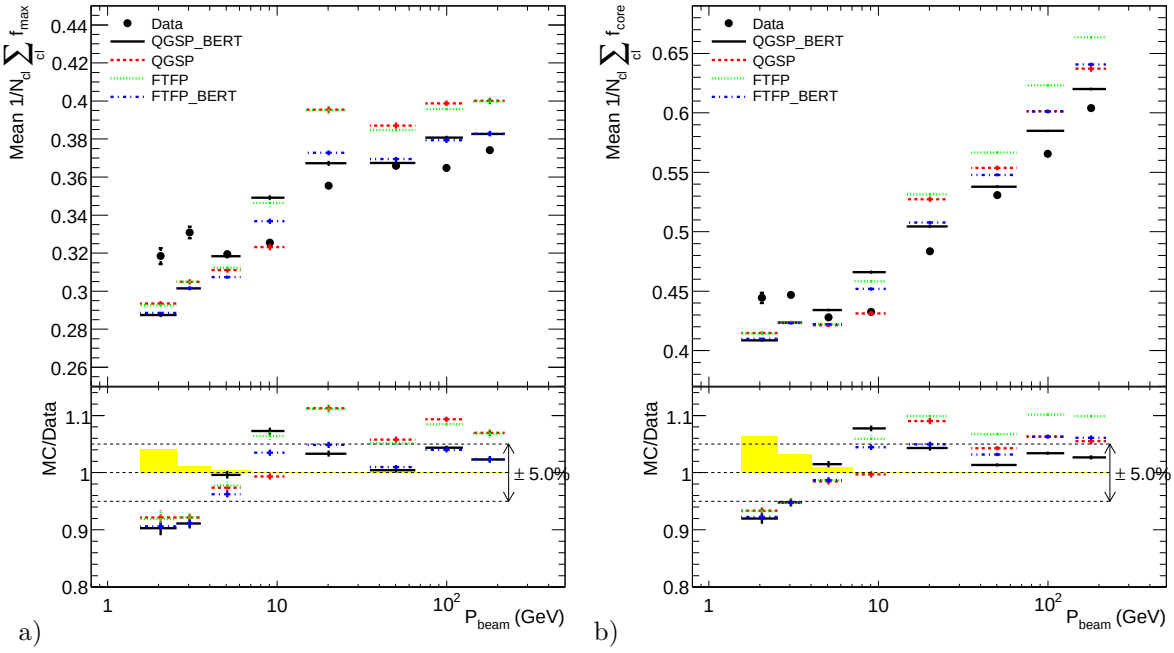

Figure 33: Mean energy fraction of the cell with the highest energy f_{max} (a) and with the sum of all cells close to the shower axis f_{core} (b) with respect to the cluster energy as a function of the beam momentum for pions with beam momenta of 2 to 180 GeV. Shown are data as closed points and Monte Carlo simulations as lines. Only statistical uncertainties are shown. The light band indicates the uncertainty due to the likelihood cut to remove muons from pion decays.

Fig. 33a) shows the mean fraction of the energy in the cell with the maximal energy with respect to the cluster energy $\langle f_{\text{max}} \rangle$ as a function of the pion momentum. The Monte Carlo simulations describe the data within 10%. The QGSP and the FTFP model give similar predictions and for both models adding the Bertini cascade gives similar results. This observable is mainly influenced by the nuclear cascade and not by the fragmentation.

Without the Bertini cascade the mean f_{max} is about 10% too high for large pion momenta, but is about 10% too low for small pion momenta. For pion momenta with $P_{\text{beam}} > 9$ GeV the Bertini cascade decreases $\langle f_{\text{max}} \rangle$. However, for 5 and 9 GeV $\langle f_{\text{max}} \rangle$ is increased. This is in better agreement with the data for $P_{\text{beam}} > 9$ GeV where the Bertini cascade makes the shower wider or narrower. For 2 GeV and 3 GeV adding the Bertini cascade has no influence and the Monte Carlo simulations are 10% lower than the data.

Fig. 33b) shows the mean fraction of the energy contained in the cells closest to the shower axis in each calorimeter compartment with respect to the total energy $\langle f_{\text{core}} \rangle$. The Monte Carlo simulations behave similarly as for $\langle f_{\text{max}} \rangle$. However, for high pion momenta this time the QGSP model describes the data better (+5%) than the Fritiof model (+10%). The QGSP_BERT physics list is 3% above the data. The description of the FTFP_BERT is a bit worse. At very low pion momenta the Monte Carlo simulations are all below the data. At 5 GeV, they describe the data, at 9 GeVthey are all 5% lower than the data (except QGSP).

It seems that both energy fractions, f_{max} and f_{core}, are influenced by the modelling of the low energetic nucleons. The fragmentation seems to play a smaller role.

13.2.2. Longitudinal Shower Depth and Length

The mean shower depth λ_{centre} and the mean shower length $\langle \lambda^2 \rangle$ (along the shower axis) are shown in Fig. 34a) and b). Both quantities increase logarithmically from low to high pion momenta. The QGSP physics list predicts showers that penetrate less in the calorimeter than the showers measured in the data.

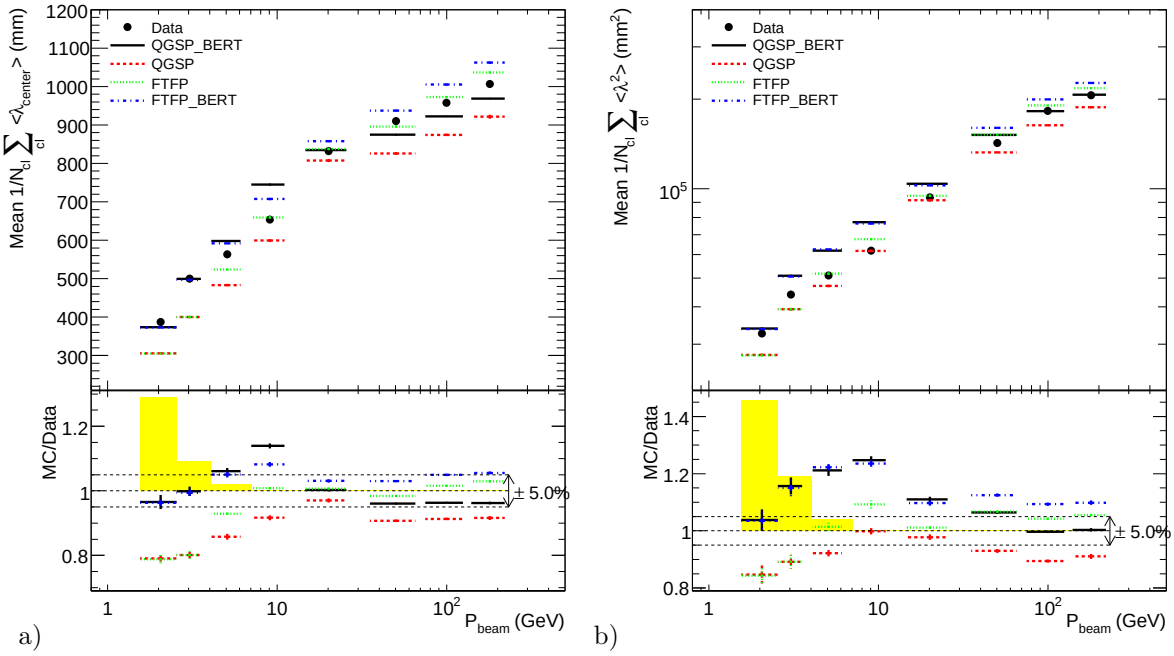

Figure 34: Mean shower depth λ_{centre} (a) and shower length $\langle\lambda^2\rangle$ (b) for pions with beam momenta from 2 to 180 GeV. Shown are data as closed points and Monte Carlo simulations as lines. Only statistical uncertainties are shown. The light band indicates the uncertainty due to the likelihood cut to remove muons from pion decays.

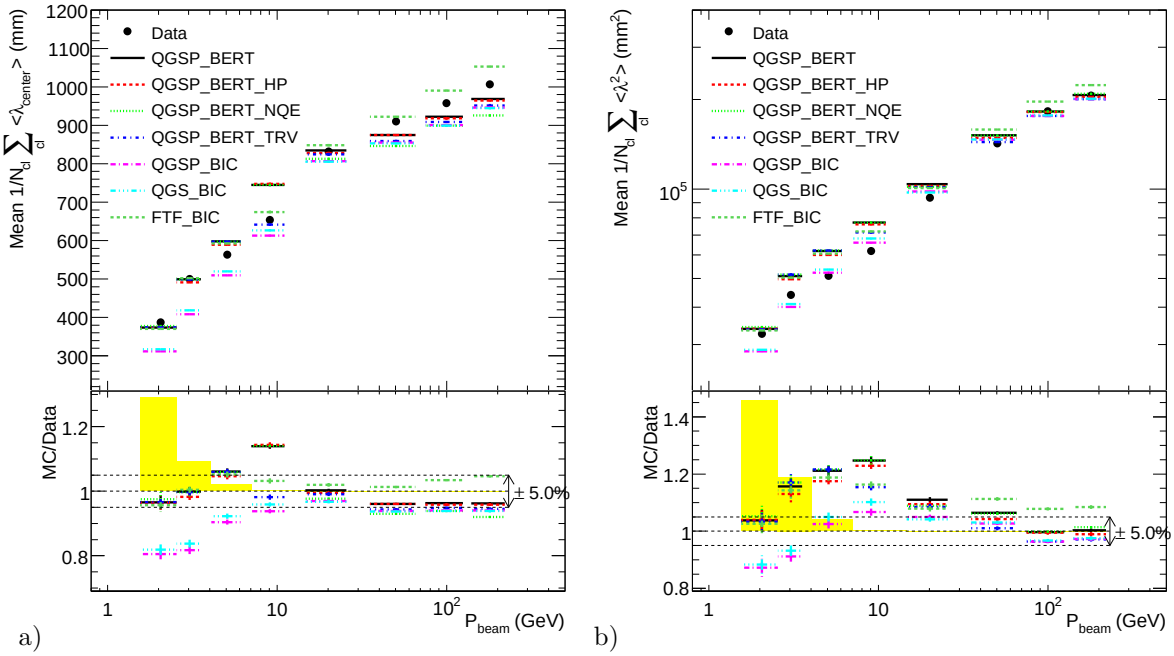

Figure 35: Mean shower depth λ_{centre} (a) and shower length $\langle\lambda^2\rangle$ (b) for pions with beam momenta of 2 to 180 GeV. Shown are data as closed points and Monte Carlo simulations as lines. Only statistical uncertainties are shown. The light band indicates the uncertainty due to the likelihood cut to remove muons from pion decays.

The mean λ_{centre} is 10% lower than in the data for high pion momenta and within −20% lower for very low pion momenta at 2–3 GeV.

Adding the Bertini cascade increases the mean shower depth by a few per cent at high pion momenta and within 10% at low pion momenta and gives a reasonable data description.

The shower predicted by the Fritiof model is longer than the one predicted by the QGSP model. It is in better agreement with the data. The FTFP physics list describes the data well at high pion momenta (±3%), but has problems at low pion momenta. Again, adding the Bertini cascade makes the shower longer. This is at high pion momenta in worse agreement with the data (+5%), but at low pion momenta in better agreement (±8%).

Fig. 35 shows the same observables for other physics lists. Adding the high precision neutron physics on top of QGSP_BERT has no effect. Changing the region of transition between the Bertini and the LEP model (QGSP_BERT_TRV) makes the shower a bit shorter in worse agreement with data. The QGSP_BERT_NQE physics list also predicts too short showers. This shows that the quasi–elastic process makes the shower longer (from −4% in QGSP_BERT to −7% QGSP_BERT_NQE).

The QGSP model with the binary cascade predicts a $\langle\lambda_{\text{centre}}\rangle$ that is 10% lower than the one in the data at large pion momenta and is too low for low pion momenta (−5% to −20%). The FTF_BIC model describes the data within 3% down to pion momenta of 5 GeV. It produces showers that are a bit longer than the ones in the data. Only for 2 GeV the $\langle\lambda_{\text{centre}}\rangle$ is 10% lower to the data. The FTF_BIC describes the data best.

The shower length is within 5% for pion momenta above 20 GeV, but 10–20% above the data for lower pion momenta where the shower in the Monte Carlo simulation is longer. The Bertini cascade makes the shower longer which is in better agreement with the data at high momenta, but in worse agreement at low momenta. The Fritiof model produces longer showers than the QGS model. The quasi-elastic scattering process has no influence on the shower length.

13.2.3. Transverse Shower Width

The second moment of the transverse shower extension $\langle r^2\rangle$ (shower width) is shown in Fig. 36. The shower width increases exponentially from 2 to 20 GeV and then decreases towards 180 GeV where it reaches a similar level to the 5 GeV point.

None of the Monte Carlo models are able to well describe the shower width. The QGSP and the FTFP models are 20–40 % below the data. The FTFP model describes the data a bit better than the QGSP model. Adding the Bertini cascade increases the shower width and improves the description of the data. For low pion momenta the QGSP_BERT and the FTFP_BERT model describe the data within ±5% For high pion momenta the QGSP_BERT model is about 10% below the data, while the FTFP_BERT is 5% below the data.

The binary cascade leads also to a wider shower. However, this increase is less than the one obtained with the Bertini cascade, and the agreement with the data is worse. The QGSP_BIC is for all pion momenta about 20% below the data. No significant difference is found between QGSP_BIC and QGS_BIC. This means that pion induced nuclear cascades play a minor role for the transverse shower extension, while the nuclear cascade induced by nucleons (proton or neutrons) have a significant influence.

The variants of the Bertini cascades do not alter the description of the transverse shower extension. Also the inclusion of the quasi–elastic scattering process does not influence the transverse shower development.

In conclusion, the data are not well described by any of the models. The transverse shower development is a bit better described by the Fritiof fragmentation model than by the QGSP model. The shower width is less influenced by the fragmentation, but rather by nuclear cascades.

13.2.4. Energy Density

The first and second energy density moments are shown in Fig. 37a) and b). The first moment is about the same for 2–3 GeV and then strongly increases towards higher energies.

The Fritiof model describes the data well down to 50 GeV within 3%. At low energy it is about 10% too high. The QGSP model predicts an energy density that is much higher than the one in the data. The discrepancy to the data rise from +10% at low pion momenta to up to +50% at $P_{\text{beam}} = 180$ GeV.

Adding the Bertini cascade decreases the energy density for both QGSP and FTFP. For the QGSP model the decrease is not enough at high pion momenta (+20%) and too much for low pion momenta

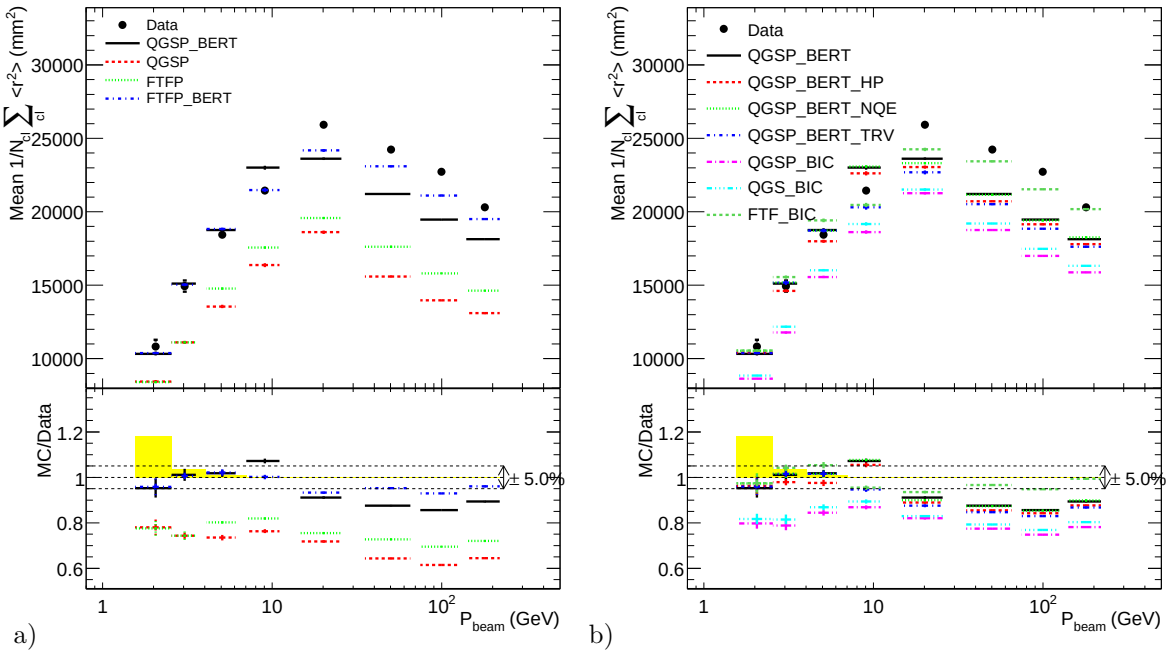

Figure 36: Mean second radial moment $\langle r^2 \rangle$ (shower width) for pions with beam momenta of 2 to 180 GeV. Shown are data as closed points and Monte Carlo simulations as lines. Only statistical uncertainties are shown. The light band indicates the uncertainty due to the likelihood cut to remove muons from pion decays.

(-10%). The FTFP_BERT physics lists describes the data best, i.e. within $\pm 5\%$ for $P_{\text{beam}} > 20$ GeV and within $\pm 10\%$ from 5 to 20 GeV.

The variants of the Bertini model have no influence. The QGSP model with the binary cascade gives a good description of the data for low pion momenta ($+5\%$), but also fails at high pion momenta ($+25\%$). The FTFP model together with the binary cascade describes the data well for high pion momenta ($\pm 5\%$), but gives a worse description at small pion momenta.

The energy density seems to be more influenced by the fragmentation model than by the intra–nuclear cascade models. At pion momenta below 5 GeV the LEP model is in better agreement than the Bertini model that is 10–20% below the data. The second energy density moments are also largely influenced by the fragmentation model. The Fritiof model describes the data best. The $\langle \rho^2 \rangle$ is within 10% of the data for $P_{\text{beam}} > 20$ GeV and above 20% for $P_{\text{beam}} > 9$ GeV. The QGSP physics list is well above the data (10% at 20 GeVand 50 % at 180 GeV). The discrepancy increases towards higher pion momenta. The Bertini cascade decreases $\langle \rho^2 \rangle$ a bit, but does not significantly improve the data description For 2 and 3 GeV the Bertini model is 35% and 20% below the data.

The variants of the Bertini cascade have no influence. The QGSP model with the binary cascade is 10% higher than the data at low pion momenta, but can not describe the data at high pion momenta. Here the QGS_BIC model($+5\%$) is in better agreement than the QGSP_BIC model ($+10\%$). The FTFP model with the binary cascade is 10% higher than the data at high pion momenta, but below 5 GeV it increasingly falls below the data and is 50% too low at 2 GeV.

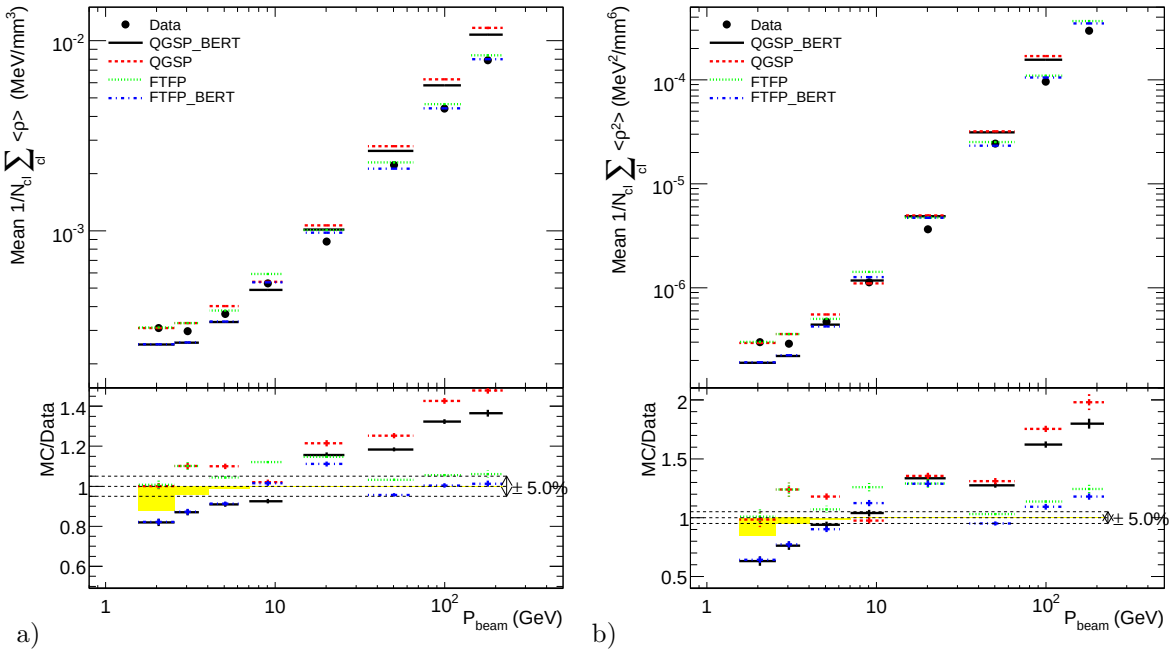

Figure 37: Mean first $\langle\rho\rangle$ (a) and second $\langle\rho^2\rangle$ (b) energy density moment for pions with beam momenta of 2 to 180 GeV. Shown are data as closed points and Monte Carlo simulations as lines. Only statistical uncertainties are shown. The light band indicates the uncertainty due to the likelihood cut to remove muons from pion decays.

physics list	longitudinal				radial	
	λ_{centre}		$\langle\lambda^2\rangle$		$\langle r^2\rangle$	
	VLE	HE	VLE	HE	VLE	HE
QGSP	−15%	−10%	−10%	−10%	−30%	−40%
QGSP_BERT	±10%	−4%	+20%	+10%	±5%	−10%
QGSP_BERT_HP	±10%	−4%	+20%	+10%	±5%	−10%
QGSP_BERT_NQE	±10%	−7%	+20%	+10%	±5%	−10%
QGSP_BERT_TRV	±10%	−5%	+20%	+8%	±5%	−10%
QGSP_BIC	−15%	−6%	±10%	±5%	−20%	−20%
QGS_BIC	−15%	−6%	±10%	±5%	−20%	−20%
FTFP	−15%	±3%	±10%	+5%	−25%	−30%
FTFP_BERT	±8%	+5%	+20%	+10%	±5%	−5%
FTF_BIC	±10%	+4%	+20%	+10%	±5%	−5%

Table 14: Summary of the comparison of the Geant4 Monte Carlo simulations to data. Compared are various physics lists to the cluster moments describing the longitudinal and transverse shower development. Indicated are typical upwards (+) or downwards (−) fluctuations in per cent.

physics list	energy density				energy fraction			
	$\langle\rho\rangle$		$\langle\rho^2\rangle$		f_{core}		f_{max}	
	VLE	HE	VLE	HE	VLE	HE	VLE	HE
QGSP	+10%	+30%	+15%	+50%	−5%	+5%	±10%	+10%
QGSP_BERT	−10%	+25%	−20%	+50%	±10%	+3%	±5%	+3%
QGSP_BERT_HP	−10%	+25%	−20%	+50%	±10%	±3%	±10%	±3%
QGSP_BERT_NQE	−10%	+25%	−20%	+50%	±10%	±3%	±10%	±2%
QGSP_BERT_TRV	−10%	+25%	−20%	+50%	±10%	±3%	±10%	±3%
QGSP_BIC	+5%	+25%	+10%	+50%	−5%	+5%	±10%	+6%
QGS_BIC	+5%	+25%	+5%	+50%	−5%	+3%	−5%	+6%
FTFP	+10%	+5%	+15%	+10%	±10%	+10%	±10%	+10%
FTFP_BERT	−10%	±3%	−20%	+10%	±10%	+5%	±10%	+3%
FTF_BIC	−10%	±5%	−30%	+10%	±10%	±2%	−10%	+3%

Table 15: Summary of the comparison of the Geant4 Monte Carlo simulations to data. Compared are various physics lists to the cluster moments describing the longitudinal and transverse shower development. Indicated are typical upwards (+) or downwards (−) fluctuations in per cent.

14. Simulation Results from Fine Momentum Scan

In the previous sections the description of the data by the Monte Carlo simulation has been discussed. To take the changing beam composition for the various beam momenta into account the Monte Carlo simulation have been compared to samples of pion and protons that were mixed according to the measured beam composition.

In this section the matching of the Bertini cascade model, the LEP model and the QGSP model in the QGSP_BERT physics list is addressed by using a fine momenta scan from 1 to 230 GeV. Only pions are simulated.

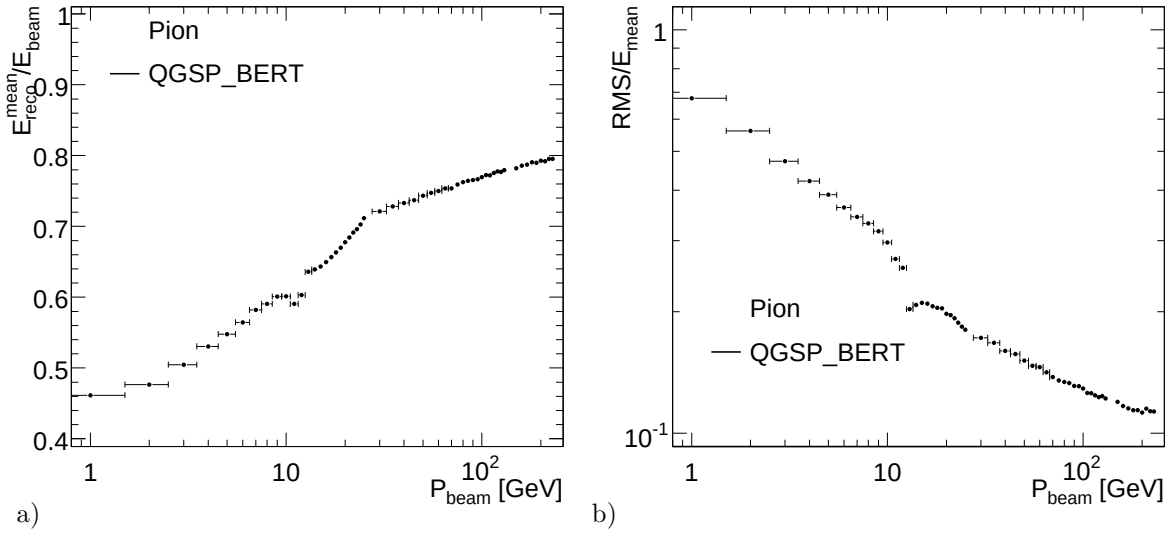

Figure 38: Mean energy (a) and resolution (b) for all topological clusters as a function of the beam momenta. The results are obtained using Geant4 Monte Carlo simulations for pions using the QGSP_BERT physics lists. The light band indicates the uncertainty due to the likelihood cut to remove muons from pion decays.

The pion response and resolution as a function of the beam momenta is shown in Fig. 38. In the transition region between the Bertini cascade and the LEP model around 10 GeV an unphysical dip is observed. The response from the Bertini cascade is higher than the one from the LEP model for similar beam momenta. The resolution is better in the LEP model than in the Bertini model. At 25 GeV which is the transition region of the LEP and the QGSP model an unphysical kink is observed for both the

response and the resolution. The resolution does not exhibit the expected energy behaviour falling with $1/\sqrt{P_{\mathrm{beam}}}$.

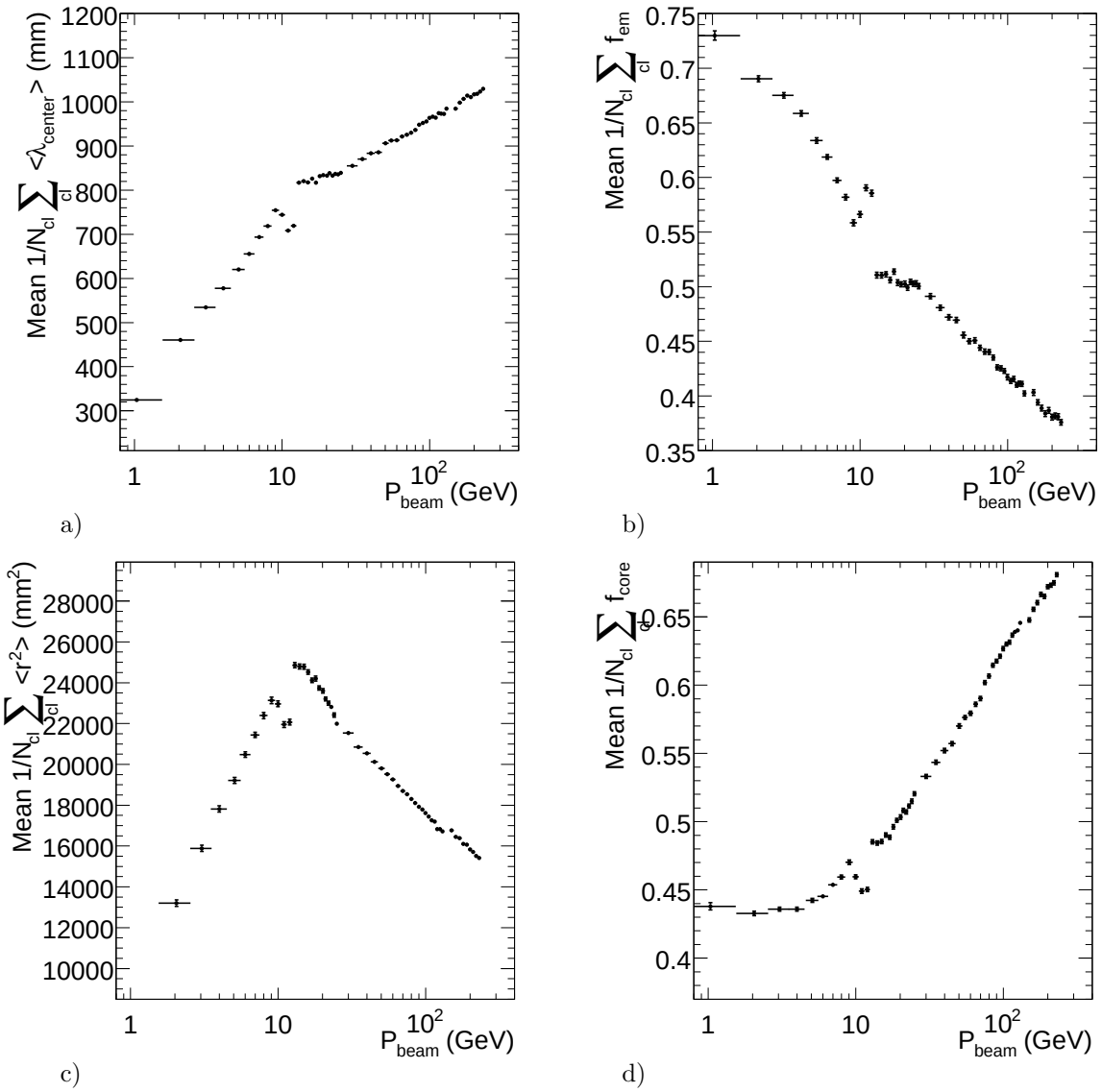

Figure 39: Mean longitudinal barycentre (a), energy fraction in the LAr calorimeter for all topological clusters (b), mean second moment of the radial shower extension (shower width) (c) and energy fraction in all cells near to the shower core for all topological clusters (d) as a function of the beam energy. The results are obtained from Geant4 Monte Carlo simulations for pions using the QGSP_BERT physics list. The light band indicates the uncertainty due to the likelihood cut to remove muons from pion decays.

Similar problems are observed for the shower depth and the fraction of the energy in the electromagnetic to the total energy (see Fig. 39). In the low momentum range below $P_{\mathrm{beam}} < 10$ GeV the shower penetrates deeper and is laterally wider than above 10 GeV. The momentum dependence suggest that there are significant uncertainties between 9 and 30 GeV.

Also the first and second moment of the energy density exhibit a unphysical behaviour in the transition region between the models. This is shown in Fig. 40.

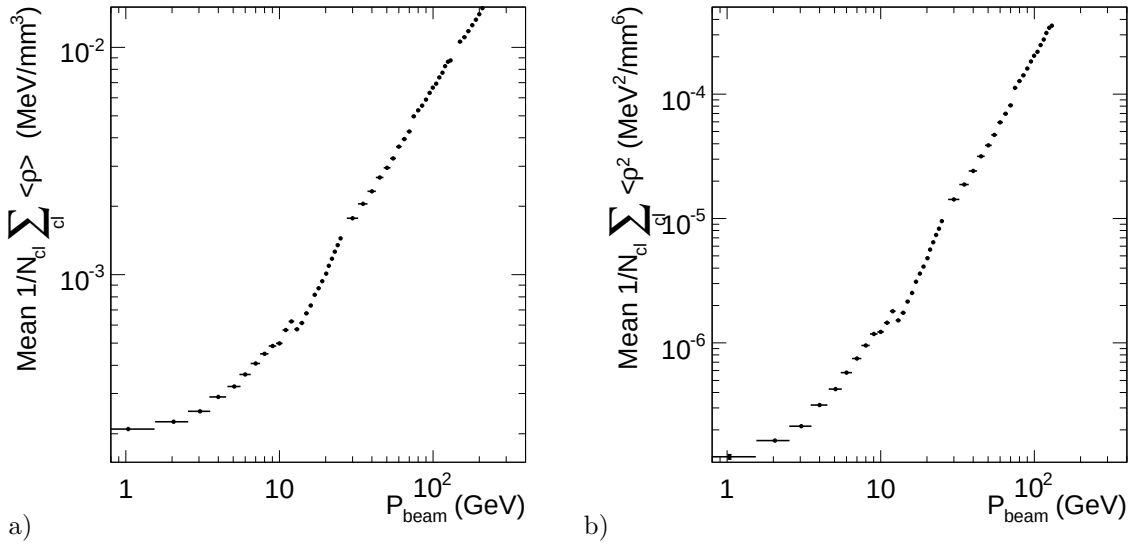

Figure 40: Mean first (a) and second moment (b) of the energy density for all topological clusters as a function of the beam energy. The results are obtained from Geant4 Monte Carlo simulations for pions using the QGSP_BERT physics list. The light band indicates the uncertainty due to the likelihood cut to remove muons from pion decays.

15. Summary of the Monte Carlo to Data Comparisons

The comparisons of the Monte Carlo simulations to the data are summarised in Table 16 and Table 17. Table 16 shows the performance of each studied physics lists in terms of response, resolution and the longitudinal and transverse shower extension. The low and high pion momentum range is given separately. The performance numbers refer to roughly averaged deviations evaluated by eye. Table 17 gives a concise overview how the Monte Carlo simulation describes the data for each physics list. The comparison is done only in a qualitative way.

The main conclusion from the comprehensive data to Monte Carlo simulations comparisons presented in the previous sections can be summarised as follows:

- The pions with momenta below 10 GeV are wider described than the pions at higher momenta
- The resolution is too narrow in the Monte Carlo simulation compared to data for most physics lists. Only QGSP gives a worse resolution than in data.
- Adding the nuclear cascade models increases the response and brings the simulation in better agreement with the data. The increase is smaller for the binary cascade than for the Bertini cascade. For the QGSP_BERT physics list the response is described within 1% for high pion momenta and within 5% for low pion momenta.
- The longitudinal shower development is largely influenced by the fragmentation model. The Fritiof model produces hadronic showers that are longer than the ones in the quark gluon string model. The Fritiof model is in better agreement with the data. The showers are a bit longer than the ones in the data. For the quark gluon string model the shower starts and ends too early.
- Adding the nuclear cascade models makes the shower longer, and in better agreement with the data in case of the quark gluon string fragmentation model, while in worse agreement in case of the Fritiof model. The Bertini nuclear cascade produces longer showers than the binary cascade, but the showers are still shorter than the ones in the data.
- The radial extension of the shower is not well reproduced by any of the simulations. The data are wider than the Monte Carlo simulations. The radial extension of the shower is only little influenced by the fragmentation models.

- The shower get wider with the nuclear cascade models. The simulation using the Bertini cascade are in better agreement with the data than the ones using the binary cascades.
- Quasi–elastic scattering makes the shower longer. This improves the description of the data. The radial extension is not influenced.
- The detailed tracking of neutrons down to thermal energies has no influence on the data description.
- The Bertini model has problems to describe the data for pion momenta around 9 GeV, where the low energy parametrised model is clearly better. However, lowering the region of applicability in the Bertini cascade has little effect. It leads to showers that are a bit shorter and narrower.
- The energy density is best described by the Fritiof fragmentation model. The inclusion of the nuclear cascade models has only little influence.
- The predictions of the low energy parametrised model is not well matched with the Bertini cascade at the low energy end and with the quark gluon string model at the high energy end. This leads to a significant uncertainty of the predictions in the energy range from a few GeV to 20–30 GeV.

In summary, there is no physics list that describes all features of the data. The best overall description of the data is obtained with the Fritiof model with or without the Bertini cascade and with the quark gluon string model with the Bertini cascade.

For the analysis of the first collision data, ATLAS has adopted the QGSP_BERT physics list as a default. This decision was mainly based on the better description of the response and the longitudinal and radial shower extension.

The Fritiof model with the Bertini or the binary nuclear cascades represents an interesting alternative, in particular the simulation of longer showers and the better description of the energy density allows for interesting systematics studies.

physics list	response		resolution		shower development			
					longitudinal		transverse	
	VLE	HE	VLE	HE	VLE	HE	VLE	HE
QGSP	−8%	−4%	−5%	±3%	−50%	−15%	+5%	+5%
QGSP_BERT	+5%	+1%	−8%	−5%	±20%	−5%	±3%	+2%
QGSP_BERT_HP	+5%	+1%	−8%	−5%	±20%	−5%	±3%	+2%
QGSP_BERT_NQE	+5%	+1%	−8%	−5%	±20%	−15%	±3%	+2%
QGSP_BERT_TRV	+5%	+1%	−8%	−5%	±20%	−5%	±3%	+2%
QGSP_BIC	−5%	−1%	−8%	−5%	−20%	−15%	+4%	+3%
QGS_BIC	−3%	±1%	−10%	−5%	−20%	−15%	+4%	+3%
FTFP	±5%	−3%	−10%	−5%	−50%	±2%	+5%	+4%
FTFP_BERT	+8%	+2%	−15%	−10%	±20%	+10%	±3%	+1%
FTF_BIC	+10%	+3%	−8%	−5%	±30%	±10%	−5%	+1%

Table 16: Summary of the comparison of the Geant4 Monte Carlo simulations to data. Compared are various physics lists for the response, resolution as well as for the longitudinal and transverse shower extension. Indicated are typical upwards (+) or downwards (−) fluctuations in percent. The longitudinal shower development refers to the energy deposition in the second Tile calorimeter compartment. The transverse shower development refers to the mean energy fraction in a narrow cone around the shower axis. The symbol ± is used when the Monte Carlo simulation is for some momenta above and for some other below the data.

physics list	response	resolution	longitudinal	radial
QGSP	low	ok	too short	too narrow
QGSP_BERT	ok	low	short	narrow
QGSP_BERT_HP	ok	low	short	narrow
QGSP_BERT_NQE	ok	low	too short	narrow
QGSP_BERT_TRV	ok	low	short	narrow
QGSP_BIC	low	low	too short	too narrow
QGS_BIC	low	low	too short	too narrow
FTFP	ok	low	short	too narrow
FTFP_BERT	high	low	long	ok
FTFP_BIC	high	low	long	narrow

Table 17: Rough summary of the comparison of the Geant4 Monte Carlo simulations to data. Compared are various physics lists for the response, resolution as well as for the longitudinal and transverse shower extension.

16. Conclusion

Data of the combined test–beam taken in the year 2004, where a full slice of the ATLAS detector has been exposed to pion beams from 2 to 180 GeV have been analysed. In view of the LHC proton–proton collision data taking, analysis techniques planned to be used for the reconstruction of the hadronic final state have been investigated in detail.

Emphasis has been put on the comparison of the data with Monte Carlo simulations in particular in the momentum range below 9 GeV, since in this region only the combined barrel test–beam has data available. The Monte Carlo simulations have difficulties to accurately describe the pion data for momenta below 9 GeV. Since pions at such momentum carry a large fraction of the jet energies, it can be expected that the Monte Carlo simulation will not be able to give a good description of the hadronic final state for proton–proton collisions.

All models predict a resolution that is better than the one measured in the data. For QGSP_BERT the resolution in the Monte Carlo is better by 5–10%. The Bertini nuclear cascade model increases the response and decreases the resolution which is in better agreement to data. For pion momenta below 10 GeV the data are described within 5%, while for pion momenta above 10 GeV the data are described within 2%.

Generally, the use of nuclear cascade models gives a better description of the data. The Bertini cascade is preferred over the binary cascade.

The radial and the longitudinal shower development is largely influenced by the nuclear cascade models. The quark gluon string fragmentation model together with the Bertini nuclear cascade (QGSP_BERT) gives the best overall description of the data. The longitudinal shower development at high pion momenta is reasonably described, but at low pion momenta large discrepancies are observed. For all pion momenta the simulated showers remain shorter and narrower than the ones in the data. Nevertheless this physics list is recommended for the analysis of the first ATLAS collision data.

Simulations based on the Fritiof fragmentation models might offer an interesting alternative for systematics studies. Simulations with this physics list (FTFP_BERT or FTF_BIC) produce showers that are longer than the one in the data and the energy density is better described.

The present Monte Carlo simulations suffer from a mismatch between the predictions of the nuclear cascade models, the low energy parametrised models and the high energy quark gluon models. This leads to an uncertainty of the description of the pion response and the shower topology of a few per cent in the pion momentum from 5 to 9 GeV to 20 to 25 GeV that limit the possibility to correctly describe jets in proton proton collisions.

Acknowledgements

A very important ingredient of the 2004 ATLAS CTB has been the mechanics of the two calorimeters support and movement. We would like to acknowledge Danilo Giugni, Simone Coelli and Giampiero Braga from INFN Milano for the design, overview of the production and testing of the LAr calorimeter support table. We wish to thank Claude Ferrari, Pierre Gimenez, Yves Bonnet, Denis Gacon and Alain Pinget of CERN EN/MEF group for the continuous mechanical support provided in the CERN SPS North Area during the installation of the setup and the data taking.

We are grateful to the staff of the SPS for the excellent beam conditions and assistance provided during our tests. We acknowledge the support of ANPCyT, Argentina; Yerevan Physics Institute, Armenia; ARC and DEST, Australia; Bundesministerium fu rWissenschaft und Forschung, Austria; National Academy of Sciences of Azerbaijan; State Committee on Science and Technologies of the Republic of Belarus; CNPq and FINEP, Brazil; NSERC, NRC, and CFI, Canada; CERN; NSFC, China; Ministry of Education, Youth and Sports of the Czech Republic, Ministry of Industry and Trade of the Czech Republic, and Committee for Collaboration of the Czech Republic with CERN; Danish Natural Science Research Council; European Commission, through the ARTEMIS Research Training Network; IN2P3-CNRS and Dapnia-CEA, France; Georgian Academy of Sciences; BMBF, HGF, DFG and MPG, Germany; Ministry of Education and Religion, through the EPEAEK program PYTHAGORAS II and GSRT, Greece; ISF, MINERVA, GIF, DIP, and Benoziyo Center, Israel; INFN, Italy; MEXT, Japan; CNRST, Morocco; FOM and NWO, Netherlands; The Research Council of Norway; Ministry of Science and Higher Education, Poland; GRICES and FCT, Portugal; Ministry of Education and Research, Romania; Ministry of Education and Science of the Russian Federation, Russian Federal Agency of Science and Innovations, and Russian Federal Agency of Atomic Energy; JINR; Ministry of Science, Serbia; Department of International Science and Technology Cooperation, Ministry of Education of the Slovak Republic; Slovenian Research Agency, Ministry of Higher Education, Science and Technology, Slovenia; Ministerio de Educacion yCiencia, Spain; The Swedish Research Council, The Knut and Alice Wallenberg Foundation, Sweden; State Secretariat for Education and Science, Swiss National Science Foundation, and Cantons of Bern and Geneva, Switzerland; National Science Council, Taiwan; TAEK, Turkey; The Science and Technology Facilities Council and The Leverhulme Trust, United Kingdom; DOE and NSF, United States of America.

References

[1] E. Abat et al., Study of the response of the ATLAS central calorimeter to pions of energies from 3 to 9 GeV, Nucl. Instrum. Meth. A 607 (2009) 372.

[2] S. Akhmadalev et al., Results from a new combined test of an electromagnetic liquid argon calorimeter with a hadronic scintillating-tile calorimeter, Nucl. Instrum. Meth. A 449 (2000) 461.

[3] B. Girolamo et al., Beamline instrumentation in the 2004 combined atlas testbeam, Tech. Rep. ATLAS-TECH-PUB-2005-001, CERN, Geneva (Switzerland) (2005).

[4] M. Aharrouche et al., Energy linearity and resolution of the ATLAS electromagnetic barrel calorimeter in an electron test- beam, Nucl. Instrum. Meth. A 568 (2006) 601.

[5] M. Delmastro et al., Response of th ATLAS liquid argon electromagnetic barrel calorimeter to electrons from 1 to 100 GeV at the 2004 ATLAS combined test-beam, Tech. Rep. ATL-LARG-INT-2009-007, CERN, Geneva (Switzerland) (2009).

[6] M. Aleksa et al., Measurement of the response of the ATLAS liquid argon barrel calorimeter to electrons at the 2004 combined test-beam, Nucl. Instrum. and Methods A 614 (2010) 400.

[7] G. Aad et al., The ATLAS experiment at the cern large hadron collider, JINST 3 S08003.

[8] ATLAS Collaboration, Lar calorimeter technical design report, Tech. Rep. CERN/LHCC/96-41, CERN, Geneva (Switzerland) (1996).

[9] B. Aubert et al., Construction, assembly and tests of the ATLAS electromagnetic barrel calorimeter, Nucl. Instrum. Meth. A558 (2006) 388.

[10] ATLAS Collaboration, Tile calorimeter technical design report, Tech. Rep. CERN/LHCC/96-42, CERN, Geneva (Switzerland) (1996).

[11] M. Aleksa et al., ATLAS combined testbeam: Computation and validation of the electronic calibration constants for the electromagnetic calorimeter, Tech. Rep. ATL-LARG-PUB-2006-003, CERN, Geneva (Switzerland) (Apr 2006).

[12] W. E. Cleland, E. G. Stern, Signal processing considered for liquid ionization calorimeter in a high rate enviroment, Nucl. Instrum. Meth. A 338 (1994) 467.

[13] M. Delmastro, Energy reconstruction and calibration algorithms for the ATLAS electromagnetic calorimeter, Tech. Rep. CERN-THESIS-2003-033, CERN, Geneva (Switzerland) (2003).

[14] D. Banfi, M. Delmastro and M. Fanti, Cell response equalization of the ATLAS electromagnetic calorimeter without the direct knowledge of the ionization signals, J. Instrum. 1 (2006) P08001.

[15] P. Amaral et al., Nucl. Instrum. Meth. A 606 (2009) 362.

[16] M. Hurwitz et al., Performance and calibration of the TileCal fast readout using the charge injection system, Tech. Rep. ATL-COM-TILECAL-2008-003, CERN, Geneva (Switzerland) (2008).

[17] E. Starchenko et al., Cesium monitoring system for ATLAS hadron calorimeter, Nucl. Instrum. Meth. A 494 (2002) 381.

[18] N. Shalanda et al., Radioactive source control and electronics for the ATLAS Tile calorimeter cesium calibration system, Nucl. Instrum. Meth. A 508 (2003) 276.

[19] K. J. Anderson et al., Calibration of ATLAS Tile calorimeter at electromagnetic scale, Tech. Rep. ATL-COM-TILECAL-2008-016, CERN, Geneva (Switzerland) (November 2008).

[20] K. J. Anderson et al., The effect of Tile light collection reduction along radius on the ATLAS Tile calorimeter uniformity, Tech. Rep. ATL-TILECAL-PUB-2009-005, CERN, Geneva (Switzerland) (2009).

[21] W. Lampl et al., Calorimeter clustering algorithms : Description and performance, Tech. Rep. ATL-LARG-PUB-2008-002, CERN, Geneva (Switzerland) (2008).

[22] T. Carli and P. Speckmayer, Study of energy reconstruction algorithms for pions from 2 to 180 GeV measured with the ATLAS barrel calorimeter at the CERN SPS test-beam, Tech. Rep. ATL-COM-CAL-2010-001, CERN, Geneva (Switzerland) (2010).

[23] S. Agostinelli et al., Nucl. Instrum. Meth. A 506 (2003) 250.

[24] H. P. Wellisch and D. Axen, Phys. Rev. C 54 (1996) 1329.

[25] V. S. Barashenkov, Tech. Rep. P2-90-158, Dubna (Russia) (1997).

[26] G. Folger and J.-P. Wellisch, String parton models in geant4, Proceedings of International conference on: Computing in High Energy Physics, La Jolla (California) nucl-th/0306007.

[27] N. S. Amelin et al., Phys. Rev. Lett. 67 (1991) 1523.

[28] N. S. Amelin et al., Nucl. Phys. A 544 (1992) 463.

[29] L. V. Bravina et al., Nucl. Phys. A 566 (1994) 461.

[30] L. V. Bravina et al, Phys. Lett. B 344 (1995) 49.

[31] B. Andersson et al., Nucl. Phys. B 281 (1987) 289.

[32] B. Andersson, A. Tai and B. H. Sa, Z. Phys. C 70 (1996) 499.

[33] B. Nilsson-Almquist and E. Stenlund, Comp. Phys. Commun. 43 (1987) 387.

[34] B. Ganhuyag and V. Uzhinskii, Czech. Journal of Physics 47 (1997) 913.

[35] M. P. Guthrie, R. G. Alsmiller and H. W. Bertini, Nucl. Instr. and Meth. 66 (1968) 29.

[36] H. W. Bertini and P. Guthrie, Nucl. Instr. and Meth. A 169 (1971) 670.

[37] N. V. Stepanov, ITEP Preprint ITEP-55 (Moscow).

[38] G. Folger, V. N. Ivanchenko and J. P. Wellisch, Eur. Phys. J. A 21 (2004) 407.

[39] H. S. Fesefeldt, Pitha-85-02, Tech. Rep. CERN/LHCC/96-41, Aachen (Germany) (1996).

[40] M. Baker and K. A. Ter-Martirosyan, Phys. Rev. D 18 (1978) 4120.

[41] B. Andersson et al., Phys. Rep. 97 (1983) 31.

[42] S. Scalettar, P. J. Doe, H. J. Mahler and H. H. Chen, Ionisation recombination in liquid argon low drift fields, Phys. Rev. A 52 (1981) 2419.

[43] S. Amoruso et al., Study of electron combination in liquid argon with the icarus tpc, Nucl. Inst. and Meth. A 523 (2004) 275.

[44] J. B. Birks, Phys. Rev. 86 (1952) 569.

[45] J. B. Birks, The theory and practice of scintillation counting, New York, Pergamon Press.

[46] T. Carli, K.-J. Grahn and P. Speckmeyer, Implementation of the Recombination Effects in the ATLAS simulation, in preparation.

[47] J. P. Archambault et al., The simulation of the ATLAS liquid argon calorimetry, Tech. Rep. ATL-LARG-PUB-2009-001, CERN, Geneva (Switzerland) (2009).

[48] W. Lampl et al., Digitisation of the Lar calorimeter for CSC simulations, Tech. Rep. ATL-LARG-PUB-2007-011, CERN, Geneva (Switzerland) (November 2007).

[49] R. L. Craun, D. L. Smith, Analysis of response data for several organic scintillators, Nucl. Instr. and Meth. 80 (1970) 239.

[50] G. Schlager, The energy response of the atlas calorimeter system, Tech. Rep. CERN-THESIS-2006-056, CERN, Geneva (Switzerland) (November 2006).

[51] F. Spano, Simulation of the full noise pattern in tile calorimeter front end electronics : a phenomenological approach to coherent effects, Tech. Rep. ATL-COM-TILECAL-2008-009, CERN, Geneva (Switzerland) (July 2008).

[52] M. Simonyan, Performance of the ATLAS Tile calorimeter to pions and protons, Tech. Rep. CERN-THESIS-2008-032, CERN, Geneva (Switzerland) (2008).

[53] M. Simonyan et al., Measurement of pion and proton longitudinal shower profiles up to 20 nuclear interaction lengths with the ATLAS Tile calorimeter, Tech. Rep. ATL-TILECAL-PUB-2007-008, CERN, Geneva (Switzerland) (2006).

[54] A. Fabich, Decay muons, Tech. rep. (talk given in the CTB meeting, 19.4.2005).

[55] G. Aad et al., Expected performance of the ATLAS experiment : Detector, trigger and physics, arXiv:0901.0512, CERN-OPEN-2008-020, CERN, Geneva (Switzerland).

[56] K. J. Grahn et al., A layer correlation technique for pion energy calibration at the 2004 ATLAS combined beam test; to be published.

[57] J. Abat et al., Study of energy response and resolution of the ATLAS barrel calorimeter to hadrons of energies from 20 to 350 GeV; submitted to NIM.

[58] T. Carli et al., Study of the response of the hadronic barrel calorimeter in the ATLAS combined test-beam to pions of energies from 20 to 350 GeV for beam impact points from 0.2 to 0.65, Tech. Rep. ATL-TILECAL-PUB-2009-00, CERN, Geneva (Switzerland) (2009).

[59] T. Barillari et al., Local hadronic calibration, Tech. rep., CERN, Geneva (Switzerland) (2009).

Appendix A: Result Tables

combined response					
P_{beam} (GeV)	$E_{\text{reco}}^{\text{mean}}/P_{\text{beam}}$	Stat.	Scale (%)	Long. Weight (%)	Pion Decay (%)
2.05	0.439	0.007	0.891	0.04	10.3
3.05	0.479	0.005	0.954	0.03	3.0
5.09	0.525	0.003	0.911	0.03	0.0
9.04	0.595	0.002	0.890	0.02	0.0
20.16	0.671	0.001	0.854	0.03	0.0
50.29	0.712	0.001	0.866	0.04	0.0
99.80	0.742	0.001	0.875	0.05	0.0
179.68	0.759	0.001	0.883	0.05	0.0

Table 18: Measured beam momentum, relative mean response, statistical uncertainty and relative systematical uncertainty (in per cent) due to the overall energy scale, longitudinal and the bias due to the removal of the pion decays.

Tile only response					
P_{beam} (GeV)	$E_{\text{reco}}^{\text{mean}}/P_{\text{beam}}$	Stat.	Scale (%)	long. weight (%)	Pion decay (%)
2.05	0.323	0.011	0.985	0.07	40
3.05	0.424	0.010	1.186	0.06	12
5.09	0.530	0.007	1.154	0.06	0.2
9.04	0.687	0.004	1.074	0.07	0.4
20.16	0.774	0.002	1.020	0.08	0.0
50.29	0.807	0.001	1.007	0.10	0.0
99.80	0.826	0.001	1.003	0.11	0.0
179.68	0.830	0.002	1.002	0.12	0.0

Table 19: Measured beam momentum, relative mean response for pions that traverse the LAr calorimeter as minimally ionising particles, statistical uncertainty and relative systematical uncertainty (in per cent) due to the overall energy scale, the longitudinal weights and the bias due to the removal of the pion decays.

Appendix B: Software Information

The simulation of the Monte Carlo events has been done with the ATHENA release version 12.0.95. Some packages have been modified to include Birks law These modifications are meanwhile part of the ATLAS software

In the simulation of the barrel calorimeter (in case of the test–beam) by default no cut is applied on the time of the energy deposition. The time cut has been activated. The simulated energy depositions are convoluted with the pulse-shape to take the time structure of the hadronic shower into account.

For the reconstruction the release 12.0.7 has been used. The reconstruction used some modifications to improve the energy reconstruction.

For the TileCal the improvements in the pion energy reconstruction that have been worked out by the TileCal pion energy reconstruction task-force in the year 2007 and 2008 and are in the ATLAS software since The tags are summarised in Table 20.

The tag for the energy reconstruction in the LAr are tabulated in [5].

Some of the modifications were only needed for the local hadronic calibration. These modifications are not necessary for the study presented here, but are relevant for future work.

Calorimeter/CaloCnv/CaloCondAthenaPool/CaloCondAthenaPool-00-00-00-01
Calorimeter/CaloClusterCorrection/CaloClusterCorrection-00-02-71-04
Calorimeter/CaloConditions/CaloConditions-00-00-02-02
Calorimeter/CaloEvent/CaloEvent-01-02-31-06
Calorimeter/CaloRec/CaloRec-02-06-97-12
Calorimeter/CaloTools/CaloTools-00-01-68-10
Calorimeter/CaloUtils/CaloUtils-00-02-75-03
LArCalorimeter/LArCalibTools/LArCalibTools-00-03-31-01
LArCalorimeter/LArTestBeam/LArTBRec/LArTBRec-00-02-23
TileCalorimeter/TileCalib/TileCalibCondObjects/TileCalibCondObjects-00-00-01
TileCalorimeter/TileCalibObjects/TileCalibObjects-00-07-06
TileCalorimeter/TileConditions/TileConditions-00-05-25-12
TileCalorimeter/TileEvent/TileEvent-00-06-13
TileCalorimeter/TileIdentifier/TileIdentifier-00-01-06
TileCalorimeter/TileSvc/TileByteStream/TileByteStream-00-04-07
TileCalorimeter/TileRecUtils/TileRecUtils-00-03-06-11
TileCalorimeter/TileTBRec/TileTBRec-00-03-16-10
InnerDetector/InDetTestBeam/InDetTestBeamAlgs/InDetTestBeamCBNT/InDetTestBeamCBNT-00-01-67-01

Table 20: Summary of the software modifications that have been used in the reconstruction on top of the standard Atlas software release version 12.0.7.

Appendix C: Topological Cluster Moment Distributions

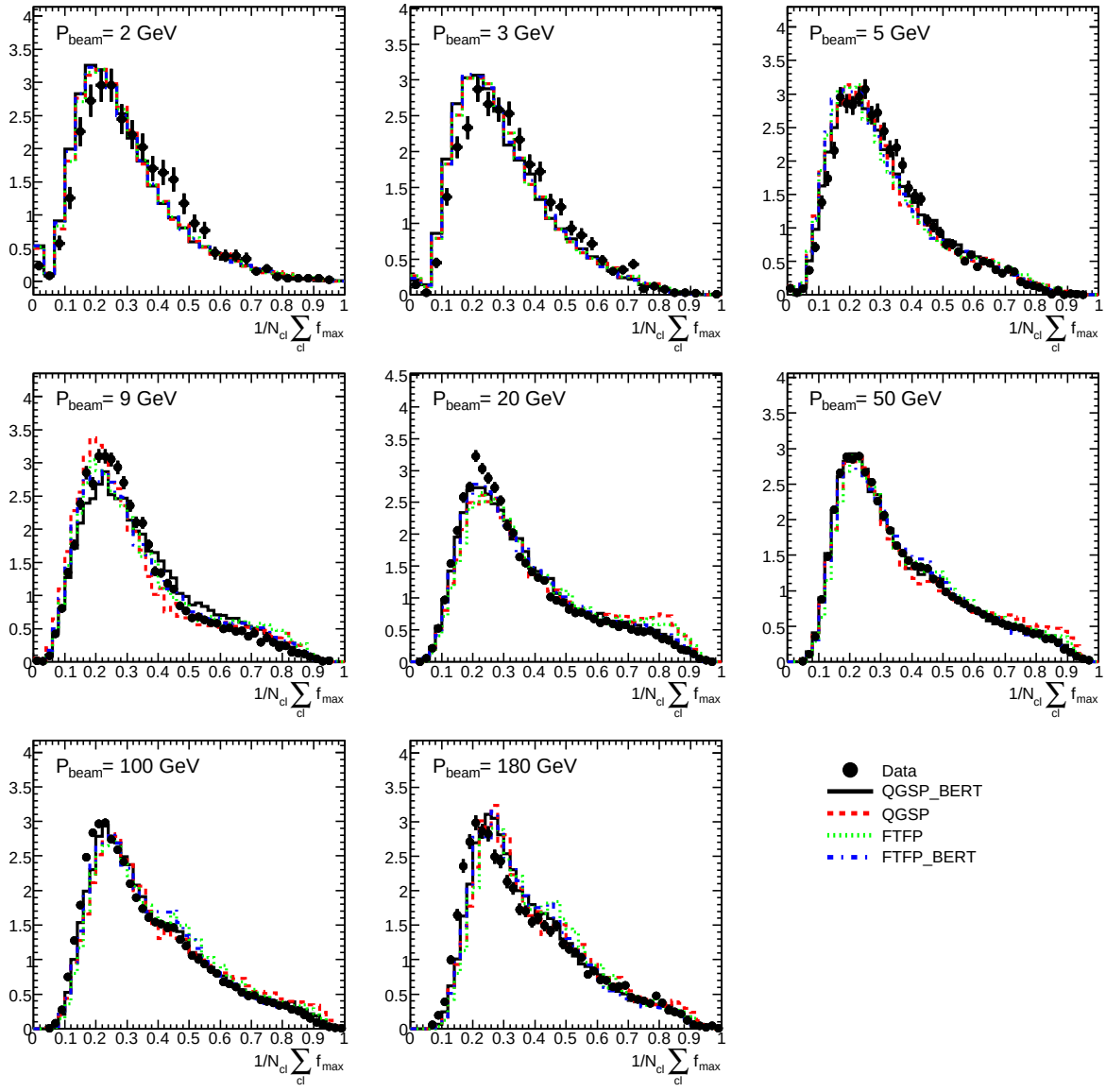

Figure 41: Distribution of the energy fraction of the cell with the highest energy with respect to the total cluster energy $f_{\max}$ for pions with beam momenta from 2 to 180 GeV. Shown are data as closed points and Monte Carlo simulations as lines. Only statistical uncertainties are shown.

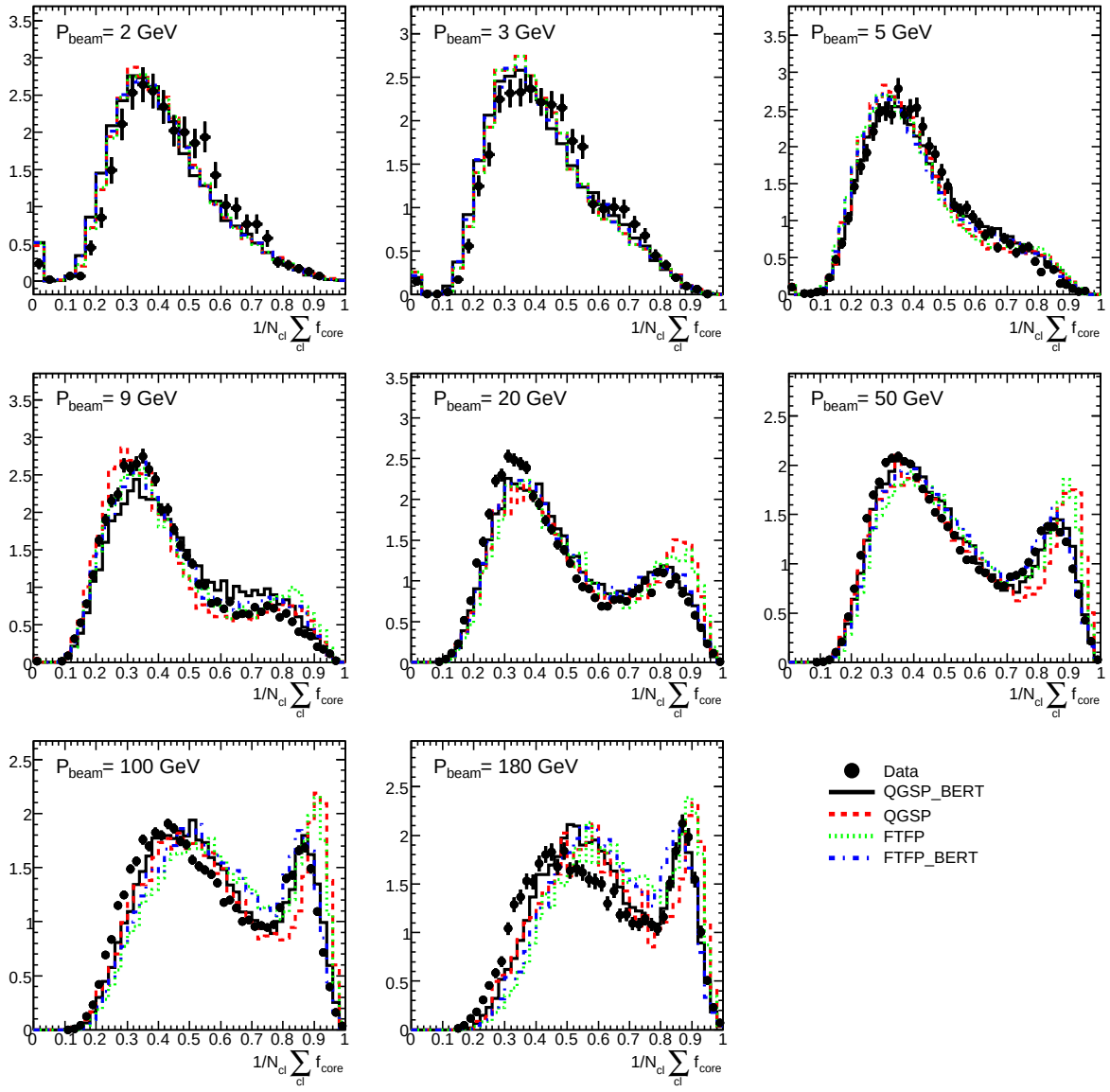

Figure 42: Distribution of the energy fraction of the sum of the cells close to the shower axis with respect to the total cluster energy f_{core} for pions with beam momenta from 2 to 180 GeV. Shown are data as closed points and Monte Carlo simulations as lines. Only statistical uncertainties are shown.

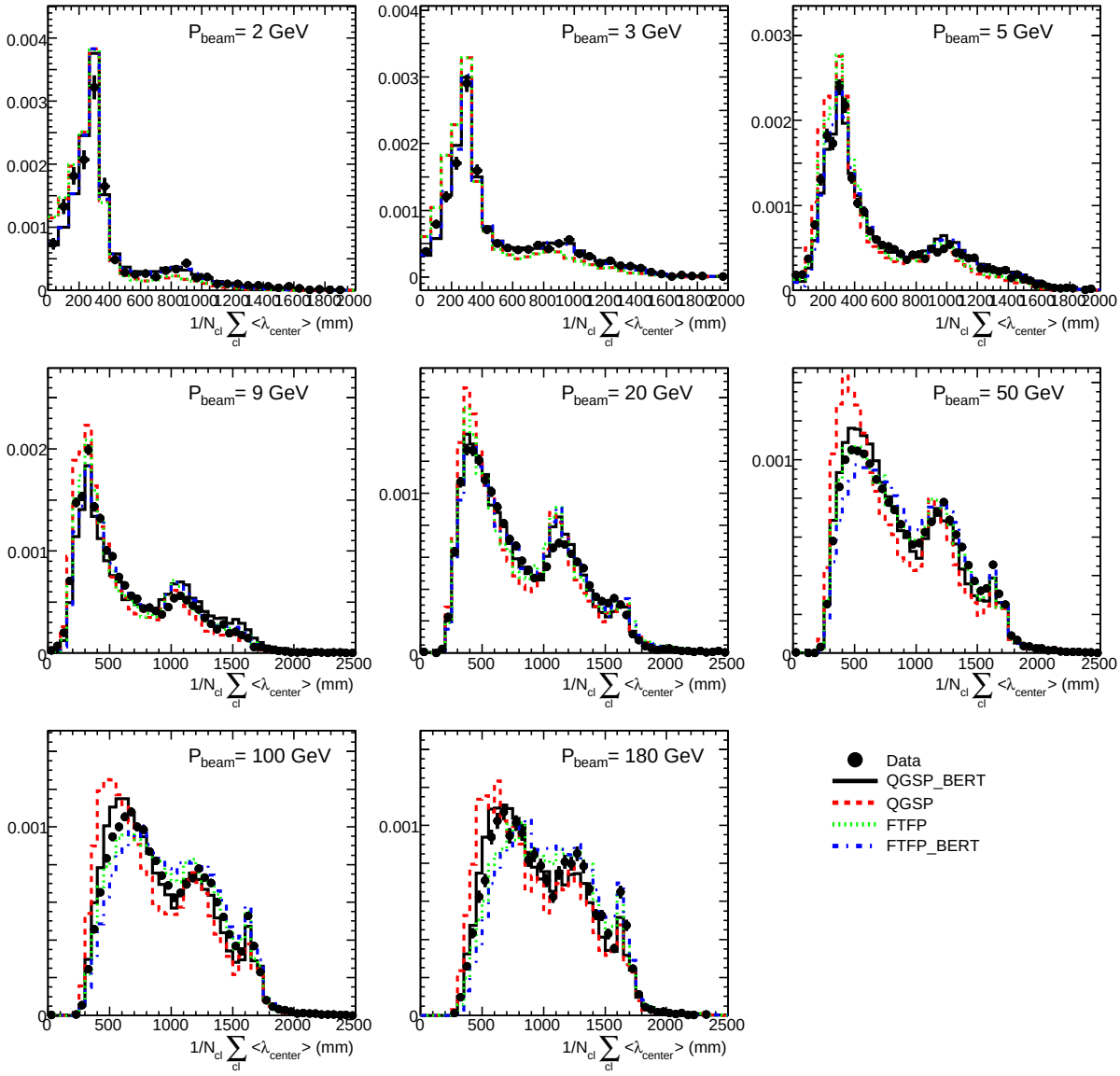

Figure 43: Distribution of the shower depth λ_{centre} for pions with beam momenta from 2 to 180 GeV. Shown are data as closed points and Monte Carlo simulations as lines. Only statistical uncertainties are shown.

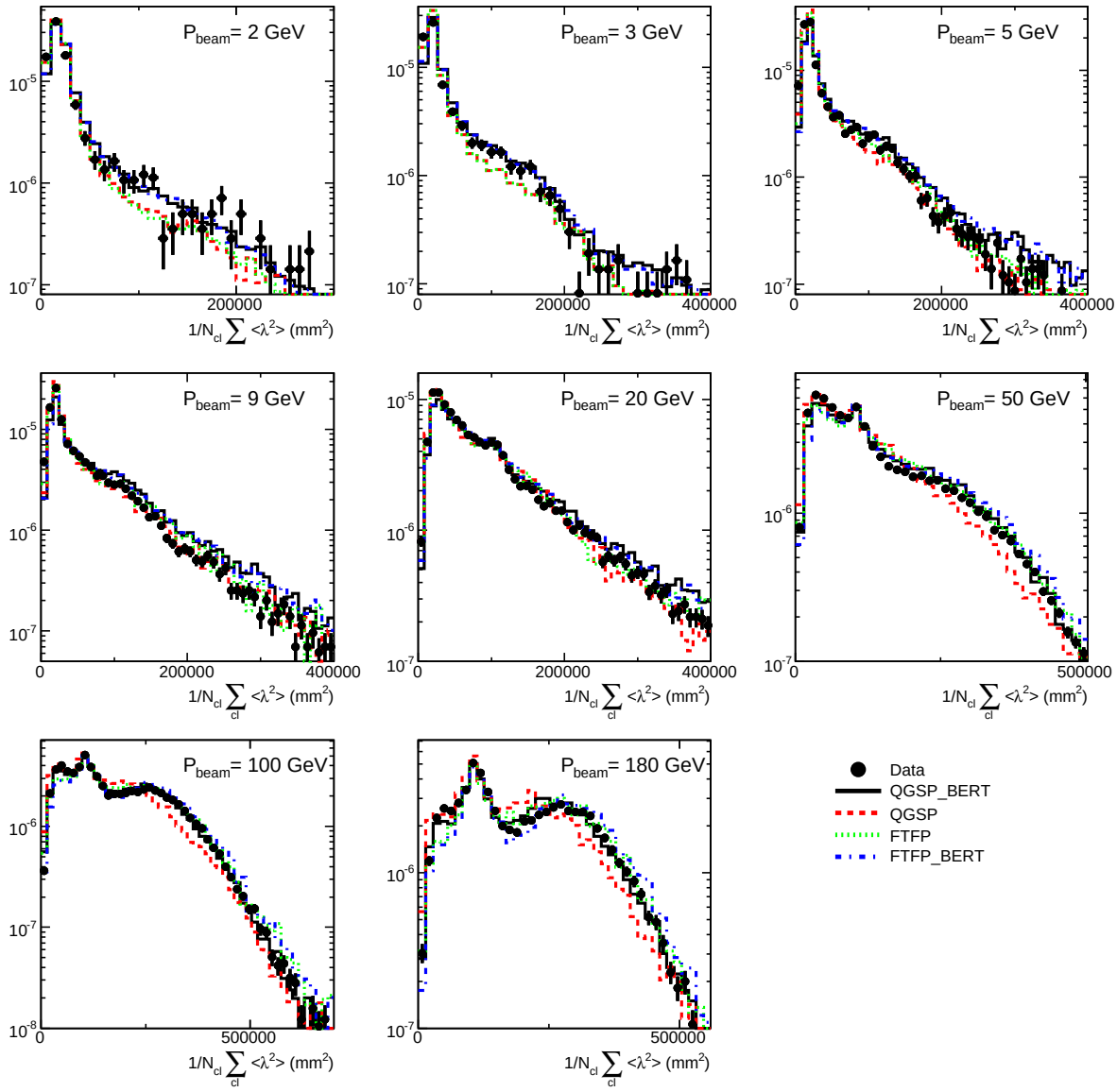

Figure 44: Distribution of the second longitudinal shower moment $\langle\lambda^2\rangle$ (shower length) for pions with beam momenta from 2 to 180 GeV. Shown are data as closed points and Monte Carlo simulations as lines. Only statistical uncertainties are shown.

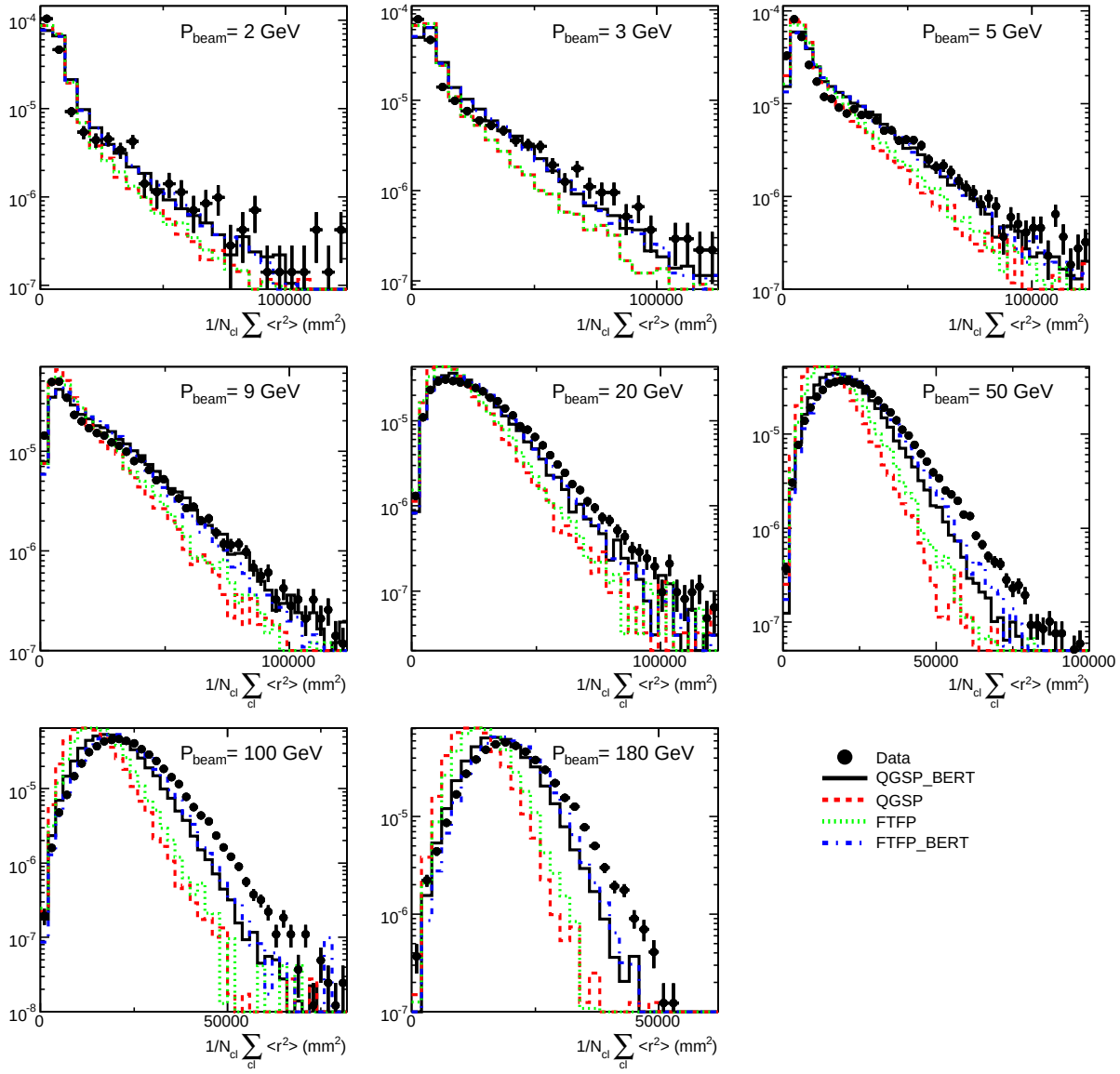

Figure 45: Distribution of the second radial moment $\langle r^2 \rangle$ (shower width) for pions with beam momenta from 2 to 180 GeV. Shown are data as closed points and Monte Carlo simulations as lines. Only statistical uncertainties are shown.

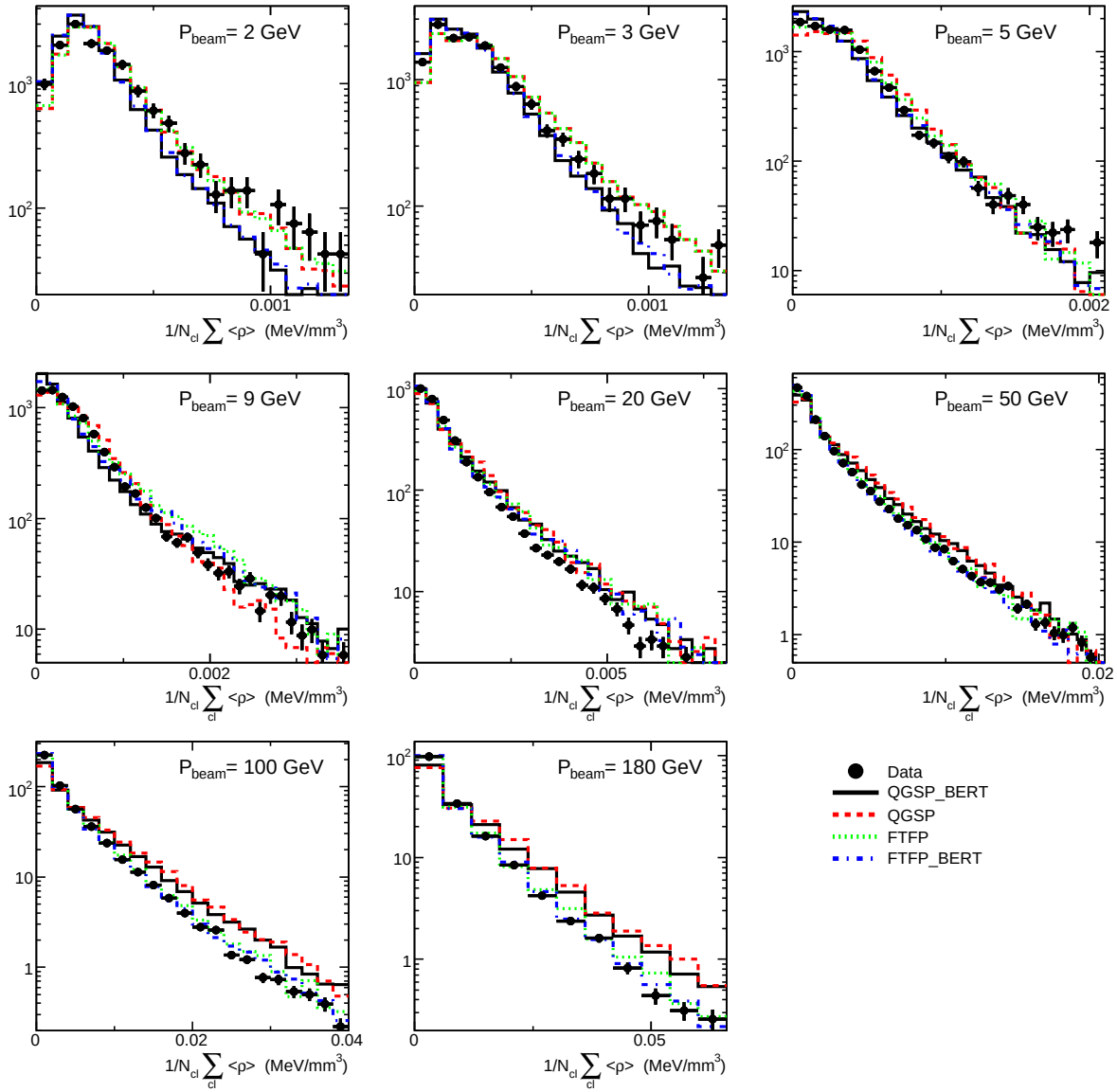

Figure 46: Distribution of the first $\langle\rho\rangle$ energy density moment for pions with beam momenta from 2 to 180 GeV. Shown are data as closed points and Monte Carlo simulations as lines. Only statistical uncertainties are shown.

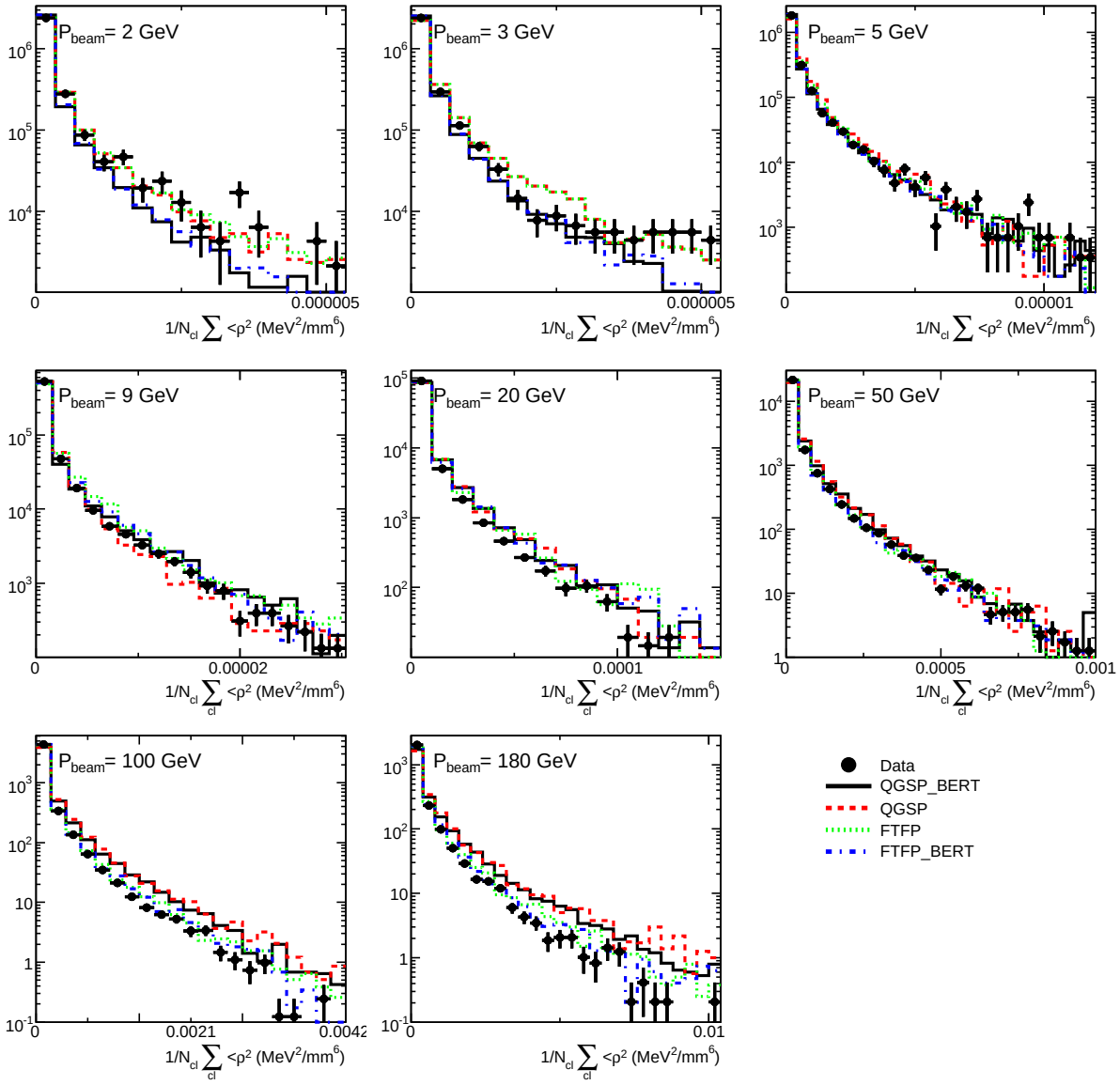

Figure 47: Distribution of the second $\langle \rho^2 \rangle$ energy density moment for pions with beam momenta from 2 to 180 GeV. Shown are data as closed points and Monte Carlo simulations as lines. Only statistical uncertainties are shown.

Appendix C: Energy Distributions in Calorimeter Compartments

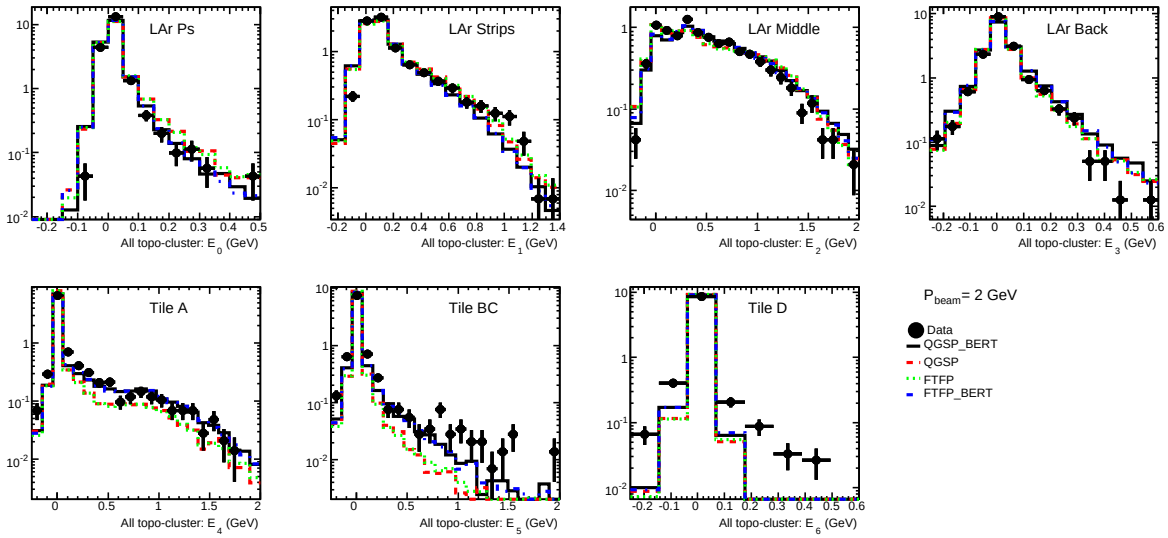

Figure 48: Energy distribution in the calorimeter compartments for pions with a momentum of 2 GeV. Only statistical uncertainties are shown.

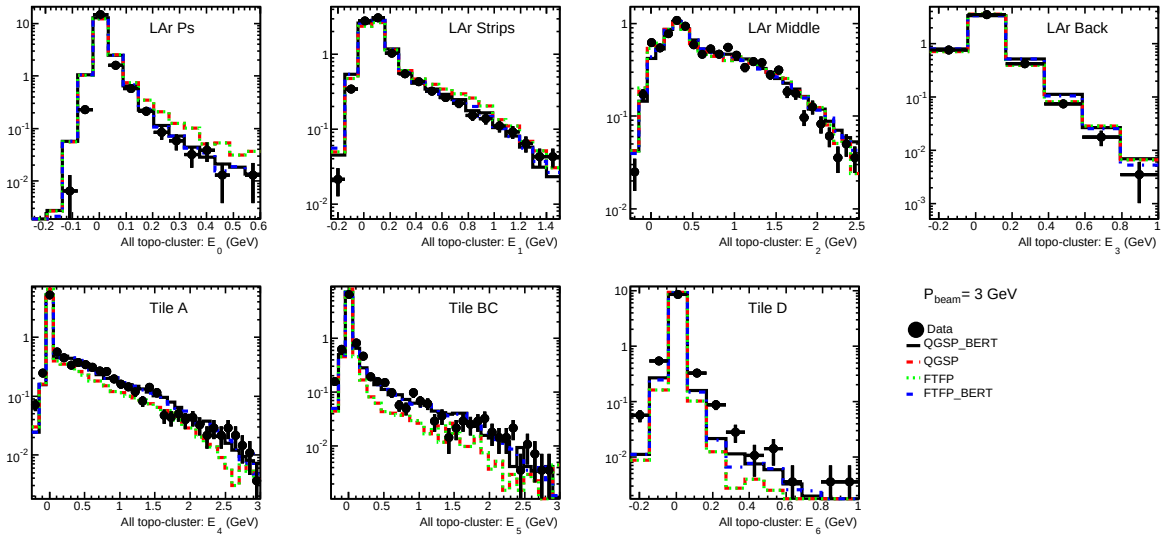

Figure 49: Energy distribution in the calorimeter compartments for pions with a momentum of 3 GeV. Only statistical uncertainties are shown.

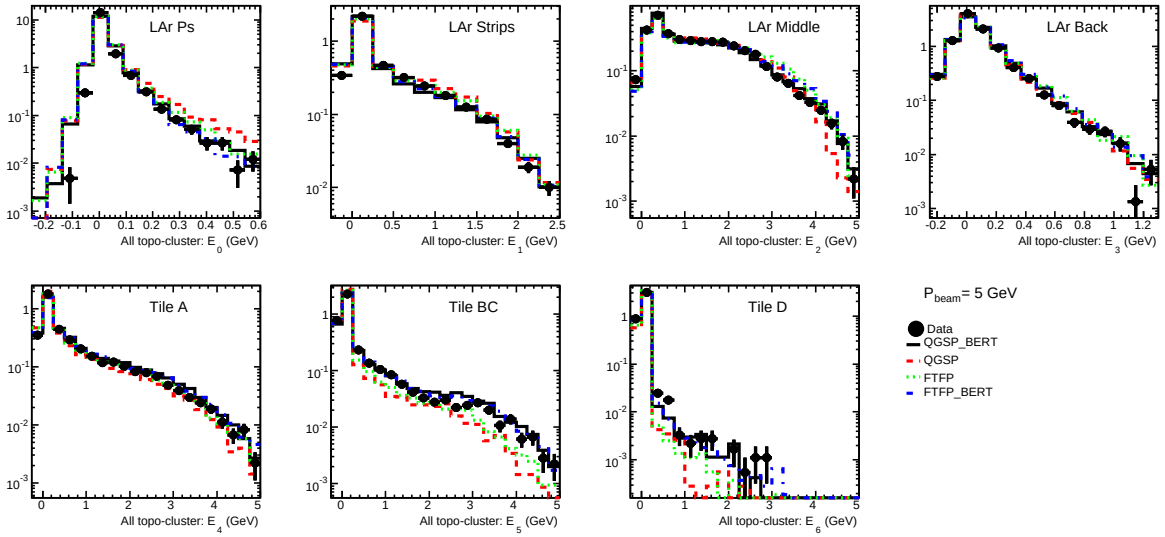

Figure 50: Energy distribution in the calorimeter compartments for pions with a momentum of 5 GeV. Only statistical uncertainties are shown.

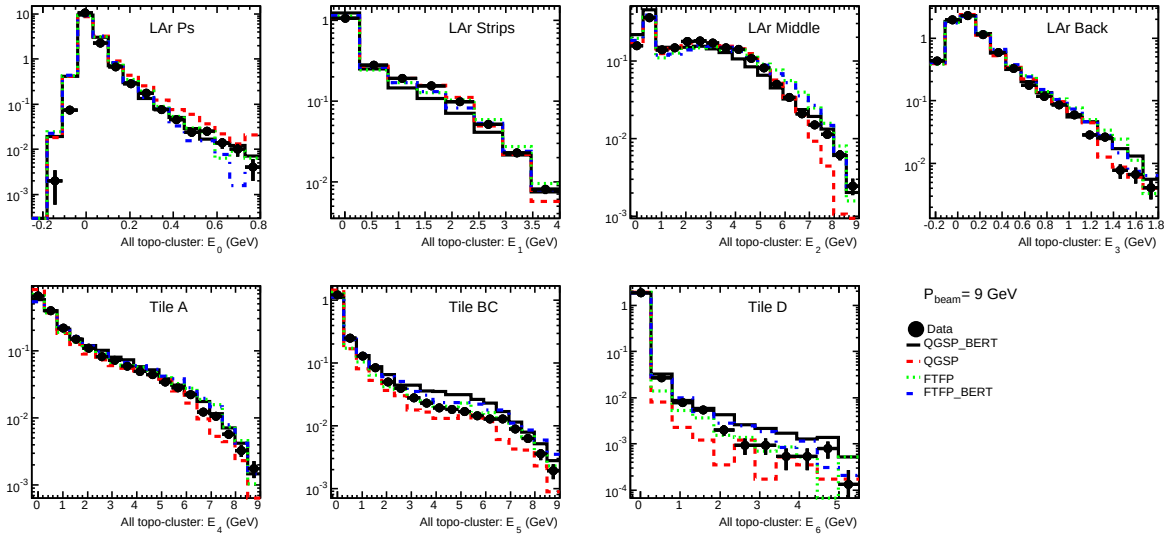

Figure 51: Energy distribution in the calorimeter compartments for pions with a momentum of 9 GeV. Only statistical uncertainties are shown.

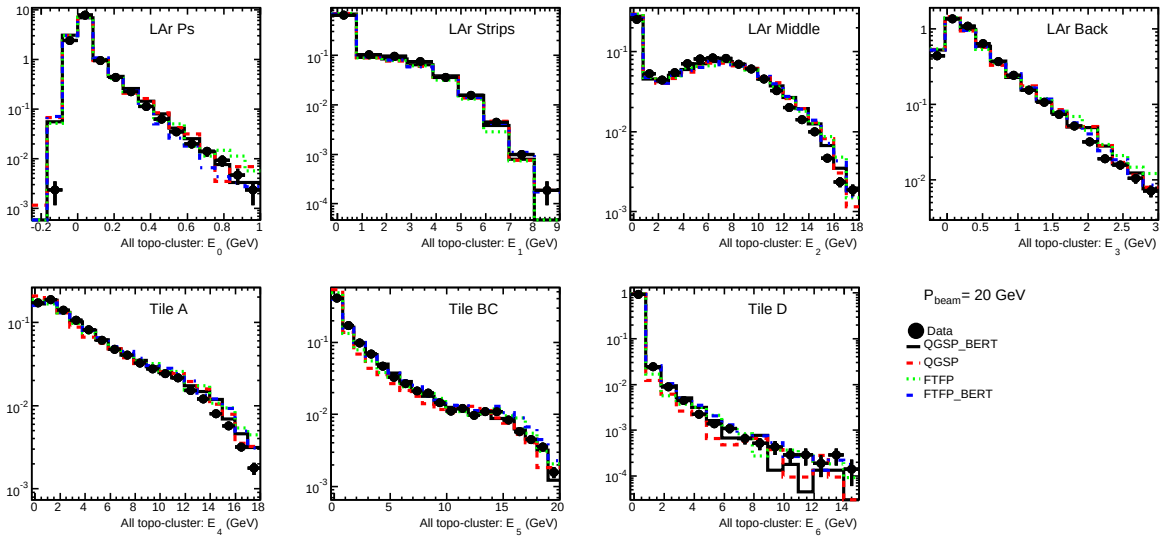

Figure 52: Energy distribution in the calorimeter compartments for pions with a momentum of 20 GeV. Only statistical uncertainties are shown.

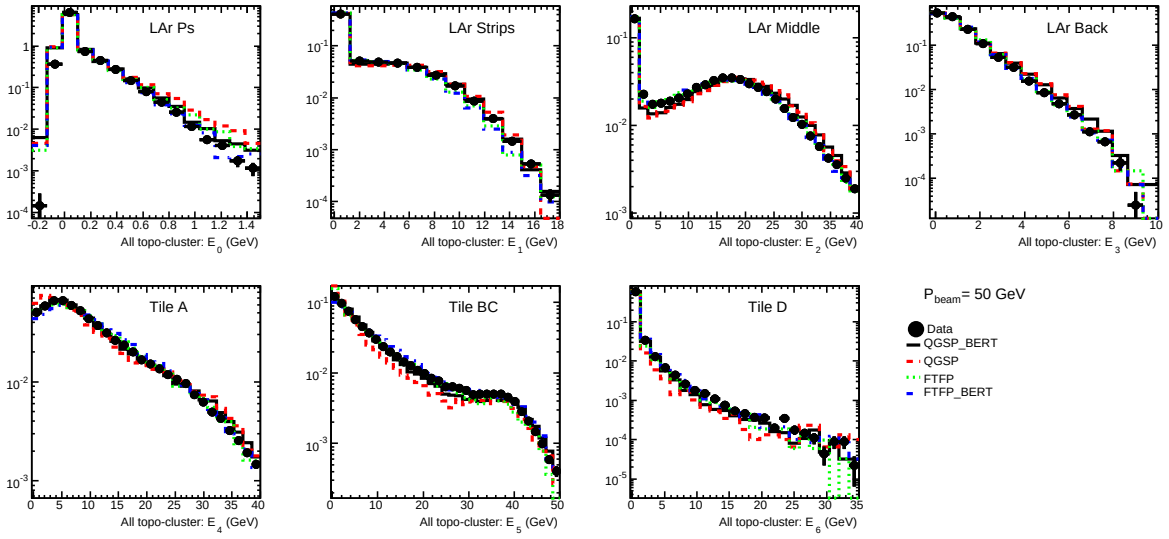

Figure 53: Energy distribution in the calorimeter compartments for pions with a momentum of 50 GeV. Only statistical uncertainties are shown.

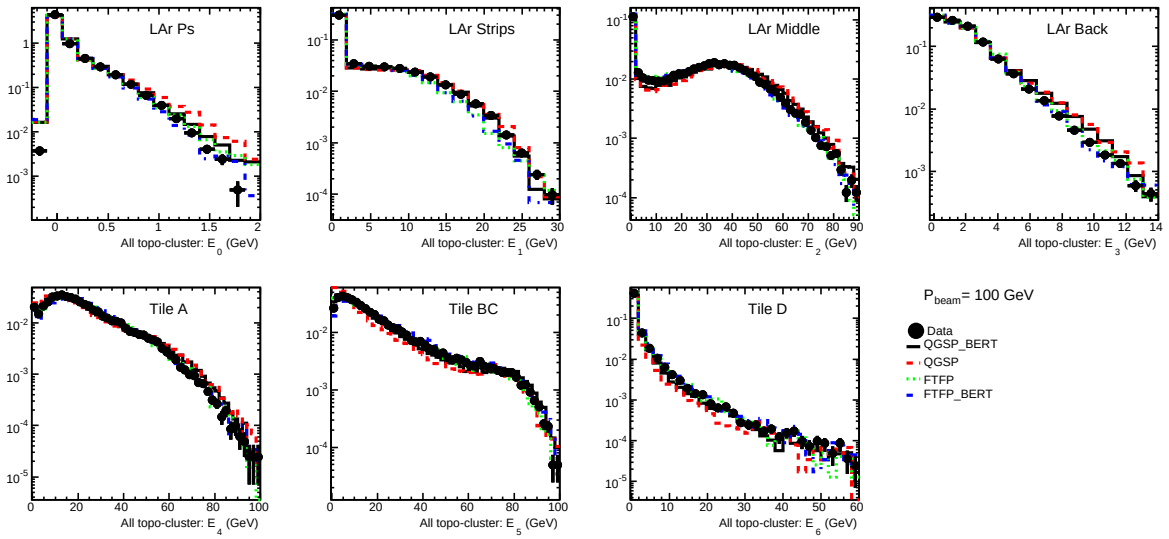

Figure 54: Energy distribution in the calorimeter compartments for pions with a momentum of 100 GeV. Only statistical uncertainties are shown.

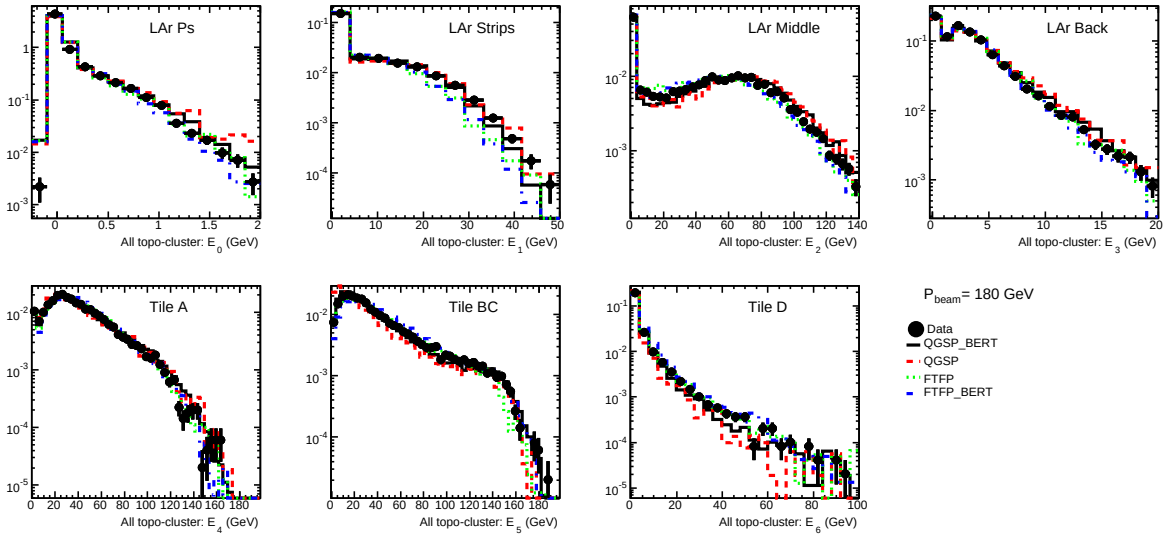

Figure 55: Energy distribution in the calorimeter compartments for pions with a momentum of 180 GeV. Only statistical uncertainties are shown.